High-Resolution Numerical Thermal Modeling of Timescales and Mechanisms of Rhyolite Genesis and Transport as a Consequence of Basalt Influx: Applications to the Long Valley Volcanic Field, CA

by

Meredith Adelle Calogero

A dissertation submitted in partial fulfillment
of the requirements for the degree of
Doctor of Philosophy
(Earth and Environmental Sciences)
in the University of Michigan
2021

Doctoral Committee:

Associate Professor Eric A. Hetland, Co-Chair
Professor Rebecca A. Lange, Co-Chair
Associate Professor Jeremy N. Bassis
Dr. Aaron Wolf
Professor Youxue Zhang

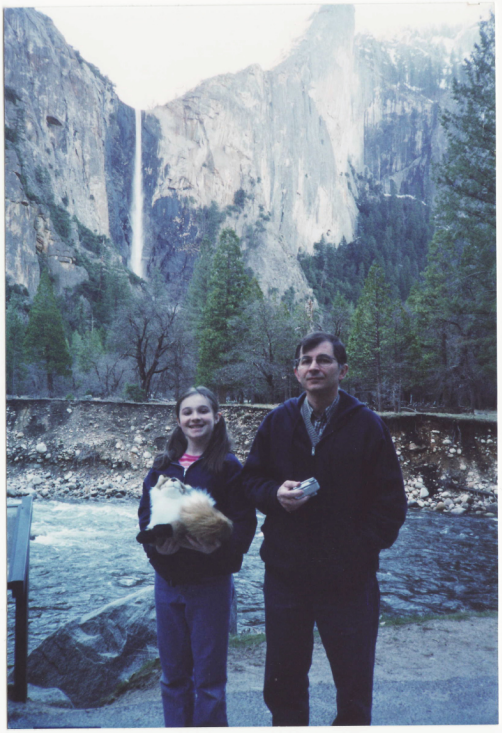

Meredith Adelle Calogero

calogero@umich.edu

ORCID iD: 0000-0002-4951-1755

Dedication

This dissertation is dedicated to my parents and grandmother, and every teacher, mentor, and friend along the way who provided me with the tools and encouragement to prime my own crust, one sill at a time. No matter how transient each moment may be, together there's enough impact to spark a supervolcano into action.

Acknowledgements

Many individuals played a role in the completion of this dissertation, whom I would like to recognize.

Firstly, thank you to my advisors, Eric Hetland and Becky Lange for all of your guidance, support, and reassurances throughout the years.

Eric, thank you for your patience and reliability as I navigated a research topic apart from your usual work. Thank you for humoring my interests, both personal and professional, in helping me feel at home here in Michigan. Thank you for welcoming me into your home and amongst your family. I appreciate everything you've done to take care me, especially during this past year full of stress and uncertainty. I'm thankful for what opportunities you've provided for me through teaching, travel to conferences and workshops, and every talk we've had about what my career path can look like. I am enthusiastic about continuing working together in the year ahead in my first post-doctoral role, and I am humbled by the chance to do so.

Becky, thank you for every long meeting, every phone call at odd hours; thank you for supporting my naturally odd circadian state of being to begin with. It has been so exciting to put vision into practice in developing this model, and I look forward to a long continued working relationship. I greatly appreciate your support and care, both in ensuring that my understanding of the real rock record is top notch, supplemented through our trips to Long Valley and Yosemite, and in ensuring I had opportunities to expand my horizons and network as far afield as Italy and Chile.

My gratitude to both of you for allowing me to take the helm of this project is boundless. Your support through my struggles adjusting to graduate school, the initial slow pace of developing this study, and the need for a second try sometimes to really tackle problems confidently have all helped shape the beginnings of my career. I never expected to be in Michigan of all places, but the opportunity to be here, at the crossroads of geophysics and petrology, is a blessing I am so happy for.

Thank you to my committee members – Youxue Zhang, Aaron Wolf, and Jeremy Bassis. Thank you for the trust and curiosity as I've presented my work and the oftentimes slow process of model development throughout the years. Jeremy, our interactions have always been very clear and productive, and I greatly appreciate your input on my code development and throughout the years. Aaron, from even my first week in the department, your scientific curiosity has been an inspiration to me. I am always impressed with your insights and inquiries in seminars and department lectures, and with your strong blend of physics and geochemistry knowledge. Furthermore, the MRM seminars you led were key in helping me break out of my shell in my early years here. All of our interactions have been invaluable to me and I am exceedingly grateful to you. Youxue, first of all, thank you for re-directing my Michigan application to Eric and Becky in the first place, as that action made this all possible. Your input in our committee meetings and subsequent lively discussions have greatly helped my progress through this study, and broadened my understanding of geochemical processes.

Many other individuals in the Earth Department have played key roles in supporting me through this thesis and I am beyond thankful. I want to draw special attention to a few individuals. James Jolles, Sarah Brehm, and Juliana Mesa from Becky's lab, and Olivia Helprin and Eric Szymanski from Eric's lab have acted in many roles for me as both scientific support,

and friendly ears, and I could not have completed this dissertation without you. An extra shout out is noteworthy for Juliana and Olivia who have kindly kept track of my sanity during this stressful year. You are my friends for life.

My cohort – especially Meg Veitch, Tristan Childress, Youngjae Kim, Katy Rico, Brian Konecke, Arianna Trusiak, Alex Tye, and Hong "Dora" Shen: thank you for being friends and supporters for me as we all navigated this new experience and life in Ann Arbor, Michigan, together. I am excited to see where each of your own careers take you!

Others in the department who I spent significant time with, through the Geophysics lab, teaching, or otherwise – Marlon Ramos, Prithvi Thakur, Jing Ci Neo, Kierstin Rosenbach, Ethan Shirley, Maria Rodriguez Mustafa, Meichen Liu, Peng Ni, Chenghuan Guo, Ross Maguire, Sha Chen, Nikolas Midttun, Trevor Hines, Sean Hurt, and Xiaofei Pu: you all inspire me, personally and academically, and I am very thankful to know you all.

Additionally, thank you to Anne Hudon, Craig Delap, Nancy Kingsbury, and everyone working in the office who have supported me throughout these years. Thank you to Jeroen Ritsema, Kacey Lohmann, and Ben van der Pluijm for the opportunity to teach with you. Engaging with students at an introductory level is a passion of mine and I greatly enjoyed working with you each over those five semesters.

Outside of our department, I must express my utmost thanks to David Sparks at Texas A&M University, who opened the door for me to numerical modeling research in general, when I was a stressed out undergraduate in introductory Geophysics, trying to solve my homework on a Friday afternoon. Your support for my career and encouragement from that day are precious to me, and your dedication to teaching and strengthening the educational opportunities back at TAMU are things I aim to take forward in my own career.

I want to thank my family. Between trips to National Parks at a young age, especially the visits to Yosemite and one life changing visit to Mt. St. Helens which set volcanoes on my heart, and your support as I eagerly chased this career in academia – I'm grateful that I've been allowed to pursue my dreams this way. Your love and support, your insights and encouragement, all of it means the world to me. I also want to thank my best friends, Angelica Reynoso and Kristen Mallett, née Kiser, for loving and cheering me on all these years. To the Reynoso and Kiser families as well, I'm so grateful to you all for the friendship, support and kindness you have shown me.

Lastly, thank you to Gabbro, my cat, for your warmth and unconditional love. This year you have taken to sleeping beside my head every night, and instantly make every problem feel smaller.

Thank you to everyone, I cannot express it strongly enough.

Table of Contents

List of Tables

List of Figures

List of Appendices

Abstract

High-silica rhyolites (>75 wt% SiO_2) are the most differentiated magmas on Earth. Though rare in subduction volcanism, they erupt in large volumes (100–1000s km^3) in extensional settings. Understanding their generation is crucial as rhyolite formation substantially alters the continental crust, and such voluminous eruptions have global implications. Two supervolcano eruptions of high-silica rhyolite have occurred in the Western U.S. within 1 Myr, Long Valley, California, and Yellowstone, Wyoming. This thesis focuses on Long Valley caldera, where 800 km^3 rhyolite erupted over the last 2.2 Myr, including the catastrophic caldera-forming Bishop Tuff eruption resulting in ≥600 km^3 of zoned rhyolite in under a week. The second-most eruptive magma type in Long Valley is basalt. The formation of silicic magmas in response to basalt influx has been addressed by numerous numerical models in the literature. This study differs in that I present a novel numerical model with high spatial (~1 m) and temporal (<day) resolution, tracking both kilometer- and meter-scale thermal and compositional evolution as consequences of basaltic sill emplacements and secondary rhyolitic melt segregation and transport.

In Chapter 2, I investigate the crustal-scale response of basaltic sill emplacements into thick (32 km) granitoid crust, and quantify the importance of emplacement rate, depth range, and ambient temperature for causing substantial localized heating. I constrain the timescales for volatile release from a basaltic sill with finite H_2O during crystallization and for the formation of transient wall-rock partial melts on the order of sill thickness. These timescales are both dependent on local ambient temperature and overlap within 10–100s of years after sill

emplacement. Based on the results presented in Chapter 2, I hypothesize a mechanism for secondary melt migration, wherein melting of pre-existing aplite dikes enables transport of rhyolite melt.

To address the consequences of secondary rhyolitic melt transport, I developed a new numerical model in Chapter 3, which I have named TIRAMISU (Transient hIgh-Resolution pArtial MeltIng Simulation of the crUst). The core of TIRAMISU is similar to that presented in Chapter 2, but in TIRAMISU melts may ascend if the sill center attains 80% crystallization and there is enough cumulative partial melt within the wall rock adjacent to the sill to be captured by model resolution. Secondary transport driven by a 50-m thick basalt sill invading the deep crust every 5 kyr results in about 60ºC cooling of the lower crust, and <60ºC warming of the crust around the shallower rhyolite sills. For 3 km of basalt emplaced, about 1.7 km of rhyolite was generated, with about 30% of rhyolite from basalt and 70% from the granitoid crust.

TIRAMISU tracks the evolving composition of the crust, including the partitioning of Sr. The Sr signature of the volcanic products in Long Valley is somewhat paradoxical. In these simulations, I find average Sr concentrations in the first-generation rhyolites of 380 ppm, with about 60% of the cumulative Sr from basaltic sources. Using melt contribution and Sr contribution percentages, I can estimate further drops in Sr concentration in second- and third-generation rhyolites, which would form through subsequent stages of melt transport. I intend further expansion of TIRAMISU to further investigate Long Valley, estimating the range of basalt influx histories needed to generate the observed volcanic products, as well as for exploring additional volcanic plumbing systems.

CHAPTER 1
Introduction

High-silica rhyolite (≥75 wt% SiO_2) is the most evolved eruptive magma type on Earth. While rare in subduction zone volcanism, high-SiO_2 magmas sometimes erupt voluminously (>500 km^3) as supervolcano eruptions in regions dominated by extensional tectonics. There have been two such eruptions in North America in the last 1 Myr (Figure 1-1), both within extensional tectonic settings and both accompanied by abundant mantle-derived basalt; the Lava Creek tuff out of Yellowstone caldera, Wyoming, (~1 Ma; e.g., Christansen, 2001), and the Bishop tuff eruption out of Long Valley caldera, California, (~765 ka; Andersen et al., 2017). The mechanisms and timescales surrounding the origin of these highly explosive, massive volumes of evolved magma is a key question in volcanology today, as such eruptions have catastrophic implications for global climate and are a major hazard within the western US.

In this study, I seek to understand the origin of rhyolites, focusing on the high-SiO_2 rhyolites of the Long Valley (LV) volcanic field. Geochemical evidence demands that there are contributions from both mantle-derived basalts and crustal rocks to form these high-SiO_2 rhyolites. One such piece of evidence is that the LV high-SiO_2 rhyolites have a high H_2O content (>6.5 wt% H_2O; Wallace et al., 1999). The underlying Mesozoic granitoid which makes up the Sierra Nevada batholith cannot carry more than 0.6 wt% H_2O within biotite and amphibole phases (Bateman, 1992), and thus cannot be the provider of H_2O to the high-SiO_2 rhyolites. In

contrast, coeval eruptive LV basalts are rich in H_2O, containing 3–6 wt% H_2O (Jolles, 2020). Additionally, the high-SiO_2 LV rhyolites have high-Nd and low-Sr isotopic ratios which are indicative of the influence of mantle-derived basalt (Figure 1-2). I point out two LV basalt populations, separated by time, which are similar in isotopic Sr, but strongly dissimilar in Nd isotopic values. The isotopic compositions of these basalt populations are distinct from the swath of Mesozoic granitoids of the Sierra Nevada, including the populations in nearest proximity to Long Valley caldera (Barth et al., 2011).

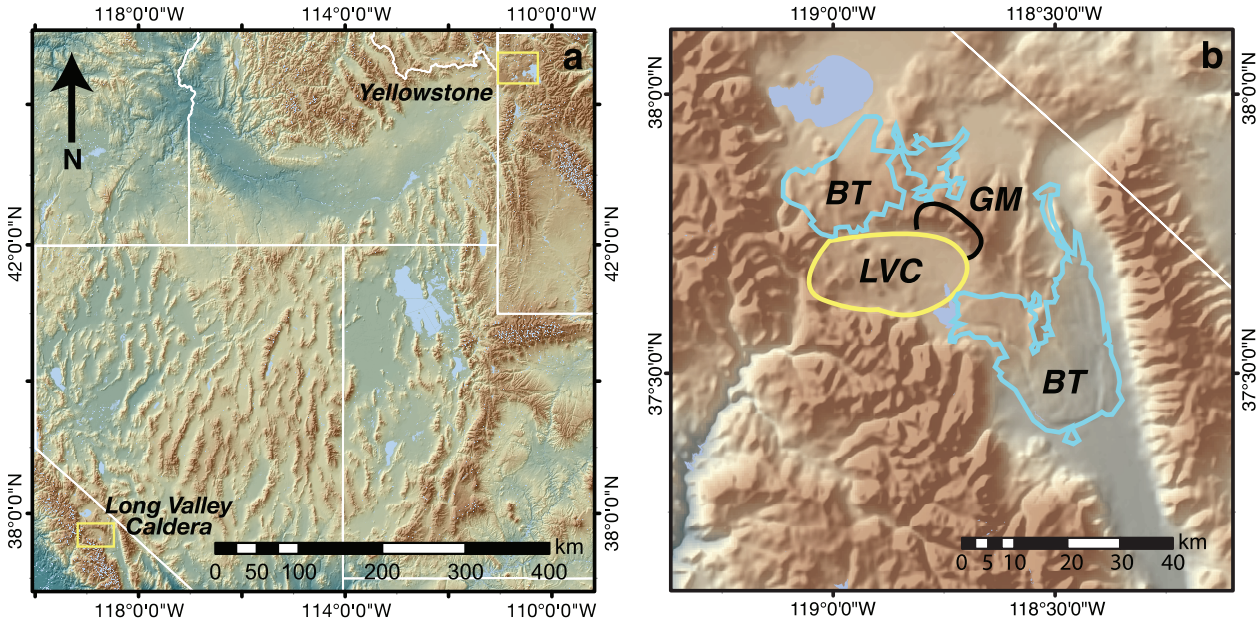

Figure 1-1. (a) Map of Basin and Range province in western U.S.; Yellowstone, WY, and Long Valley, CA, are sites of super-volcano eruptions of high-SiO2 rhyolite <1 Ma. (b) Blow-up of Long Valley caldera, California; modified from Hildreth & Wilson (2007). BT is Bishop Tuff, LVC is Long Valley caldera, and GM is Glass Mountain.

Variability in major and trace element concentrations highlight the inability of mantle-derived basalt to be the sole parent to the LV rhyolites. Another such discrepancy is the presence of quartz, sanidine, and sodic-plagioclase ($\leq An_{25}$) in high-SiO_2 rhyolites (e.g., Metz & Mahood, 1991). This mineralogical composition cannot be derived in one stage of melting from a basaltic parent, even as a low-degree partial melt. The LV basalts are also enriched in MgO, yet there is <0.1 wt% MgO measured in LV rhyolites (Hildreth & Wilson, 2007; Metz & Mahood, 1991).

Additionally, the early and late populations of LV basalts are rich in Sr, containing 1000-2000 ppm and ~550 ppm respectively (Cousens, 1996). In contrast, the eruptive high-SiO_2 rhyolites contain <25 ppm Sr (e.g., Hildreth, 1979; Metz & Mahood, 1991). All of these differences between the erupted basalts and rhyolites, taken together, motivate the question: How can the isotopic concentrations and the H_2O content found in the eruptive rhyolites be derived from local basaltic magmas, yet these same rhyolites, some voluminous, are extremely differentiated and remain uncontaminated by major (e.g., MgO) and trace elements (e.g., Sr) found enriched in the basalt?

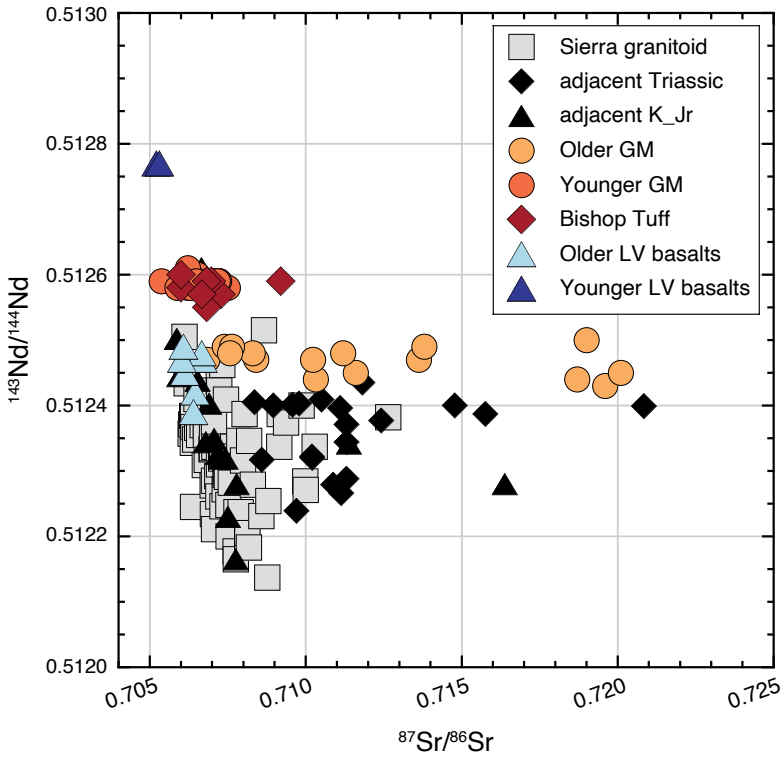

Figure 1-2. Plot of $^{143}Nd/^{144}Nd$ vs. $^{87}Sr/^{86}Sr$ isotopic compositions for plutonic and volcanic rock units relevant to the Long Valley magmatic system. Literature sources for these data are listed in Table 3-1. Triassic and Cretaceous-Jurassic granitoid units, which outcrop adjacent to the Long Valley caldera region, are shown by black diamond and black triangles; all other Sierra granitoid units (with $^{87}Sr/^{86}Sr$ values ≥0.706) are shown with gray boxes. Older and Younger GM refer to Glass Mountain rhyolites erupted along the northern margin of Long Valley caldera pre- and post 1.2 Ma, respectively. The Bishop Tuff rhyolite (>600 km^3 erupted at ~765 ka to form the Long Valley caldera; Andersen et al., 2017) is shown by dark red diamond. The Older and Younger LV basalts refer to all high-MgO (>7 wt%) basalts that erupted pre- and post-caldera, respectively. All Sierra Nevada granitoid isotopic data are those measured (i.e., not age-corrected to initial values) since these are the relevant values for partial melting events in the Plio-Quaternary. Conversely, all the Long Valley rhyolite (i.e., GM and Bishop Tuff) isotopic data are corrected to

values at the time of their eruption, since these are the relevant values when tracking the isotopic signature of their source rocks. Note that the Long Valley rhyolites all have Nd isotopic compositions that are shifted to higher values than those for granitoid in the crustal column, consistent with a strong influence from Long Valley basalts. Note also that the younger GM and Bishop Tuff rhyolites have an average Nd isotopic signature that is intermediate between the older and younger LV basalts, which points to both suites of basalts playing a role in their origin.

The necessity of mantle-derived basalt influx as a source of heat, volatiles, and potential physical contribution in conjunction with partial melting of the nearby crustal column as the mechanism for generating silicic magmas has been extensively explored in the literature (e.g., Huppert & Sparks, 1988; Petford & Gallagher, 2001; Jackson et al., 2003; Dufek & Bergantz, 2005; Annen et al., 2006; Leeman et al., 2008; Karakas & Dufek, 2015; Colón et al., 2018). Here, I present a brief review of the questions posed through such prior efforts. Several early models explored a whole crustal-scale response to basalt influx (as sills and/or dikes; e.g., Dufek & Bergantz, 2005; Annen et al., 2006; Leeman et al., 2008; Karakas & Dufek, 2015; Colon et al., 2018). In these cases, the efficiency of different basalt emplacement geometries has been explored, with horizontal sills emplaced randomly at depth identified as the most efficient way to broadly heat the crust quickly. Sills are considered the more efficient geometry for heat transfer (Huppert & Sparks, 1988), and the random emplacement of such sills (e.g., Dufek & Bergantz, 2005; Annen et al., 2006; Karakas & Dufek, 2015; Colon et al., 2018) has been shown to be more effective at crustal heating than a fixed or underplating scheme (e.g., Huppert & Sparks, 1988; Petford & Gallagher, 2001; Jackson et al., 2003; Annen et al., 2006; Leeman et al., 2008).

Transient partial melts adjacent to basaltic sills after emplacement were identified by Huppert & Sparks, (1988) but the potential for segregation of these melts has been largely ignored, and instead previous models consistently aim to elevate a broad portion of the crust to super-solidus conditions, thereby generating a km-scale body of silicic melt. All the aforementioned models treat partial melt of crustal wall rock and residual melt within their basaltic mass separately. With fixed basalt emplacement in the middle crust at 10 km, Leeman et

al., (2008), found they required 16 km of basalt to generate enough rhyolite between the two reservoirs in order to match the eruptive volume from one magma field of the Snake River Plain (SRP) hotspot track. While seismic evidence reveals a mid-crustal low velocity zone under the SRP (Yuan et al., 2010), it is not extensive enough to match the modeled basalt thickness. Seismic studies similarly indicate a mid-crustal low velocity zone underneath Long Valley (e.g., Thurber et al., 2009; Frassetto et al., 2011; Flinders et al., 2018) Further work on understanding the interplay between extensional tectonics and magma evolution point to intermediate–high extension rates (>0.005 m/yr; Karakas & Dufek, 2015) in order to accommodate for a basalt emplacement rate high enough to maintain both melt reservoirs super-solidus.

In this thesis, I present an alternative method to accumulate a sub-solidus, fertile, leucogranite parent for the Long Valley rhyolites. Specifically, I consider the interaction of transient wall-rock partial melts and the interstitial melts from crystallizing sills in addressing paradoxical contributions of H_2O and Sr isotopic signature of mantle-derived basaltic origin and the extreme Sr depletion found in the LV rhyolites. To investigate such, in this dissertation research I developed a numerical simulation capable of resolving transient partial melting of the crust within the first 10–100s of years after basaltic sill emplacement. Prior to this dissertation research, all numerical simulations ignored this transient melting, which was considered insignificant because there would not be time for the melt to ascend far through flow along grain boundaries before re-crystallization (e.g., Jackson et al., 2003). However, if these crustal partial melts interact with local residual melts from the basalts on similar time scales, they may reasonably ascend together some distance, before freezing again as secondary melt emplacements. The simulations in this dissertation are motivated by the LV system, and a brief overview of the geologic history of Long Valley is provided in Chapter 2.

In Chapter 2 (published in *Journal of Geophysical Research: Solid Earth*), I presented a novel, high-resolution numerical thermal model, developed in Matlab, to evaluate key processes regarding the development of transient localized partial melts as a consequence of basalt influx into granitoid. The model solves thermal diffusion on a finite difference moving mesh in 1-D with Runge-Kutta time stepping (e.g., Dormand, 1996) between instantaneous emplacements of basalt. A high-resolution of 1 meter was used within the basaltic sills, as well as extending one sill thickness (50 m) above and below each basaltic sill, which is assumed infinite in lateral dimensions. The meter-level resolution of these simulations is a more than three orders of magnitude increase in the resolution in previously published numerical simulations (e.g., Dufek & Bergantz, 2005; Annen et al., 2006; Leeman et al., 2008). To maintain computational tractability, minimizing the total number of finite-difference nodes used, I allow for lower resolution far away from the sill, where there are no abrupt thermal or material phase changes. By keeping the number of nodes used in each simulation relatively low, I am able to compute crustal-scale thermal evolution over millions of years, at the same time as I can capture the localized response in and around the basaltic sill following its emplacement and subsequent solidification. At the crustal scale I tested several factors to identify the strongest controls on thermal evolution, and our results are broadly consistent with other numerical thermal models (e.g., Dufek & Bergantz, 2005; Annen et al., 2006; Leeman et al., 2008; Karakas & Dufek, 2015; Colon et al., 2018). I find that partial melting is maximized with random sill emplacement rather than a fixed underplating, high emplacement rates, which limit cooling between events, and the availability of H_2O in the basalt. This third control is the most striking, as I compare the significant partial melt fraction development in the wall rock under finite fluid-present conditions compared to fluid-absent conditions.

At the sill-scale, I identify the duration after sill emplacement for transient partial melt formation at various depths in the wall rock above the sill, for various initial basaltic sill thicknesses. For a given thickness, the degree of melting is strongly controlled by the ambient temperature. For example, for basalts emplaced at 50 m per 10 kyr into a 650ºC ambient temperature, 20 and 5% partial melts develop from granitoid and previously solidified mafic sills respectively, 50 m above the newest sill's top surface. This difference in degrees of melting has geochemical implications, which I explore further in Chapter 3. Here, I also identify the timescales for H_2O exsolution from a crystallizing basaltic sill of varying thicknesses with initial 3 wt% H_2O. The strongest control on this process is also ambient temperature. Because H_2O provided from the sill is limited, high-degree partial melts are expected to be fluid-undersaturated, and thereby have a large increase in volume (>10%; Lange, 1997; Ochs & Lange, 1999). This scenario promotes the growth of microcracks and development of melt-filled fractures in the wall rock (e.g., Connolly et al., 1997; Rushmer, 2011). Additionally, near-eutectic bulk composition aplite dikes (e.g., Sleep, 1988) are a ubiquitous, pre-existing, scattered feature in granitoid (e.g., Lange, 2019). When the surrounding granitoid partially melts, aplite dikes will melt entirely. Should these melts begin ascent, a pressure gradient is expected to form, driving local partial melts and interstitial melts from the crystallizing sill into the available fracture channel. The aplite dikes therefore offer a viable hypothesis for secondary melt transport, and I consider the thermal and compositional consequences of a secondary melt transport process in Chapter 3.

The model presented in Chapter 2 was insufficient for addressing questions related to the segregation and ascent of melts, and for tracking melt composition. The main impediment to capturing these phenomena was that the Matlab code I initially developed faced memory

bottlenecks and was inefficient. As such, it was imperative to develop a new numerical model within a more robust computational framework (Figure 1-3). The new model, which I've named TIRAMISU (Transient hIgh-Resolution pArtial MeltIng Simulation of the crUst), is written in the Julia programming language (Bezanson et al., 2017). Julia is fast, with benchmark speeds approaching C programs (julialang.org/benchmarks/), while Julia has a Matlab-like syntax. Moreover, Julia is non-commercial, with interpreters available for the three major operating systems, ensuring the maximum portability of TIRAMISU. The core of the numerical simulation in TIRAMISU remains the same as the initial version; I use a finite difference approach to solve for the evolution of temperatures and transient melting/solidification at a crustal-scale (i.e., over tens of kilometers) in response to the injection of thin basaltic sills in 1-D space (i.e., over tens of meters), while enforcing high-resolution in and around each sill as it cools. Four crucial additions were made in the development of TIRAMISU to provide additional utility: 1) All physical parameters are generalized for each basaltic sill, such as emplacement depth and time, thickness, and temperature. 2) I implement temporal and spatial criteria to trigger instantaneous secondary melt transport. The temporal criterion is based upon the timing of H_2O exsolution from the crystallizing sill which I identified in Chapter 2, and the spatial criterion is associated with the minimum spatial resolution. 3) Fundamentally, secondary melts (partial or residual, depending on the direction of temperature evolution) are more geochemically evolved than their source rocks, and the rock left behind is more refractory. These geochemical changes additionally affect their material properties. I calculate adjustments to ensure such material property changes occur with every transport event, and this results in a broadly diverse crustal column. 4) I track physical contributions to the secondary melt from different source types (e.g., basaltic and granitoid wall rock) separately, and through this I incorporate tracking of element partitioning

(e.g., Sr) between parental sources and the next generation of melts. The development of TIRAMISU has been a long-term project, born in mid-2018, and further expansions will continue after the conclusion of this thesis.

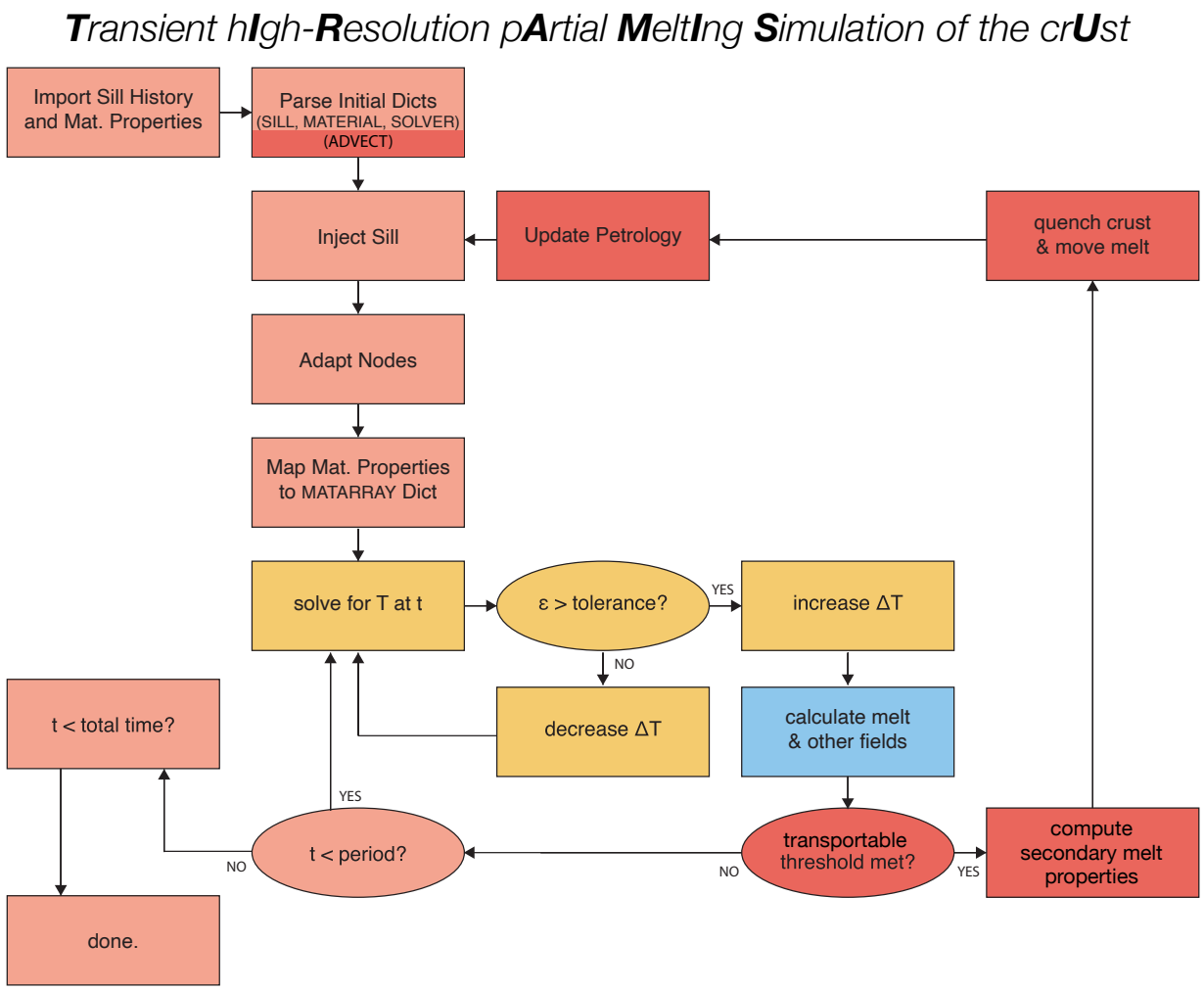

Figure 1-3 Flowchart of TIRAMISU. Orange represents simulation input, output, and the enveloping structure of the simulation. Yellow represents the Runge-Kutta time-stepping procedure. Blue represents the updating and storage of information for all physical and material fields. These portions existed in some form in the model presented in Chapter 2, however, have been revised, simplified, and generalized in TIRAMISU. All red portions are new to TIRAMISU and represent the secondary melt transport process which is discussed thoroughly in Chapter 3.

I present preliminary results of the thermal and compositional consequences of secondary melt transport in Chapter 3 (Chapter 3 will be prepared for publication). Affirming our expectations, the transport of secondary rhyolitic melts from depth to higher in the crustal column consequently warms the crust around the new emplacements and induces cooling of a

similar magnitude at depth. While this was expected, our work quantified the degree of heating/cooling due to the secondary melt movement. In our simulations, at a basalt emplacement rate of 50 m per 5 kyr, this resulted in a net 60ºC gain/loss of heat along the crustal column and further rates and emplacement geometries will be explored in our future studies. I was also able to quantify the thickness of rhyolite generated over time, relative to the original basalt influx. For 3 km of basalt emplaced, about 1.7 km of rhyolite formed and was transported to form secondary sills. Such extensive rhyolite production is reasonable for LV given the availability of subduction altered lithosphere as a source of hydrous basalts (~3-6 wt% H_2O; Jolles, 2020) coupled with the extremely thick upper crustal granitoid (~32 km; Fliedner et al., 2000) which by itself is low in H_2O (<0.6 wt% H_2O available in biotite and hornblende; Bateman, 1992). Natural interaction between both sources, due to H_2O exsolution, allows for more rhyolitic melt generation than would be possible under fluid absent conditions.

In Chapter 3, I finally demonstrate that there is a drop in Sr concentration in the rhyolite melts relative to either parental source, with isotopic signatures falling between those of either parent, 0.7068 $^{87}Sr/^{86}Sr$ on average. The secondary rhyolites achieve an average Sr concentration of 380 ppm. Multiple stages of crustal reworking, where basalt invades and partially melts the secondary rhyolites, producing a tertiary stage of even more evolved rhyolites, are necessary to achieve such low Sr concentrations as exhibited in the eruptive high-SiO_2 LV rhyolites. About 30% of the cumulative rhyolite had a basaltic source, however, the basaltic sources provided about 60% of the Sr. I use this information to inform simplified calculations for a second generation of partial melting, as well as to predict Nd concentration and isotopic evolution. The addition of Nd partitioning will add further constraints to our modeling efforts in the near future.

This dissertation research addressed specific questions pertaining to the development of the Long Valley volcanic system, that were only able to be addressed with the simulations developed. Nevertheless, not all of the questions have been answered. I continue to work towards developing a fuller model of the Long Valley system. While some issues can be investigated with the current version of TIRAMISU, further development of TIRAMISU is required to address a broader range of questions. In chapter 4, I discuss plans to incorporate a deterministic, buoyancy driven approach to secondary melt transport. Future studies include the evaluation of additional sill emplacement geometries, such as an ascending window for basalt emplacement, in order to address the multiple stages of crustal reworking necessary to develop the extremely low-Sr Long Valley rhyolites. I hope to use TIRAMISU as a launching point to explore volcanic plumbing systems underneath other large silicic systems, such as Yellowstone, and regions of subduction zone volcanism.

References

Andersen, N.L., Jicha, B.R., Singer, B.S., & Hildreth, W. (2017). Incremental heating of Bishop Tuff sanidine reveals preeruptive radiogenic Ar and rapid remobilization from cold storage. *Proceedings of the National Academy of Sciences of the United States of America*, 114(47), 12407-12412. https://doi.org/10.1073/pnas.1709581114

Annen, C., Blundy, J.D., & Sparks, R.S.J. (2006). The genesis of intermediate silicic magmas in deep crustal hot zones. *Journal of Petrology,* 47(3), 505-539. http://doi.org/10.1093/petrology/egi084

Barth, A.P., Walker, J.D., Wooden, J.L., Riggs, N.R. & Schweickert, R.A.. (2011). Birth of the Sierra Nevada magmatic arc: Early Mesozoic plutonism and volcanism in the east-central Sierra Nevada of California. *Geosphere,* 7, 877-897.

Bateman, P.C. (1992) Plutonism in the central part of the Sierra Nevada batholith, California. *U.S. Geological Survey Professional Paper,* 1483, 1-186.

Bezanson, J., Edelman, A., Karpinski, S., & Shah, V.B., (2017). Julia: A fresh approach to numerical computing. *SIAM Review*. 59:1, 65-98.

Calogero, M.A., Hetland, E.A., & Lange, R.A. (2020). High-resolution numerical model of heat and volatile transfer from basalt to wall rock: application to the crustal column beneath Long Valley caldera, CA. *Journal of Geophysical Research: Solid Earth*, 125, e2018JB016773. https://doi.org/10.1029/2018JB016773

Christiansen, R.L. (2001). The Quaternary and Pliocene Yellowstone volcanic field of Wyoming, Idaho, and Montana. *US Geological Survey Professional Paper*, 729 G, G1-G145. https://doi.org/10.3133/pp729G

Colón, D.P., Bindeman, I.N. & Gerya, T.V. (2018). Thermomechanical modeling of the formation of a multilevel, crustal-Scale magmatic system by the Yellowstone plume. *Geophysical Research Letters,* 45, 3873-3879. https://doi.org/10.1029/2018GL077090

Connolly, J.A.D., Holness, M.B., Rubie, D., Rushmer, T. (1997). Reaction-induced microcraking: an experimental investigation of a mechanism for enhancing anatectic melt extraction. *Geology,* 25, 591-594. http://doi.org/10.1130/0091-7613(1997)025<0591:RIMAEI>2.3.CO

Cousens, B.L. (1996). Magmatic evolution of Quaternary mafic magmas at Long Valley caldera and the Devils Postpile, California: Effects of crustal contamination on lithospheric mantle-derived magmas. *Journal of Geophysical Research*, 101(B12), 27673-27689. https://doi.org/10.1029/96JB02093

Dormand, J., (1996). Numerical Methods for Differential Equations: A Computational Approach, pp. 368, CRC Press LLC, New York.

Dufek, J. & Bergantz, G.W. (2005). Lower crustal magma genesis and preservation: a stochastic framework for the evaluation of basalt–crust interaction. *Journal of Petrology*, 46(11), 2167-2195. https://doi.org/10.1093/petrology/egi049

Fliedner, M.M., Klemperer, S.L. & Christensen, N.I. (2000). Three-dimensional seismic model of the Sierra Nevada arc, California, and its implications for crustal and upper mantle composition. *Journal of Geophysical Research*, 105(B5), 10899-10922. https://doi.org/10.1029/2000JB900029

Flinders, A.F., Shelly, D.R., Dawson, P.B., Hill, D.P., Tripoli, B. & Shen, Y. (2018). Seismic evidence for significant melt beneath the Long Valley Caldera, California, USA. Geology, 46(9), p. 799-802.Frassetto et al., 2011

Hildreth, W. (1979) The Bishop Tuff: evidence for the origin of compositional zonation in silicic magma chambers. In: Chapin, C.E. & Elston, W.E. (eds) Ash-flow tuffs. Geological Society of America Special Paper, 180, 43-75.

Hildreth, W. & Wilson, C.J.N. (2007). Compositional zoning of the Bishop Tuff. *Journal of Petrology*, 48(5), 951-999. https://doi.org/10.1093/petrology/egm007

Huppert, H.E. & Sparks, R.S.J. (1988). The generation of granitic magmas by intrusion of basalt into continental crust. *Journal of Petrology*, 29(3), 599-624. https://doi.org/10.1093/petrology/29.3.599

Jackson, M.D., Cheadle, M.J. & Atherton, M.P. (2003). Quantitative modeling of granitic melt generation and segregation in the continental crust. *Journal of Geophysical Research*, 108(B7), 2332, https://doi.org/10.1029/2001JB001050

Karakas, O. & Dufek, J. (2015). Melt evolution and residence in extending crust: Thermal modeling of the crust and crustal magmas. *Earth and Planetary Science Letters*, 425, 131-144. https://doi.org/10.1016/j.epsl.2015.06.001

Jolles J.S.R. (2020). Insights on the temperatures, mechanisms and timescales of voluminous (>600 km^3) high-SiO_2 (75-77 wt%) rhyolite melt generation at Long Valley, CA. University of Michigan, Ann Arbor, Ph.D. thesis

Lange, R.A. (1997). A revised model for the density and thermal expansivity of K_2O-Na_2O-CaOMgO-Al_2O_3-SiO_2 liquids from 700-1900 K: extension to crustal magmatic temperatures. *Contributions to Mineralogy and Petrology*, 130, 1-11. https://doi.org/10.1007/s004100050345

Lange, R.A. (2019). Evidence for rapid transport of rhyolite melt during hydrous partial melting of granitoid: the critical role of pre-existing aplite dikes and fluid-undersaturated conditions. *American Geophysical Union Fall Meeting Abstracts,* V44A-01.

Leeman, W.P., Annen, C. & Dufek, J. (2008). Snake River Plain – Yellowstone silicic volcanism: implications for magma genesis and magma fluxes. *Geological Society, London, Special Publications*, 304, 235-259. https://doi.org/10.1144/SP304.12

Metz, J.M. & Mahood, G.A. (1991). Development of the Long Valley, California, magma chamber recorded in precaldera rhyolite lavas of Glass Mountain. *Contributions to Mineralogy and Petrology*, 106(3), 379-397. https://doi.org/10.1007/BF00324565

Ochs, F.A. & Lange, R.A. (1999). The density of hydrous magmatic liquids. *Science*, 283(5406), 1314-1317. https://10.1126/science.283.5406.1314

Petford, N. & Gallagher, K. (2001). Partial melting of mafic (amphibolitic) lower crust by periodic influx of basaltic magma. *Earth and Planetary Science Letters*, 193(3-4), 483-499. https://doi.org/10.1016/S0012-821X(01)00481-2

Rushmer, T. (2001). Volume change during partial melting reactions: implications for melt extraction, melt geochemistry and crustal rheology. *Tectonophysics*, 342, 389-405. https://doi.org/10.1016/S0040-1951(01)00172-X

Sleep, N.H., (1988). Tapping of melt by veins and dikes. *Journal of Geophysical Research*, 93(B9), 10,255–10,272. https://doi.org/10.1029/jb093ib09p10255

Thurber, C., Zhang, H., Brocher, T. & Langenheim, V. (2009). Regional three-dimensional seismic velocity model of the crust and uppermost mantle of northern California. *Journal of Geophysical Research*, 114, B01304, https://doi.org/10.1029/2008JB005766

Wallace, P.J., Anderson, A.T. & Davis, A.M. (1999). Gradients in H_2O, CO_2, and exsolved gas in a large-volume silicic magma system: Interpreting the record preserved in melt inclusions from the Bishop Tuff. *Journal of Geophysical Research*, 104(B9), 20097-20122. https://doi.org/10.1029/1999JB900207

Yuan, H., & Dueker, K. (2010). Crustal structure and thickness along the Yellowstone hot spot track: Evidence for lower crustal outflow from beneath the eastern Snake River Plain. *Geochemistry, Geophysics, Geosystems*. 11, 3. https://doi.org/10.1029/2009GC002787

CHAPTER 2

High-Resolution Numerical Modeling of Heat and Volatile Trasfer from Basalt to Wall Rock: Application to the Crustal Column beneath Long Valley Caldera, CA

Citation:

Calogero, M. A., Hetland, E. A., & Lange, R. A. (2020). High-resolution numerical modeling of heat and volatile transfer from basalt to wall rock: Application to the crustal column beneath Long Valley caldera, CA. *Journal of Geophysical Research: Solid Earth*, 125, e2018JB016773.

doi: 10.1029/2018JB016773

Abstract

We present a high-resolution numerical model of the thermal evolution of the crustal column beneath Long Valley caldera, California, from which >800 km^3 rhyolite erupted over the last 2.2 Myr. We examine how randomly emplaced basaltic sills of variable thickness (10, 50, or 100 m) at various depth intervals (10-25 km) and at variable emplacement rates (5-50 m/kyr) gradually heat the crust and lead to a variably mixed crustal lithology (solidified mafic sills and pre-existing granitoid). We additionally explore the timescales over which dissolved water (~3 wt%) in a newly-emplaced basaltic sill exsolves during crystallization and is transferred to adjacent wall rock that is undergoing partial melting. We employ a finite-difference based technique, with variable spatial (≥1 m to ≥10 km) and temporal (<100 and >10^6 years) resolution, that enables dense analysis within and directly adjacent to a newly emplaced sill. Our results show that once ambient crustal temperatures reach ~500-600°C, subsequent injections of

basaltic sills lead to significant partial melting of adjacent wall rock (granitoid and solidified mafic sills) on time scales (10^1-10^2 years) that match those of exsolution of H_2O-rich fluid from basaltic sills. Large volumes of fusion (>10%) during fluid-undersaturated partial melting, combined with the pre-existing occurrence of aplite dikes, facilitates the development of melt-filled fractures that exceed the critical length for self-propagation. The advection of wall-rock partial melts (with a combined mantle-derived and crustal geochemical signature) to shallower depths will alter both the thermal and compositional profile of the middle-upper crust.

Introduction

Understanding the origin and evolution of voluminous rhyolitic magmas is of considerable interest because their formation fundamentally re-constitutes and differentiates continental crust, and they may lead to future "super-volcano" eruptions. The largest explosive eruptions (>100's km^3) that have occurred in the United States over the last 1 Myr were high-SiO_2 (75-77 wt%) rhyolites that erupted from the Long Valley caldera in eastern California (e.g. Hildreth and Wilson, 2007) and the Yellowstone caldera in Wyoming (e.g., Christiansen, 2001), both of which are located in the Basin and Range extensional province of the United States (Figure A-1).

Several previous studies have addressed the origin of silicic melts by modeling the thermal evolution of the crust as a function of basalt influx (e.g., Shaw, 1980; Huppert and Sparks, 1988; Petford and Gallagher, 2001; Jackson et al., 2003; Dufek and Bergantz, 2005; Annen et al., 2006; Leeman et al., 2008; Karakas and Dufek, 2015; Colón et al., 2018). These studies examined how different rates of basalt emplacement heat the crust, leading to the onset of crustal melting, and over what spatial and temporal scales this process might occur. These

models additionally track the cooling and crystallization of basaltic intrusions, and thus the geochemical evolution of differentiated mantle melts. Some studies have focused on the emplacement of basalts in the lowermost crust (e.g., Jackson et al., 2003; Dufek and Bergantz, 2005; Annen et al., 2006), which is relevant to subduction-zone settings, whereas others have focused on extensional environments where basalts ascend higher into the middle crust (e.g., Leeman et al., 2008; Karakas and Dufek, 2015; Colón et al., 2018). There is general consensus that both interstitial melts from the basalt intrusions and partial melts of pre-existing crust contribute to the formation of silicic melts, but in a complex, multi-stage process. For example, in the case of the Yellowstone rhyolites, Simakin and Bindeman (2012) and Bindeman and Simakin (2014) have modeled the late-stage, shallow (<10 km) re-melting of hydrothermally altered crust that occurred to form many of the low $\delta^{18}O$ Yellowstone rhyolites. Conversely, Leeman et al. (2008) addressed the initial emplacement of basalt into the middle crust (10-30 km) that produced evolved Yellowstone melts from both pre-existing crust and mantle-derived basalt. More recently, Colón et al. (2018) examined the crustal-scale consequences of basalt emplacement/entrapment in the middle crust beneath Yellowstone.

The purpose of this study is to examine how the process of basalt emplacement into the granitoid middle to upper crust beneath the Long Valley caldera, California, drives the production of hydrous rhyolitic melts. We build on the crustal-scale approach taken in previous studies (e.g., Dufek and Bergantz, 2005; Annen et al., 2006; Leeman et al., 2008; Karakas and Dufek, 2015; Colón et al., 2018), where the thermal evolution of the entire crustal column in response to basalt influx is simulated. However, this study differs from previous work by examining key processes that occur at relatively short length and time scales (on the order of meters and years, respectively), which requires a numerical model that can achieve such high

spatial and temporal resolution while still being able to simulate the entire lithospheric column over a time scale of millions of years.

Our goal in this study is to pay particular attention to the formation of localized partial melts along the wall-rock margins of basaltic sills within the first 10's to 100's of years of their emplacement (e.g., Lim et al, 2012), even when long-term (>1 kyr) ambient temperatures remain sub-solidus (i.e., <650°C). This is a process that has not yet been quantitatively modeled in the literature and may contribute to the formation, segregation, and ascent of evolved partial melts of a mixed lithology (granitoid and mafic sills), leading to their gradual accumulation in the upper crust. These partial melts will have a combined mantle-derived and crustal geochemical signature. The time scale for the segregation and ascent of these localized partial melts is also considered.

Another focus of this study is the examination of how water is transferred from basaltic sills to partial melts of the crust. One of the defining features of the voluminous (>400 km^3) Early Bishop rhyolite is its high concentration of water (≤6.5 wt%; Wallace et al., 1999; Anderson et al., 2000). The source of this water cannot be the pre-existing granitoid crust, with a bulk water content <0.6 wt% held in biotite and hornblende (Bateman, 1992), and instead must be derived from the Long Valley basalts (e.g., Cousens, 1996), which erupted in close spatial and temporal association with the rhyolites of Long Valley caldera. Understanding this transfer of water is of major importance because melt fraction-temperature (F-T) curves depend strongly on how much water is present.

Tectonic/Geologic Setting for Numerical Modeling

The numerical simulations presented in this study are designed to be applicable to the Long Valley magmatic system, located in eastern California along the western edge of the Basin and Range province (Figure A-1b). Between 2.2 and 0.8 Ma, ~100 km^3 of rhyolite erupted to form the Glass Mountain complex (Metz and Mahood, 1991; Hildreth, 2004), which was followed by the climactic eruption of the >600 km^3 Bishop Tuff within ~6 days (Wilson and Hildreth, 1997) to form the Long Valley caldera at ~765 ka (Andersen et al., 2017). Soon after, the eruption of ~100 km^3 of rhyolite (named "Early" post-caldera rhyolite by Bailey, 1989) occurred within the caldera between ~750-640 ka (Hildreth et al., 2017). Over the last 600 kyr, ≤8 km^3 of rhyolite have erupted inside the margins of the Long Valley caldera (Hildreth, 2004; Simon et al., 2014). A combined volume of >800 km^3 of rhyolite has erupted within the Long Valley volcanic system over the last 2.2 Myr, but over discrete, punctuated time periods characterized by highly variable eruption rates.

This voluminous production of rhyolite was driven by an influx of basalt into the crustal column beneath Long Valley caldera (e.g., Hildreth and Wilson, 2007). Seismic studies indicate a mid-crustal (~10-20 km depth) low-velocity zone beneath Long Valley (Thurber et al., 2009; Frassetto et al., 2011; Flinders et al., 2018), consistent with the presence of melt and/or fluid. The Long Valley basalts were formed by partial melting of subduction-modified mantle lithosphere (Cousens, 1996), which was triggered by upwelling asthenosphere due to lithosphere delamination beneath the eastern Sierra Nevada (e.g., Manley et al., 2000; Saleeby et al., 2003; Zandt et al., 2004).

Numerical Model

Temperature and melt fraction are solved for using the 1-D non-homogeneous transient thermal diffusion equation:

$$\rho C_p \frac{\partial T}{\partial t} + \rho L \frac{\partial F}{\partial t} = \frac{\partial}{\partial x} k(x) \frac{\partial T}{\partial x} \quad (1)$$

where ρ is density, C_p is specific heat capacity, L is the latent heat, $k(x)$ is thermal conductivity, T is temperature, F is melt fraction, t is time, and x is depth. Temperature and melt fraction are related by a piecewise linear function, $F(T)$, given in general as

$$F(T) = \begin{cases} 0, & T \leq T_0 \\ m_i T + b_i, & T_{i-1} \leq T < T_i \\ 1, & T \geq T_p \end{cases} \quad (2)$$

where $T_0 = T_{solidus}$ and $T_p = T_{liquidus}$, and m_i and b_i are the slope and intercept, respectively, for $i \in [1, p]$ segments of the temperature verses melt fraction relationship. Approximating the melt fraction-temperature relationship with $F(T)$ allows for the general relationship

$$\frac{\partial F}{\partial t} = \phi \frac{\partial T}{\partial t} \quad (3)$$

where $\phi = 0$ if $T < T_{solidus}$ or $T > T_{liquidus}$, and $\phi = m_i$ otherwise. Using Equation (3), Equation (1) then reduces to

$$\left(\rho C_p + \phi \rho L\right) \frac{\partial T}{\partial t} = \frac{\partial}{\partial x} k(x) \frac{\partial T}{\partial x} \quad (4)$$

The 1-D compaction and expansion due to solidification and melting, respectively, are approximated by

$$\frac{dX}{dt} = \varphi X \frac{dF}{dt}, \quad (5)$$

where X is the height of the column of the region undergoing solidification or melting, and φ is a scalar representing the percent height change during the phase transition.

Equation (4) is solved in non-dimensional form using a numerical method of lines (MOL) technique on a non-uniform spatial grid and with adaptive time resolution. Discretizing the spatial coordinate as x_j, $j \in [1, N]$, we denote $T(x_j, t) = T_j$, which for brevity is not written as a function of t. The spatial finite difference approximation of Equation (4) is

$$\frac{\partial T}{\partial t} \simeq \frac{1}{\rho(C_p + L\phi_i)} \frac{\left(\frac{T_{j+1} - T_j}{x_{j+1} - x_j}\right) k_{j+\frac{1}{2}} - \left(\frac{T_j - T_{j-1}}{x_j - x_{j-1}}\right) k_{j-\frac{1}{2}}}{\frac{1}{2}(x_{j+1} - x_{j-1})}, \tag{6}$$

where $k_{j+\frac{1}{2}} = \frac{k_{j+1} + k_j}{2}$ and $k_{j-\frac{1}{2}} = \frac{k_{j-1} + k_j}{2}$. Equation (6) is numerically integrated at x_j using a standard Runge-Kutta method with adaptive time steps (e.g., Dormand, 1996). In the adaptive time-stepping method, the nodal temperatures at each time step are calculated using a proposed time step with both 2nd and 3rd order Runge-Kutta integration schemes. If the maximum difference in the solutions is larger than a specified tolerance (here we use 10^{-5} in non-dimensional temperature), the current time step is decreased, and the temperatures for the next time step are recalculated using the two Runge-Kutta schemes and the smaller time step. We continue to decrease the time steps until the 2nd and 3rd order solutions are within tolerance. For each rejected time step, the time step is decreased to $0.9delT(tolerance/error)^{1/3}$, where error is the maximum absolute difference in the temperature solutions and delT is the previously tested time step (e.g., Noda et al., 2009; Hetland et al., 2010). Once the solutions converge within tolerance, we take the 3rd order solution as the temperatures for the next time step, and the next time step is also $0.9delT(tolerance/error)^{1/3}$ (i.e., if the error is larger than 1.372 of the tolerance the time step grows). The minimum nodal spacing controls the stability of each time step, so the solution is always within stability for the larger nodal spacings on the non-uniform spatial grid. Using this scheme, the time step decreases when the temperature gradients are high, and then gradually increases after the spatial variations in the temperature gradients subsequently

subside. Once the temperatures are calculated at a given time step, the nodal melt fraction is solved for using Equation (2). The melt fraction is then used to calculate the material density, using prescribed densities of the solid and the liquid phases. A first-order discretized form of Equation (5) is integrated to find the compaction (and/or expansion) due to changes in melt crystallization (and/or melt formation).

In all of the simulations presented in this study, the initial domain thickness (from the surface to depth) is 45 km. Over this domain, N nodes are initially distributed evenly with depth. The material properties of each node are assigned based on their depth, such that if a node is within the boundaries of the lower crust, it is assigned material properties of the lower crust, etc. (Table 2-1). The first sill is then injected into the model domain (all basalt sills in this study have an initial temperature of 1150ºC and melt fraction of 1), and then the nodes are adjusted as described below, before solving for the temperatures. Temperatures are calculated at each time step as described above, with additional basalt sills periodically injected into the crust at specified emplacement rates.

After each sill is injected, the domain thickness is increased by the thickness of the sill, and the temperature and melt fraction fields below the sill are advected downward. With each emplacement, new nodal positions are calculated using a node placement optimization motivated by a moving mesh MOL (MM-MOL) technique (Huang and Russell, 2011). This allows temperatures to be resolved where thermal gradients are high, without overly discretizing regions of the domain with near-linear temperature gradients. In this node adaptation scheme, the spatial resolution is increased in regions of the model domain with high curvature of the temperature field and/or with high melt faction, while node spacing is decreased where the temperature has

minimal curvature and there is no melt present. To adapt the node distribution, we use the mesh density function

$$\delta^* = 1 + |\nabla^2 T|^{\frac{1}{4}} + \gamma F, \quad (7)$$

and solve for optimal nodal spacings that are proportional to δ^*, under the constraint of a prescribed minimum node spacing and that the entire domain is covered by nodes. The proportionality factor γ is determined such that the computation domain contains a fixed number of nodes (i.e., nodes are not added or removed from the domain). To avoid singularities in the temperature field, we smooth the mesh density function, following the MM-MOL method (Huang and Russell, 2011). Compression (expansion) during crystallization (melting) is then accounted for by perturbing the nodal positions. Finally, the node positions may be slightly perturbed in order to ensure that there is at least one node between all material boundaries, including locations of all past sills. After the node positions are adjusted, the temperature and melt fraction fields, as well as all material parameters, are mapped from the old mesh to the new mesh using a linear interpolation.

The numerical solution is implemented in Matlab. With 600 total nodes over an initial domain thickness of 45 km, the largest node spacing after a sill injection is about 130 meters, and occurs at the edges of the model domain (close to the surface and the base of the domain). Aside from some resolution tests, the main simulations presented in this study use a minimum spatial resolution of 1 meter, which corresponds to a minimum temporal resolution of about a minute. Using a spatial resolution of at least 5 meters, the smallest time step is ~6 days. Due to the adaptive time-stepping algorithm, as temperatures diffuse and basalt sills crystallize, temporal resolution increases, and 1000 years after a sill injection, the time step increases to ~10 days and ~8 months, respectively, for 1 and 5 meter minimum spatial resolutions. Simulations of the

thermal evolution of the crust after 200 sill injections take ~1 and ~14 hours for 1 and 5 meter minimum spatial resolutions, respectively, on a circa 2012 desktop workstation. Results from a benchmark simulation of basalt intruding basalt and subsequent cooling is provided in the supplementary information (Figure A-2).

Model Parameters

An initial 20°C/km linear geotherm is assumed prior to injection of the basaltic sills, which is consistent with the seismically imaged lithosphere-asthenosphere boundary at ~60 km for the Basin and Range (Levander and Miller, 2012), where a temperature of 1200°C marks the lithosphere-asthenosphere boundary (LAB). This relatively cool geotherm of 20°C/km is also consistent with the volcanic hiatus in the Long Valley region from 8-4.5 Ma prior to renewed magmatism in the region (Bailey, 1989; Du Bray et al., 2016). The initial crustal composition is assumed to be granitoid from the surface to 32 km depth, mafic amphibolite from 32–35 km depth, and mantle lithosphere below 35 km (Figure A-3; Fliedner et al., 2000). The bulk composition used for the granitoid upper crust beneath Long Valley caldera is the average composition of upper crust from Rudnick and Gao (2014). Note that several whole-rock compositions of granitoid from the Sierra Nevada batholith (e.g., Bateman, 1992; Coleman et al., 2012) broadly overlap this average upper crust composition. The composition of basalt used in this study is the average of several Long Valley basalts (50.9 wt% SiO_2, 1.5 wt% TiO_2, 15.7 wt% Al_2O_3; 8.2 wt% FeO_T, 8.0 wt% MgO, 9.1 wt% CaO, 3.6 wt% Na_2O, 2.2 wt% K_2O and 0.6 wt% P_2O_5).

In this study, we initially focus on the emplacement of 5 km of basalt over a 1 Myr time period, in the form of 50-m thick sills emplaced every 10 kyr, into the crust (5 m/kyr). This rate of emplacement was also employed in Leeman et al. (2008) in their thermal model of the crust in

response to Yellowstone hot spot magmatism. Different sill thicknesses (10 and 100 m) and different time intervals for the emplacement of basalt are additionally explored, leading to different basalt flux rates (~5-50 m/kyr). Because rhyolite eruption rates out of the Long Valley volcanic system have been highly variable, from ~0.1 km^3/kyr between 2.2 and 0.8 Ma (Hildreth, 2004) to >600 km^3/week (Wilson and Hildreth, 1997), the effect of variable basalt emplacement rates, including relatively high rates over short time periods (e.g., 50 m/kyr for ≤ 100 kyr duration), merits evaluation.

We prescribe a sill emplacement history, either placing sills at the same fixed depth or randomly placing them within a depth interval of the upper crust. Because the tectonic setting is continental extension (and not subduction), basaltic sills are emplaced in the middle (not lower) crust. Note that mid-crustal depth intervals (10-25 km) are broadly consistent with seismic evidence of a mid-crustal sill complex (MSC) beneath the Snake River Plain due to the influx of basalt from the Yellowstone plume (Stachnik et al., 2008; Yuan et al., 2010), which in turn drove the formation of voluminous rhyolite along the Yellowstone hot spot track (Leeman et al., 2008; Colón et al., 2018). In all of the simulations presented in this paper, we assume that all injected basalt sills have an initial uniform temperature of 1150ºC and are emplaced at fixed time intervals. Nodes within the sills, both the most current and previously solidified sills, are assigned the material properties of basalt (Table 2-1), and these properties, apart from density, do not change after the sills have solidified. Nodes outside of the sills are assigned material properties of the wall rock (Table 2-1), relative to the evolving material boundaries with each emplacement.

	Symbol	Mantle	Lower Crust	Granitoid	Basalt
Density (solid) kg/m^3	ρ_S	3400	3050	2650	3100
Density (melt) kg/m^3	ρ_M			2650	2830
Specific Heat $J/(kg \cdot K)$	Cp	1131	1390	1370	1480
Latent Heat J/kg	L	0	3.5E+05	2.7E+05	4.0E+05
Conductivity $J/(s \cdot m \cdot K)$	k	3.4	2.6	3	2.6
Melt Compaction		0	0	0	0.1

Table 2-1. Material Properties for Simulations. References: ρ, Holbrook et al. (1992) and Kay et al. (1992); Cp and L, Bohrson & Spera (2001); k, Chapman & Furlong (1992) and Hofmeister (1999).

When sills are emplaced, all material boundaries below the sill margin are moved down by the sill thickness. In the case where sills are inserted at a fixed depth, the top of each new sill is at the same depth, and previously emplaced sills are pushed down, creating a contiguous depth range of uniform basaltic composition. When sills are inserted randomly within a depth range, a mixed lithology of alternating granitoid and solidified mafic sills is created. The minimum nodal spacing of 1 m ensures that a new sill of 50 m is resolved with 51 nodes as it solidifies. Hereafter, in this text, the term "basaltic sill" refers to a newly emplaced sill that is undergoing crystallization, whereas the term "mafic sill" refers to a previously solidified basaltic sill.

Basalt Crystallization Melt Fraction-Temperature Curve

We assume an initial temperature of 1150°C and an initial water concentration of 3 wt% H_2O are used for each basaltic sill. This water content is based on analyses of ≤3 wt% H_2O in olivine-hosted melt inclusions of nearby Pliocene-Quaternary basalts erupted along the eastern margin of the Sierra Nevada range (Gazel et al., 2012). To determine the basalt equilibrium crystallization curve with temperature, the thermodynamic model rhyolite-MELTS (Gualda et al. 2012) was used at 0.3 and 0.5 GPa. The results are shown in Figure 2-1a and are parameterized into four linear segments. According to the MELTS calculation, latent heat is distributed nearly linearly as a function of degree of crystallization for this melt composition, which allows total

enthalpy (L) to be treated as a linear function of melt fraction. The effect of a non-linear release of latent heat across the liquidus-solidus interval is explored in the results.

Melt Fraction-Temperature (F-T) Curves for Crustal Melting

Melt fraction versus temperature curves are needed for both solidified mafic sill and granitoid lithologies, and they will each depend strongly on the total amount of H_2O present. Two end-member H_2O conditions for each lithology are evaluated: fluid-absent and finite fluid-present (i.e., fixed amount of H_2O present; not unlimited). In all cases, the F-T curves are calculated using the rhyolite-MELTS thermodynamic model of Gualda et al. (2012) and are plotted in Figure 2-1.

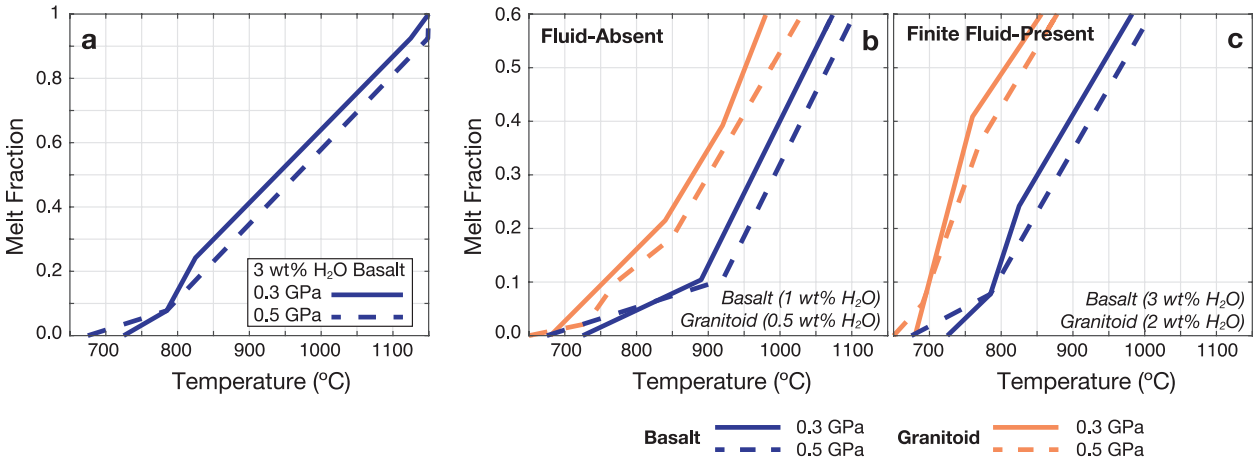

Figure 2-1. Melt fraction vs temperature (F-T) relationships for mafic sills and granitoid, calculated with rhyolite MELTS (Gualda et al., 2012). (a) Basalt crystallization at 0.3 GPa (solid) and 0.5 GPa (dashed). (b) Case 1: Fluid-absent granitoid (orange) and mafic sill (blue) melting. (c) Case 2: Finite fluid-present granitoid and mafic sill melting.

Case 1: Fluid-absent mafic sills and granodiorite

In the first case, it is assumed that after complete crystallization of the basaltic sills in the granitoid crust, approximately one-third (1 wt% H_2O) of the initial 3 wt% H_2O dissolved in the melt is retained in the mineral assemblage in the form of biotite and/or hornblende, which leaves ~2 wt% H_2O as a fluid phase under sub-solidus conditions. In this first-case scenario, it is

assumed that this fluid phase is completely lost from the sill and surrounding crustal rocks (i.e., through ascent along grain boundaries and/or fractures). This leaves a fluid-absent mafic sill with a bulk H_2O content of ~1 wt%. Similarly, it is assumed that the surrounding granitoid rock (with a bulk composition similar to average upper crust; Table 2-1) is also devoid of any fluid phase, and H_2O is only present in the form of biotite and hornblende (<10% of each phase; Bateman, 1992). In this case a total H_2O content of ~0.5 wt% is assumed for the granodiorite wall rock. The F-T curves for the fluid-absent mafic sill and granodiorite, with 1 and 0.5 wt% H_2O respectively, are calculated using rhyolite-MELTS and are illustrated in Figure 2-1b. Note that despite the lower H_2O content, the fluid-absent granodiorite has a higher melt fraction relative to the fluid-absent mafic sill at any given temperature above the solidus. For example, at 800°C and 0.3 GPa, the granodiorite and mafic sill are predicted to contain ~15 and ~5% melt, respectively.

Case 2: Finite fluid-present mafic sills and granodiorite

In the second case, it is assumed that during late-stage crystallization of the basaltic sills, ~2 wt% H_2O exsolves as a fluid phase and reaches the interface between the sill margin and the granodiorite wall rock. During transient heating of wall rock adjacent to a newly emplaced sill, an initially fluid-present melting curve at the solidus for granodiorite is employed, based on a whole-rock composition of 2 wt% H_2O, which becomes fluid undersaturated as melt fraction increases. Also shown is an initially fluid-present melting curve for the solidified mafic sills at the solidus, based on a whole-rock composition of 3 wt% H_2O (2 wt% H_2O fluid + 1 wt% in hydrous mineral phases), which becomes fluid undersaturated as melt fraction increases. A comparison of the two initially fluid-present F-T curves (Figure 2-1c), which become fluid undersaturated with melt fraction, shows that the granodiorite wall rock produces a far greater

melt fraction than the solidified mafic sills at a given temperature (e.g., 30% vs. 5% at 750°C and 0.5 GPa). We use the term "finite fluid-present" to distinguish the F-T curves in Figure 2-1c (case 2), which are based on a finite (i.e., fixed) amount of water in the system, from F-T curves that are fluid saturated under all melt fraction conditions (i.e., unlimited amount of water available).

Results

Crustal-Scale Thermal Evolution

We ran simulations with the following parameters varied: (1) sill emplacement style (e.g. fixed versus random emplacement depth); (2) minimum spatial resolution (25, 5, and 1 m); (3) non-linear distribution of latent heat in basaltic sills; (4) thickness of sills (10, 50 and 100 m); (5) depth range of sill emplacement; (6) rate of sill emplacement (i.e., different time intervals over which a fixed amount of basalt is emplaced in the crust); and (7) fluid-absent vs. finite fluid-present F-T curves for wall rock (granodiorite and solidified mafic sills). In each of these cases, all other variables were held constant. The goal was to evaluate first-order effects on the thermal evolution of the crust at the kilometer length scale, as well as the resulting proportions of mafic sills and granitoid in the crustal column. Both crustal temperature and the extent of a mixed lithology in the crustal column must first be determined before the extent of any partial melting along the margins of newly emplaced sill can be evaluated.

Fixed vs. Random Depth Emplacement

Previous studies have examined both fixed and random emplacement of basaltic sills (e.g., Annen et al., 2006; Leeman et al., 2008). For comparative purposes, we also consider both emplacement schemes. In each simulation, the initial sill temperature (1150°C) and emplacement rate (50-m sill every 10 kyr) are held constant. In the fixed-depth emplacement scheme, new sills are injected with their top surface at 10-km depth, the shallowest depth chosen in Leeman et al. (2008). In the random-depth emplacement scheme, the initial depth range for sill emplacement is 10-15 km, with the upper depth limit held constant at 10 km and the lower depth limit moved down by the thickness of each new sill after it is emplaced. The simulations were run for 1 Myr

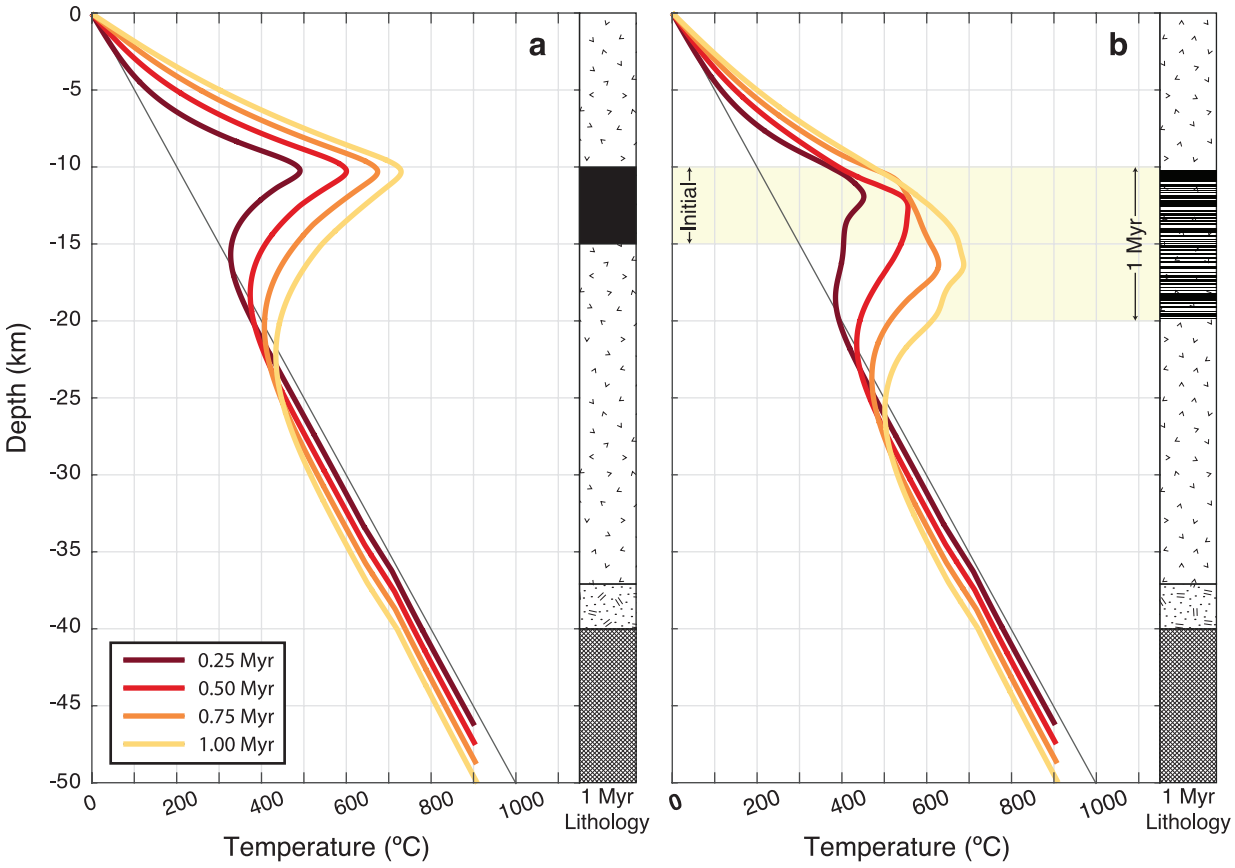

Figure 2-2. Thermal profiles for (a) fixed-depth emplacement at 10 km depth and (b) random-depth emplacement with an initial depth range of 10-15 km. Emplacement rate is 5 km/Myr in both cases (50-m thick sill every 10 kyr). Profiles are shown after 0.25 Myr (maroon), 0.5 Myr (red), 0.75 Myr (orange), and 1 Myr (yellow). The crustal lithology after 1 Myr for each emplacement scheme is included, where black is basalt sills and the other rock types

are defined in legend in Figure A-3. The thin black line denotes the initial geothermal gradient. Fluid-absent F-T curves at 0.3 GPa are used for the wall rock (Figure 2-1b).

in both cases, resulting in 5 km of basalt added to the crustal column. In the fixed-depth emplacement scheme, the added basalt sills are contiguous, whereas in the random-depth emplacement scheme, a mixed lithology results between 10-20 km depth, with an average 1:1 ratio of mafic sills to granitoid. The evolution of the thermal profile at 0.25, 0.5, 0.75, and 1 Myr for each emplacement scheme is shown in Figure 2-2. The thermal profiles shown are those 10 kyr after the most recent sill emplacement (i.e. immediately before the next scheduled emplacement of a 50-m sill). For both emplacement schemes, all basaltic sills are fully crystallized after 1 Myr and there are no crustal depths hotter than 725°C.

In the fixed-depth emplacement simulation, after 1 Myr, the maximum crustal temperature is ~725°C and occurs inside the most recently emplaced basalt sill, immediately below 10-km depth (i.e., near the interface with granitoid crust). In this simulation, temperatures are >600°C over ~2-km thickness of granitoid crust immediately above the contiguous mass of basaltic sills. In contrast, in the random-depth emplacement simulation, after 1 Myr, the maximum crustal temperature is ~686°C, again inside the most recently emplaced basalt sill. However, the amount of granitoid (distinct from mafic sills) heated >600°C is nearly twice as thick at ~4 km. The increase in thickness of granitoid that is heated by the random emplacement of sills reflects the more efficient transfer of heat from the basaltic sills to the surrounding granitoid when the 50-m thick sills are spread out throughout the crustal column (e.g., Dufek and Bergantz, 2005). A microscale example of this phenomenon is described in Spera and Bohrson (2018).

Variation in Minimum Spatial Resolution

To evaluate the effect of the spatial resolution of our finite-difference model on crustal thermal profiles, we ran the same random-emplacement simulation (i.e., with identical sill history) from Figure 2b, using minimum spatial resolutions of 1, 5, and 25 m. The final temperature profiles over the depth range where most sills were emplaced are shown in Figure 2-3. For reference, the center of the last sill emplaced is at a depth of 16.62 km. After 1 Myr the maximum temperatures in the 25-m and 5-m cases are ~19 and ~4ºC, respectively, colder than the 1-m case. The most precise results are obtained with the highest spatial resolution (1 m), which is used for all simulations presented in this study.

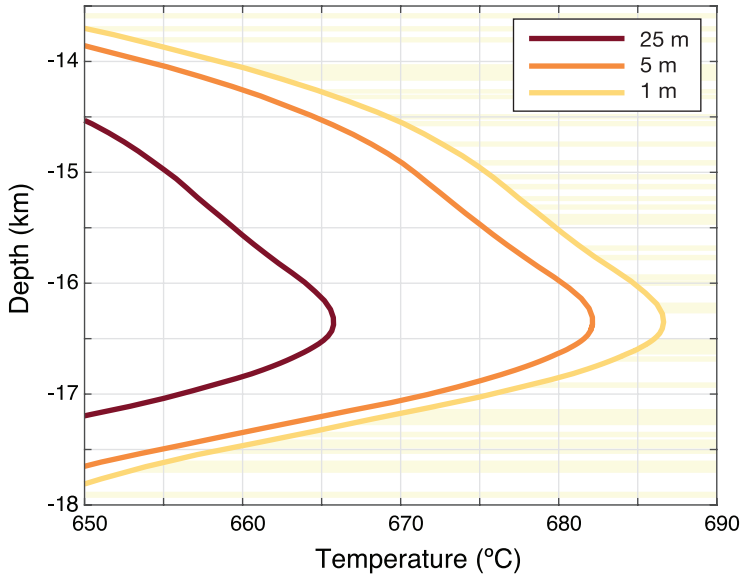

Figure 2-3. Thermal profiles after 1 Myr of random-depth emplacement (50 m sill every 10 kyr; fluid-absent at 0.3 GPa, Figure 2-2b) for three minimum spatial resolutions, 25 m (maroon), 5 m (orange), and 1 m (yellow). Pale horizontal background blocks mark the sill positions at 1 Myr. The most accurate results are for the highest spatial resolution (1 m).

Varying Distribution of Latent Heat across the Liquidus-Solidus Interval

In Equation (1), if F>0 then the latent heat (L) is released linearly as a function of % crystallization. This is the default case for all simulations presented in the main body of the text. To test whether crustal-scale thermal profiles are sensitive to how latent heat is distributed across

the liquidus-solidus interval of basaltic sills, we added an additional step during the Runge-Kutta time-stepping, which adjusts the proportion of latent heat released across the liquidus-solidus interval (Figure A-4a). In the first test case, 75% of the latent heat is released in the first 25% of crystallization, whereas in the second test case, only 25% of the latent heat is released in the first 75% of crystallization, and the remaining 75% of latent heat is released in the last 25% of crystallization. In all simulations, the same total amount of latent heat is released during crystallization of the basaltic sills, and all other parameters are unvaried, including the random sill emplacement history (same as that in Figure 2-2b). The resulting thermal profiles at 1 Myr are within ≤5 degrees for all three cases (Figure A-4b), which shows that variations in how latent heat is distributed across the liquidus-solidus interval have a negligible effect on crustal-scale thermal profiles.

Variation in Thickness of Basaltic Sills

The effect of varying the thickness of basaltic sills (10, 50 and 100 m), which are emplaced at an identical long-term rate (5 km/1 Myr) and initial depth interval (10-15 km), on the crustal-scale thermal profile was also explored. There is no difference in the temperature profile through the crust when 10- and 50-m thick sills are randomly emplaced (Figure A-5). However, three simulations of random emplacement of 100-m thick sills every 20 kyr were run, producing variable thermal profiles after 1 Myr. For one simulation, the thermal profile closely matches those for the 10- and 50-m thick sill emplacement runs, whereas other random sill histories produced higher temperature concentrations at shallower or deeper depths (see Figure A-5b). The differences in the three 100-m sill thermal profiles is due to the random (and thus

varying) emplacements of relatively thicker and fewer basaltic sills into the crustal column, particularly controlled by the final few sill emplacements in each simulation.

Variation of Emplacement Depths and Depth Ranges

In order to test the effect of varying the depth ranges over which basaltic sills are emplaced, we ran simulations of random sill emplacements (50 m/10 kyr) over a 1 Myr time interval with variable initial depth ranges: (1) 10-15 km, (2) 15-20 km, and (3) 10-20 km. In each of the three test cases, we ran four realizations of random sill emplacements and took their average thermal profile after 1 Myr (Figure A-6). In all cases, a total of 5 km of basalt was emplaced in the respective depth ranges after 1 Myr (final ranges: 10-20 km, 15-25 km, and 10-25 km respectively). In the models where the initial depth range spans 5 km (10-15 and 15-20 km), the final sill:granitoid ratio is 1:1, whereas when the initial depth range spans 10 km (10-20 km), the resulting sill:granitoid ratio is 1:2. The most important observation in Figure A-6 is that the depth interval over which basaltic sills are emplaced strongly affects the proportion of mafic sills embedded within the granitoid crust once temperatures reach ~600°C. In other words, the deeper and broader the initial depth interval of sill emplacement (at a constant rate), the lower the amount of basalt that is required to bring crustal temperatures to ~600°C.

Variation of Sill Emplacement Rate

We next explored the thermal effect of emplacing the same 5-km thickness of basalt over different time intervals (1, 0.5 and 0.1 Myr). In all cases, the initial depth range is 10-15 km, and after 100 sills are emplaced the average final sill:granitoid ratio is 1:1 between 10-20 km depth.

The only difference among the three simulations is the frequency with which the 50-m thick sills are emplaced, every 10, 5 and 1 kyr, respectively.

The results for these three simulations are compared in Figure 4, using the same sill injection histories shown in Figure 2-2b (100 total sills). The lowest basalt emplacement rate (5 km over 1 Myr) results in a thermal profile that is everywhere <700°C, with a maximum temperature of 686ºC 10 kyr after the last sill is emplaced. In the second simulation, the same 5 km of basalt is emplaced in half as much time (500 kyr), and the thermal profile is notably hotter, with ~4 km of crust reaching temperatures >700°C 5 kyr after the 100^{th} sill is emplaced, and a maximum at 752°C. In the third simulation, where 5 km of basalt is emplaced within 100 kyr (50 m/1 kyr), ~7.7 km of crust is heated above 700°C 1 kyr after the 100^{th} sill is emplaced, including ~2 km in excess of 800°C; the maximum temperature is 836°C.

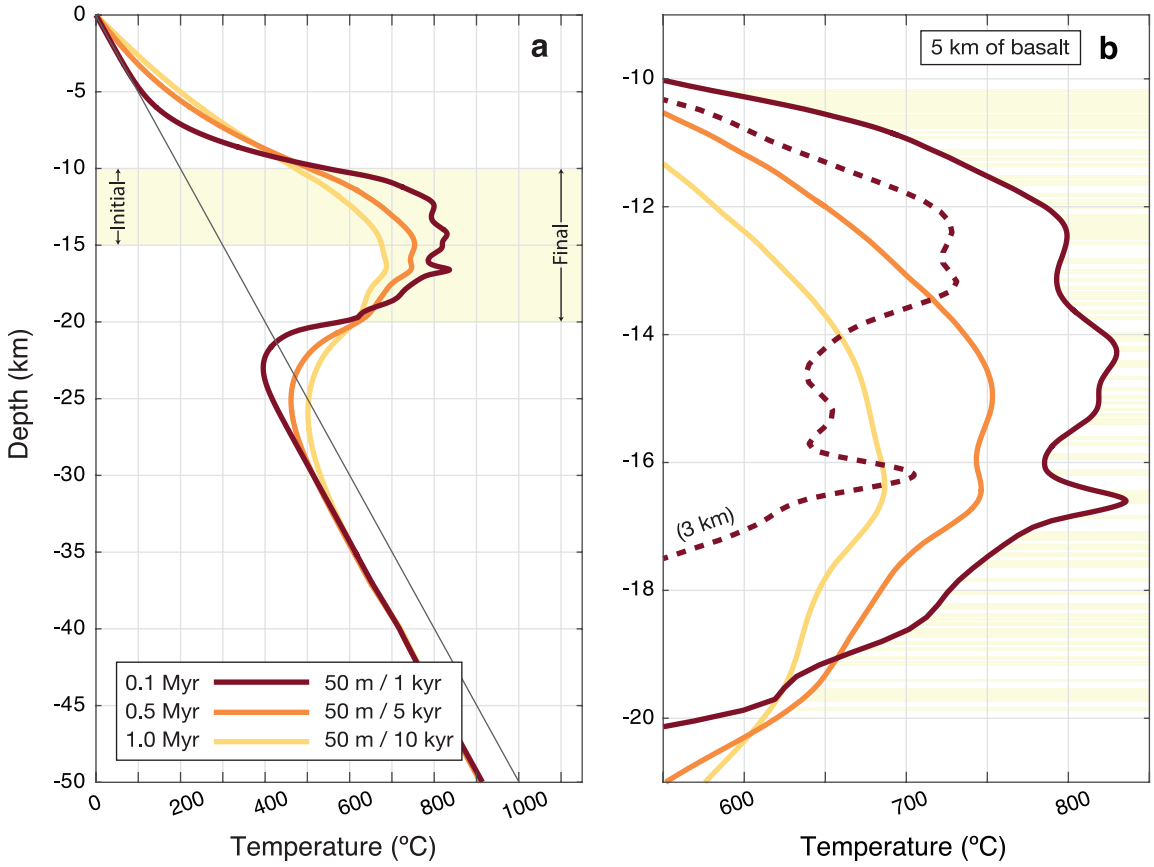

Figure 2-4. Thermal profiles for different rates of random emplacement: 5 km over 1 Myr (yellow), 0.5 Myr (orange), and 0.1 Myr (maroon). (a) Thermal profile over 0-50 km depth with initial and final emplacement ranges marked in yellow. (b) Zoomed-in thermal profile (9-21 km depth). Yellow shading denotes all sill positions after 5 km of basalt have been emplaced. All three simulations use the same sill position history and fluid-absent F-T curves at 0.3 GPa (Figure 2-2b). At depths above and below the sill emplacement range, the crustal temperatures are colder when emplacement rates are higher, because there is less time for heat from the basalt to diffuse into cooler regions. This is also why the thermal profile is less smooth and more variable over the 10-20 km depth interval for the shortest time interval tested (100 kyr).

These combined results (Figure 2-4) show that the time interval over which a fixed amount of basalt is placed into the crust has a notably strong effect on the thermal profile through the crust, as found in previous studies (e.g., Dufek and Bergantz, 2005; Annen et al., 2006; Leeman et al., 2008). Over shorter time intervals, there is insufficient time for the heat from the basaltic sills to diffuse away, allowing the crustal range with a 1:1 basalt:granitoid lithology to attain markedly higher temperatures. Conversely, less basalt (3 vs 5 km) is required at high vs. low emplacement rates (50 vs. 5 m/kyr) to reach a similar temperature profile in the crust (Figure 2-4b, dashed).

F-T Curves for Granitoid Wall Rock: Fluid-Absent vs. Finite Fluid-Present

The final parameter that we explored is the effect of variable melt-fraction vs temperature curves for the wall rock under fluid-absent (case-1) and finite fluid-present (case-2) conditions. The latent heat of fusion term in Equation (4) during partial melting acts as a heat sink (opposite to the release of heat during basalt crystallization), and hence the choice of the F-T curve for the wall rock can affect crustal-scale thermal profiles. The magnitude of this effect is illustrated in Figure 2-5 after 100 sill emplacements at two rates, 50 m/10 kyr and 50 m/5 kyr (1 and 0.5 Myr, respectively). For the same amount of basalt injected into the crust (5 km), the lower vs. higher emplacement rates heat ~4 vs. ~7 km of crust above 650°C (Figure 2-5a).

In these simulations, there is a marked difference in the amount of partial melt that is formed, depending on which F-T curve is applied to the wall rock (fluid-absent vs. finite fluid-present), examined in Figure 2-5b. For the lower emplacement rate, the difference in the melting curves leads to the presence (~2% melt) vs. absence of melt. For the higher emplacement rate (i.e. hotter crustal temperatures), the fluid-absent melting curve leads to the formation of less partial melt (<5%) across 3.6 km of crust, whereas the finite fluid-present melting curve leads to the formation of partial melt across 4.5 km of crust, with >20% melt present over nearly 3 km. Importantly, the difference in the amount of partial melt that is formed affects the crustal-scale thermal profile. The latent heat of fusion term causes cooling, the magnitude of which is dependent on the amount of partial melt that is formed. For the high-emplacement rate scenario (Figure 2-5b), the difference between ~5% vs. ~25% melt present (fluid-absent vs. finite fluid-present F-T curves) in the crustal column leads to an average cooling of ~15°C.

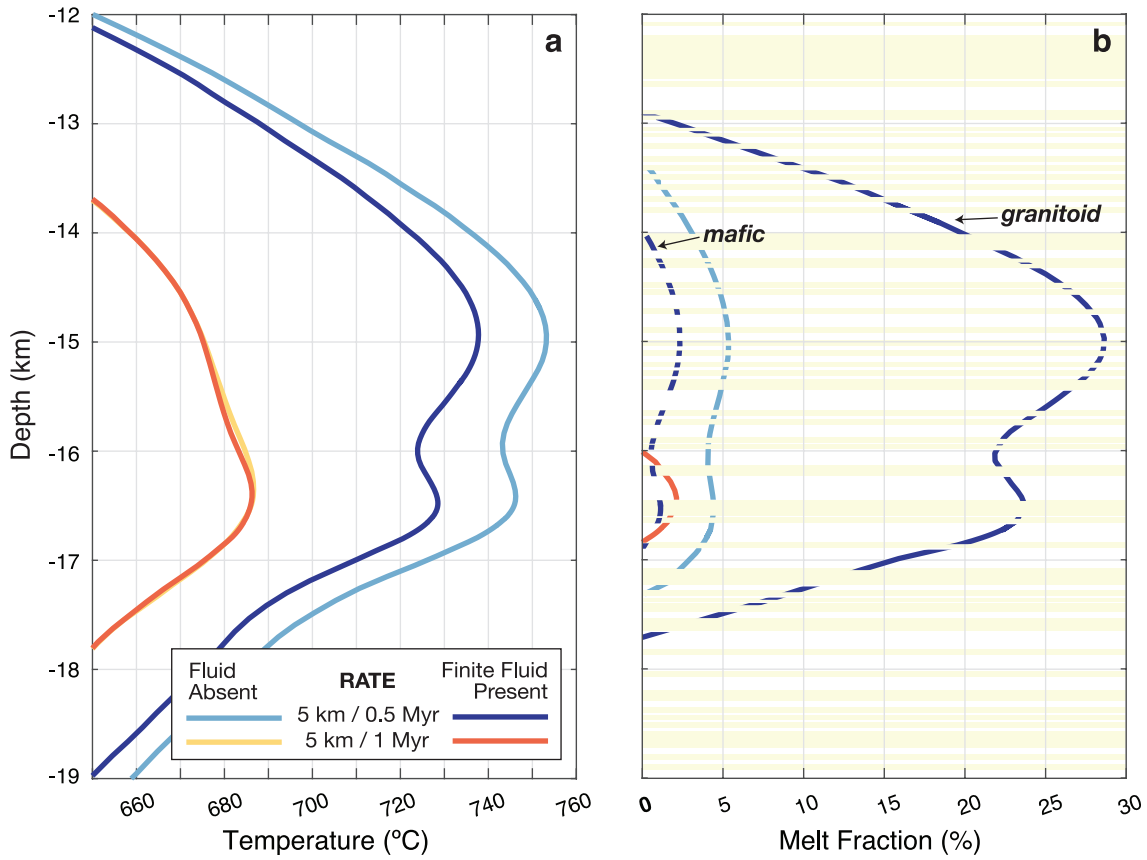

Figure 2-5. (a) A comparison of thermal profiles for two different emplacement rates: 5 km in 1 Myr (red/yellow) and 0.5 Myr (blues) for fluid-absent (light blue/yellow) and fluid-present conditions (dark blue/red). The results show the higher temperatures that result at higher emplacement rates, and that fluid-absent vs. fluid-present F-T curves (0.3 GPa, Figure 2-2) exert an influence. (b) Melt fraction profiles for the thermal profiles shown in (a). When melt fractions are low, there is little effect on thermal profiles. When melt fractions are high (dark blue vs. light blue), there is marked cooling (≤20 degrees) of the thermal profile due to the effect of latent heat of melting for different melt fractions (≤5 vs. 25 %). See text for more details.

Sill-Scale Thermal Evolution

To evaluate the thermal evolution of the basaltic sills and adjacent wall rocks at high spatial (1-50 m) and temporal (10-100's of years) resolution, simulations were run using the same sill-emplacement history shown in Figure 2b and each of the melt fraction-temperature (F-T) curve cases introduced previously (Figure 2-1). The objective was to evaluate changes in the temperature and melt fraction of the adjacent wall rock within 50 m of the basaltic sill margin and during the first few hundred years after the sill is emplaced. In all simulations, the emplacement rate is 50 m/10 kyr. The following key factors were varied: (1) ambient

temperature of the wall rock immediately prior to each sill emplacement, which increases on average as the simulation progresses (Figure A-7), (2) wall rock lithology (granitoid vs. solidified mafic sill), which becomes increasingly variable due to the random emplacement scheme (Figure 2-6), (3) fluid-absent vs. finite fluid-present F-T curves, (4) sill thickness, and (5) the distribution of latent heat in basaltic sills across the liquidus-solidus interval.

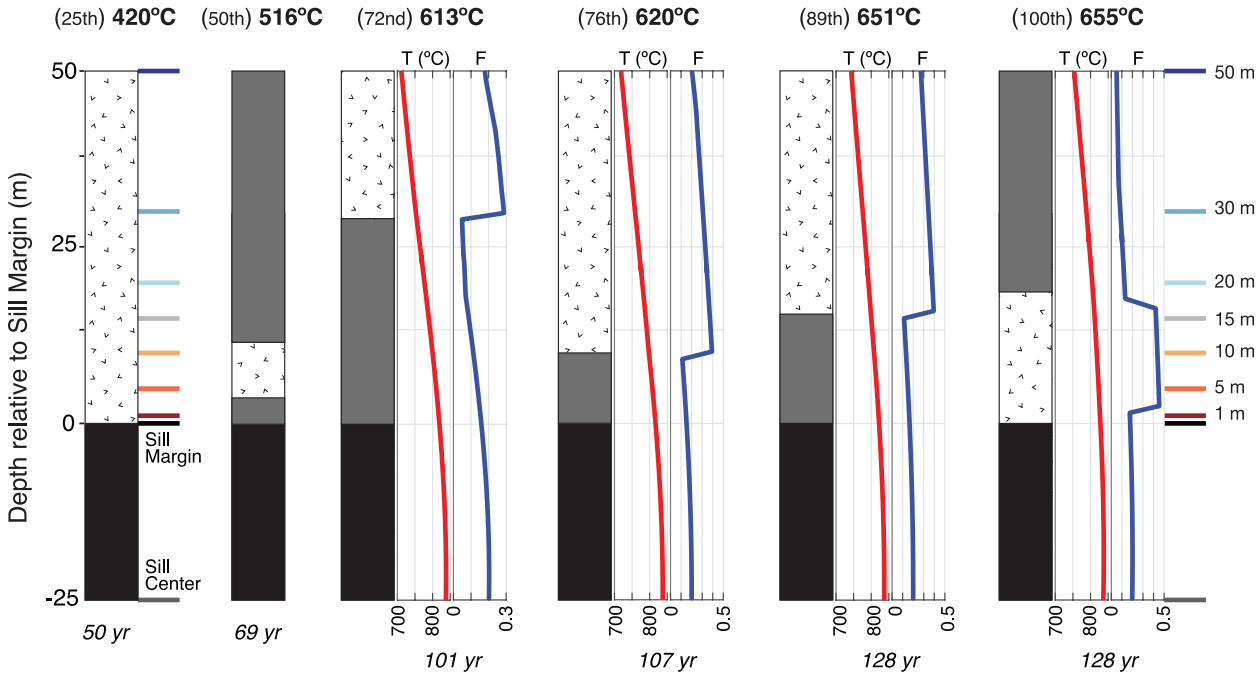

Figure 2-6. Examples of resultant lithologic column 0-50 m above newly emplaced basaltic sills at different stages of random-depth basalt emplacement (50 m sills every 10 kyr) for initial depth interval 10-15 km. Color-coded bars denote distance above sill margin (similar to those in Figures 7-10). Black is newly emplaced basalt, and gray is old mafic sill. Bolded temperature above each column marks the ambient crustal temperature at the time/depth of Xth sill emplacement (shown in adjacent parenthesis). The number at the base of the column marks the time that basalt sill center reaches 80% crystals, at which point exsolution of H2O fluid is underway. Red and blue curves mark the thermal and melt-fraction profiles (0.5 GPa; Figure 1c) along the first 50 m of wall rock adjacent to newly emplaced sills at the time indicated at the base of each column.

Temperature Changes within 100's of Years of Sill Emplacement

Heating of Adjacent 50 m of Wall Rock

After each 50-m basalt sill is emplaced, the ambient temperature of the crustal column steadily increases (Figure 2-2). Therefore, the temperature of the adjacent wall rock at the time of each sill emplacement varies with time (and location within the crustal column). In Figures 2-

7 and 2-8, four different cases of temperature vs. time for the newly emplaced sill and the adjacent 50 m of wall rock above the sill are shown (cfs. Figures A-8 & A-9, for temperature vs. time plots at 0.3 GPa). Ambient temperature refers to the temperature of the wall rock immediately prior to sill emplacement. Each column of sub-figures in Figure 2-7 refers to a different wall-rock lithology (Figure 2-6), which becomes more variable as sill emplacement progresses. The two rows in Figures 2-7 and 2-8 compare fluid-absent and finite fluid-present F-T curves (Figure 2-1) for the adjacent wall rock. The ambient temperature at the time each basaltic sill was emplaced is also noted, and there is some minor variation between fluid-absent and finite fluid-present scenarios.

In all cases (Figure 2-7), within the first 50 years of sill emplacement, there is an abrupt jump in temperature within the adjacent wall rock. When the ambient temperature is ~420°C, temperatures reach ≥700°C for 50 yrs within 15 m of adjacent wall rock. When the ambient temperature is ~516°C, temperatures are ≥700°C for 150 yrs within 20 m of adjacent wall rock. When the ambient temperature is ~611°C, temperatures reach ≥700°C for 500 years (and are ≥680°C for 900 years) within 50 m of the sill margin. When the ambient temperature is ~657°C (Figure 2-8), temperatures are ≥700°C for >1500 years (and are ≥680ºC for 3 kyr) within 50 m of the adjacent wall rock.

Not surprisingly, the most important control on how high temperatures are reached in the wall rock adjacent to a newly emplaced sill, and for how long, is the ambient temperature. The effect of different wall rock lithologies on the thermal profile is minimal. The temperature profiles are slightly cooler when finite fluid-present vs. fluid-absent F-T curves are employed, owing to the effect of latent heat of fusion during partial melting of wall rock.

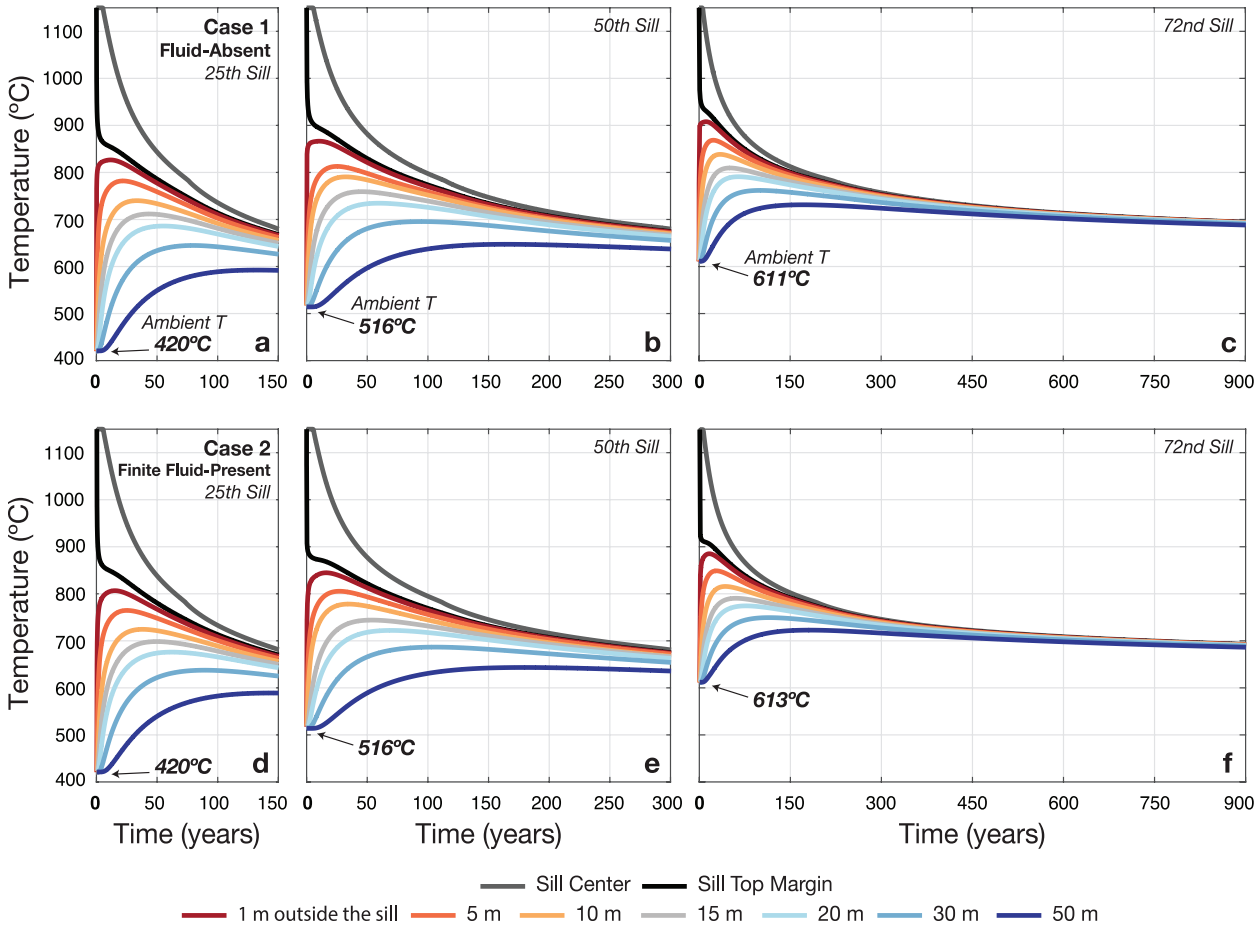

Figure 2-7. Temperature vs. time immediately after sill emplacement at the basaltic sill center (gray line), basaltic sill top margin (black line), and depths 1, 5, 10, 15, 20, 30, and 50 m above the sill margin (colored lines same as in Figure 2-6). All cases show random emplacement of 50 m thick sill every 10 kyr into an initial depth range of 10-15 km. (a) the 25th sill, (b) the 50th sill, and the (c) the 72nd sill; all for fluid-absent F-T curves at 0.5 GPa (Figure 2-1b). (d-f) same as (a-c), except all for finite fluid-present F-T curves at 0.5 GPa (Figure 1c). Bolded temperature with arrow is the ambient temperature of the crust immediately prior to sill emplacement.

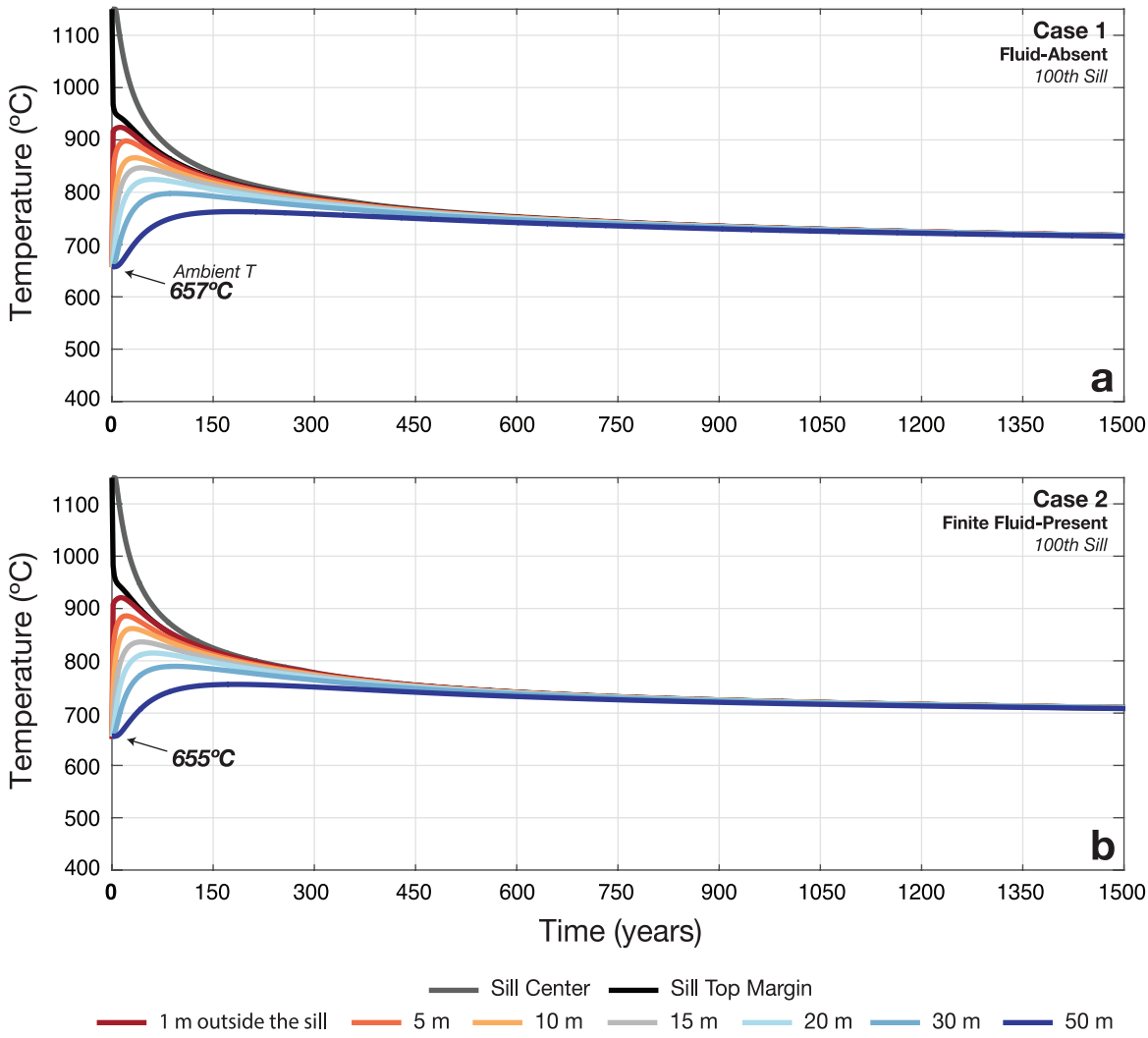

Figure 2-8. (a) Same as Figure 2-7 (a), but for the 100th sill; fluid-absent F-T curve. (b) Same as Figure 2-7 (d), but for the 100th sill; finite fluid-present F-T curve at 0.5 GPa. Bolded temperature with arrow is the ambient temperature of the crust immediately prior to sill emplacement.

Cooling of Basaltic Sills

As ambient temperatures increase at the time of sill emplacement, the time it takes for a basaltic sill to cool to its solidus (~680°C at 0.5 GPa; Figure 2-1a) also increases (Figure 2-7). When the ambient temperature is ~420 vs. 516°C, the basaltic sill center cools to 680°C within ~150 vs. ~300 years. When the ambient temperature is ~611 vs. 657°C (Figure 2-7 and 2-8), it takes more than 900 vs. 1500 years for the sill center to reach its solidus respectively.

Melt Fraction Changes Within 100's of Years of Sill Emplacement

Adjacent 50 m of Wall Rock

Melt fractions are calculated during each simulation alongside temperature, based on the various F-T curve relationships (Figure 2-1), within each wall rock lithology (granitoid vs. mafic sill). The amount of water that is present (i.e., fluid-absent vs. finite fluid-present conditions) plays a primary role in the extent of wall rock partial melting. Plots of melt fraction vs. time since sill emplacement are shown in Figures 2-9 and 2-10 (cf., Figures A-10-11, for melt fraction vs. time plots at 0.3 GPa). Each column of sub-figures in Figures 2-9 and 2-10 refers to a different ambient temperature and wall-rock lithology (Figure 2-6), whereas the two rows compare fluid-absent and finite fluid-present F-T curves for the adjacent wall rock (Figure 2-1).

In all cases (Figure 2-9 and 2-10), within the first 50 years of sill emplacement, there is an abrupt jump in melt fraction within the adjacent wall rock. For the case of the 25th sill emplacement, the ambient temperature is ~420°C and the adjacent 50 m of wall rock is all granitoid. In this case, the degree of melting in the adjacent wall rock (≤20% and ≤40%, respectively) is most strongly controlled by fluid-absent vs. finite fluid-present conditions (Figure 2-9a and 2-9d). In the case of the 50th versus 72nd sill emplacements, an additional control on the degree of melting is the lithology of the wall rock adjacent to each newly emplaced sill. For example, owing to the random emplacement of basaltic sills, by chance the wall rock immediately above the 50th sill is predominantly mafic sill, with a small lens of granitoid 4-11 m above the sill margin, whereas the wall rock above the 72nd sill is mafic sill from 0-29 m and then granitoid (Figure 2-6). The higher melt fractions when the ambient temperature is lower (i.e., 516 vs. 611 °C) are due to the presence of granitoid within 10 m of the 50th sill's margin, and its absence within the first 29 m of the 72nd sill. As expected, melt

fractions are higher for finite fluid-present (≤40% melt) vs. fluid-absent (≤18% melt) conditions in all cases.

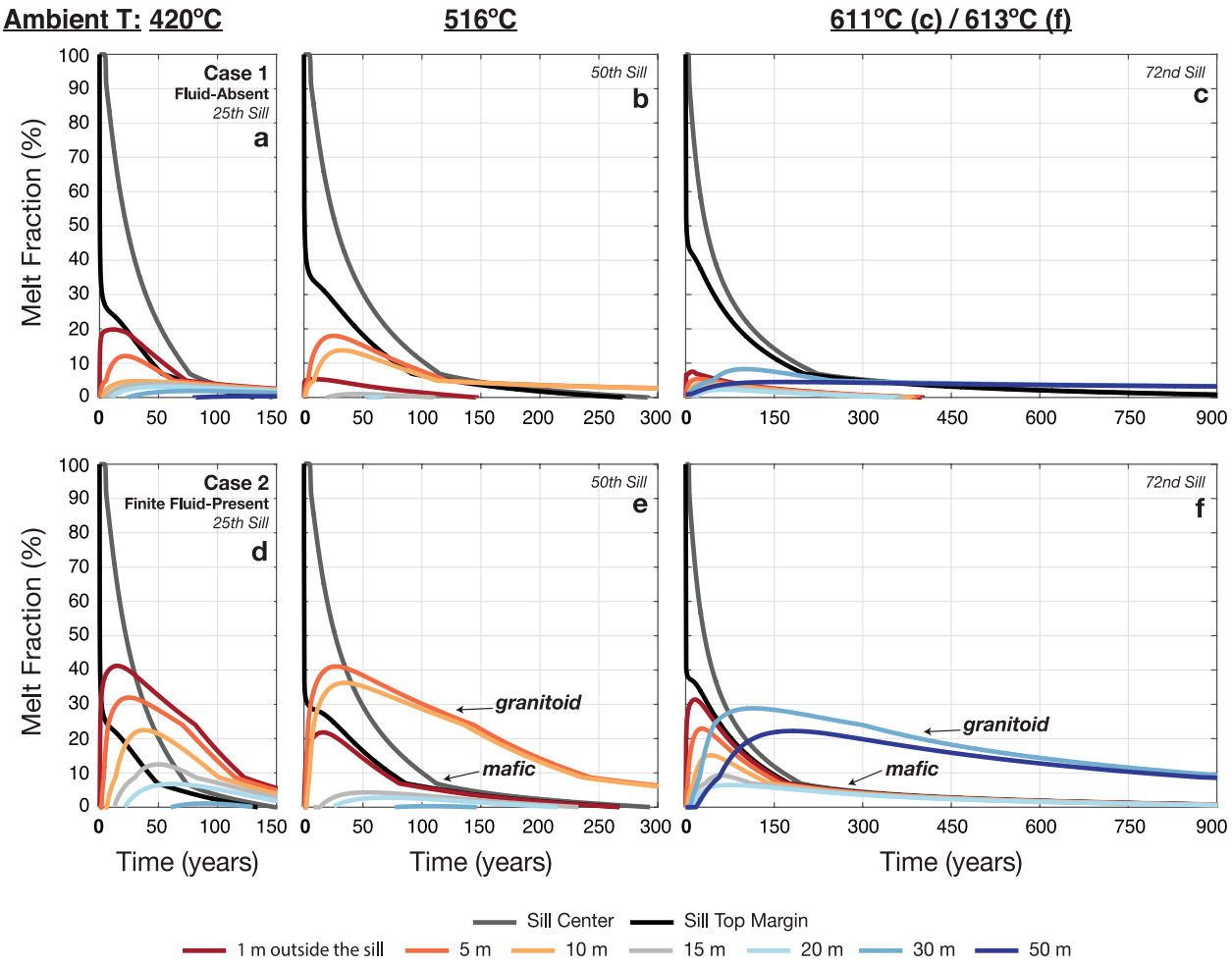

Figure 2-9. Same as Figure 2-7, but melt fraction instead of temperature is shown versus time immediately after sill emplacement. All symbols and colors are the same as in Figure 2-7. Arrows (in e-f) point to the different lithology (granitoid vs. mafic sill) of the wall rock (see Figure 6).

In Figure 2-10, the melt fractions in the 50 m above the 100th sill, where the ambient temperature at the time of sill emplacement was ~657°C, are shown for fluid-absent versus finite fluid-present conditions. In this case, the wall rock immediately above the sill is granitoid (0-19 m) and then solidified mafic sill (Figure 2-6). Under finite fluid-present conditions, the granitoid reaches 45-60% melt fraction and remains above 30% melt fraction for ~400 years, whereas the mafic sill reaches ≤12% melt and remains above 5% melt for ~400 years. The temperature and

melt fraction profile through the wall rock 50-m column is summarized in Figure 6 for various sill emplacements (at the point in time when the basaltic sill center has reached 80% crystallization).

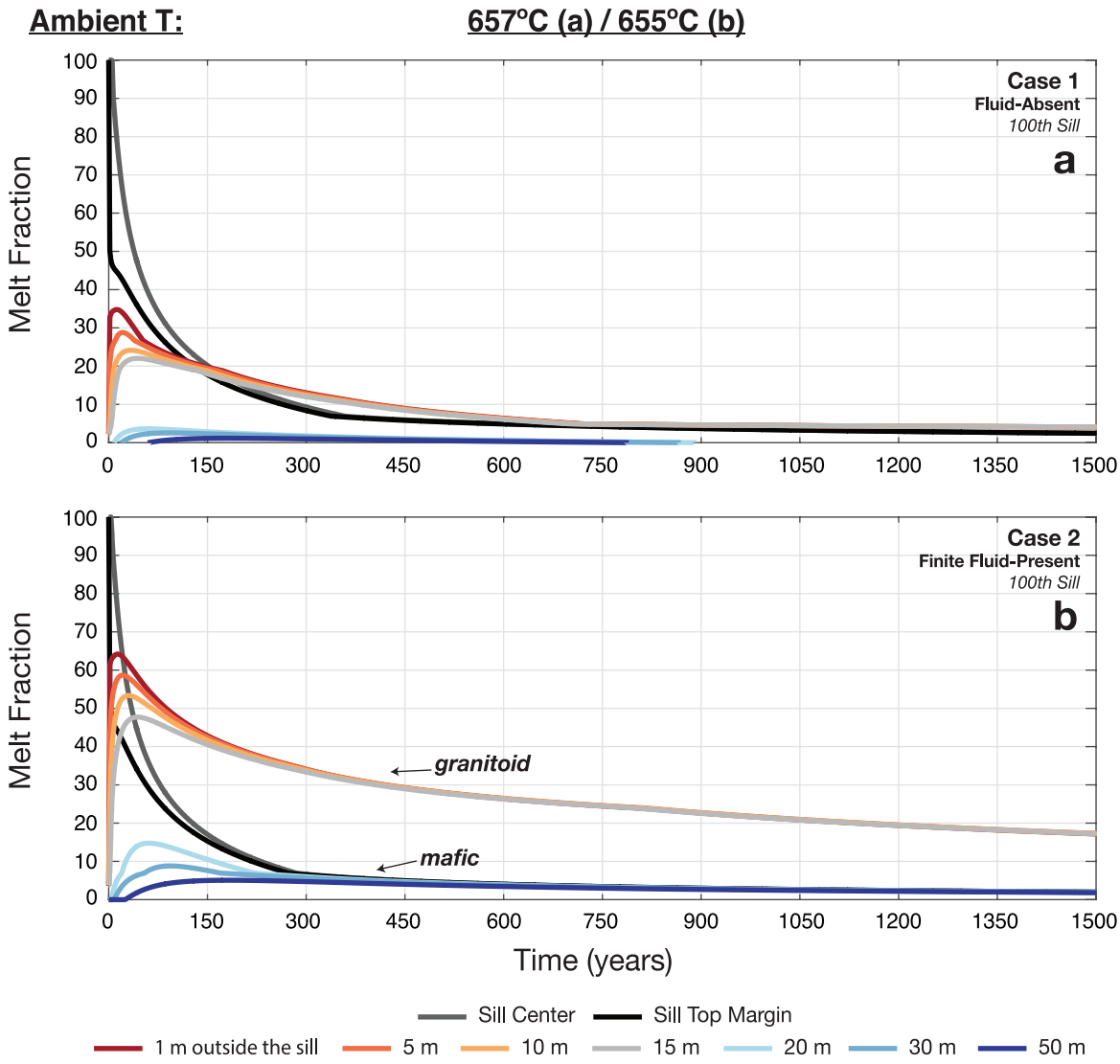

Figure 2-2-10. Same as Figure 2-8, but melt fraction instead of temperature is shown versus time immediately after sill emplacement. All symbols and colors are the same as in Figure 2-7. Arrows (in b) point to the different lithology (granitoid vs. mafic sill) of the wall rock (see Figure 2-6).

Crystallization of basaltic sills

As ambient temperatures increase at the time of sill emplacement, the time it takes for the center of the basaltic sills to crystallize to 20% melt fraction also increases (Figure A-7). It is at this stage of crystallization that the exsolution (and loss) of an H_2O-rich fluid phase from the

basaltic sill begins, as discussed below. When the ambient temperature is 420 vs. 516°C, the basaltic sill center is 80% crystallized within ~50 vs. ~69 years. When the ambient temperature is 611 and 657°C (Figure 2-9 and 2-10), it takes ~101 and ~128 years, respectively, for the sill center to reach 80% crystallization.

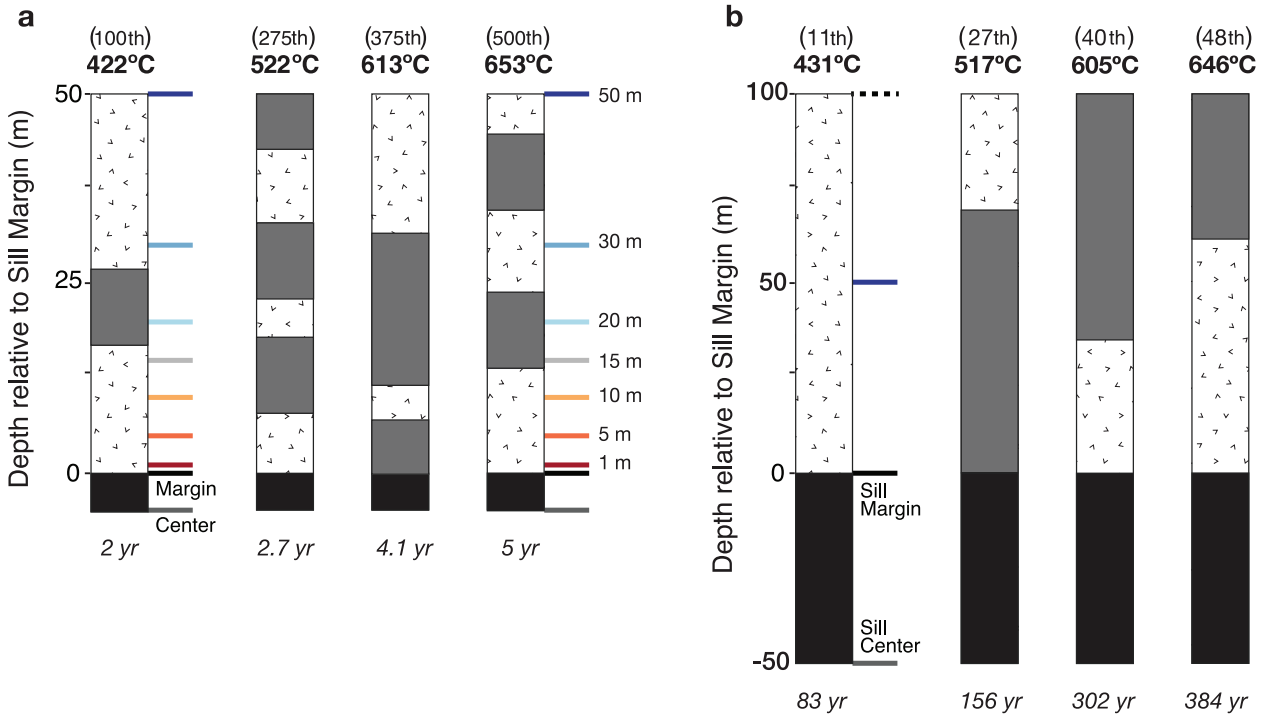

Figure 2-11. Examples of a resultant lithologic column (a) 0-50 m above newly emplaced 10-m thick basaltic sills (10 m/2 kyr) and (b) 0-100 m above newly emplaced 100-m thick basaltic sills (100 m/20 kyr) at different stages of emplacement. The initial depth interval is 10-15 km in both cases. Color-coded bars denote distance above sill margin (similar to that in Figure 2-6). Black is newly emplaced basalt, and gray is old mafic sill. Bolded temperature above each column marks the ambient crustal temperature at the time/depth of Xth sill emplacement (shown in adjacent parenthesis). The number at the base of the column marks the time that basalt sill reaches 80% crystals, at which point exsolution of H2O fluid is underway. Sill scale results for (a) are shown in Figures 2-12, A-12, A-13, and A-16. Sill scale results for (b) are shown in Figures 2-13, A-14, A-15 and A-17.

Effect of Variable Thickness of Basaltic Sills

There are two causes for why varying the thickness of newly-emplaced basaltic sills (e.g., 10, 50 and 100 m) controls the degree of partial melting that develops in the adjacent wall rock for any specified ambient crustal temperature. The first cause is the markedly different crustal lithologies (i.e., distribution of mafic sills within granitoid) that develop, dependent on whether

sill thicknesses are 50 m (Figure 2-6) or alternatively either 10 or 100 m (Figure 2-11). Because mafic sills and granitoid have distinctly different F-T curves, resulting melt fractions will vary. The second reason is that sill thickness strongly controls the temperature evolution in the surrounding wall rock (e.g., Furlong et al., 1991; Annen, 2017). Variations in the thermal profile of the adjacent wall rock at provided in Appendix A (cf. Figures A-12-15). Of relevance to this study is the impact of varying sill thickness on the extent of partial melting that occurs along wall-rock margins.

In the case of a 10-m thick sill emplaced into the crust at ~613°C (Figure 2-12f), <10% melt fraction will form in granitoid wall rock (finite fluid-present) for ≤5 years within 10 m of the sill margin. In contrast, under similar conditions (ambient temperature and finite fluid-present) a newly-emplaced 100-m thick sill causes ≥30% partial melting in granitoid wall rock for ~800 years up to 30 m distant from the sill margin (Figure 2-13f). Moreover, when the ambient temperature is as low as ~431°C, the emplacement of a 100-m thick sill induces significant partial melting (≥20%) of granitoid (finite fluid-present conditions) for ≤300 years within 20 m from the sill margin (Figure 2-13d). Importantly, the results in Figure 2-12 (10-m sills) and Figure 2-13 (100-m sills) are both markedly different from those obtained under similar conditions for 50-m thick basaltic sills (Figure 2-10). (See Figures A-16 and A-17, for melt fraction results for 10- and 100-m thick sills when ambient temperature is ~650°C.) The key observation is that variations in the thickness of newly-emplaced sills (10, 50, 100 m) lead to significant differences in the degree and duration of wall-rock partial melting.

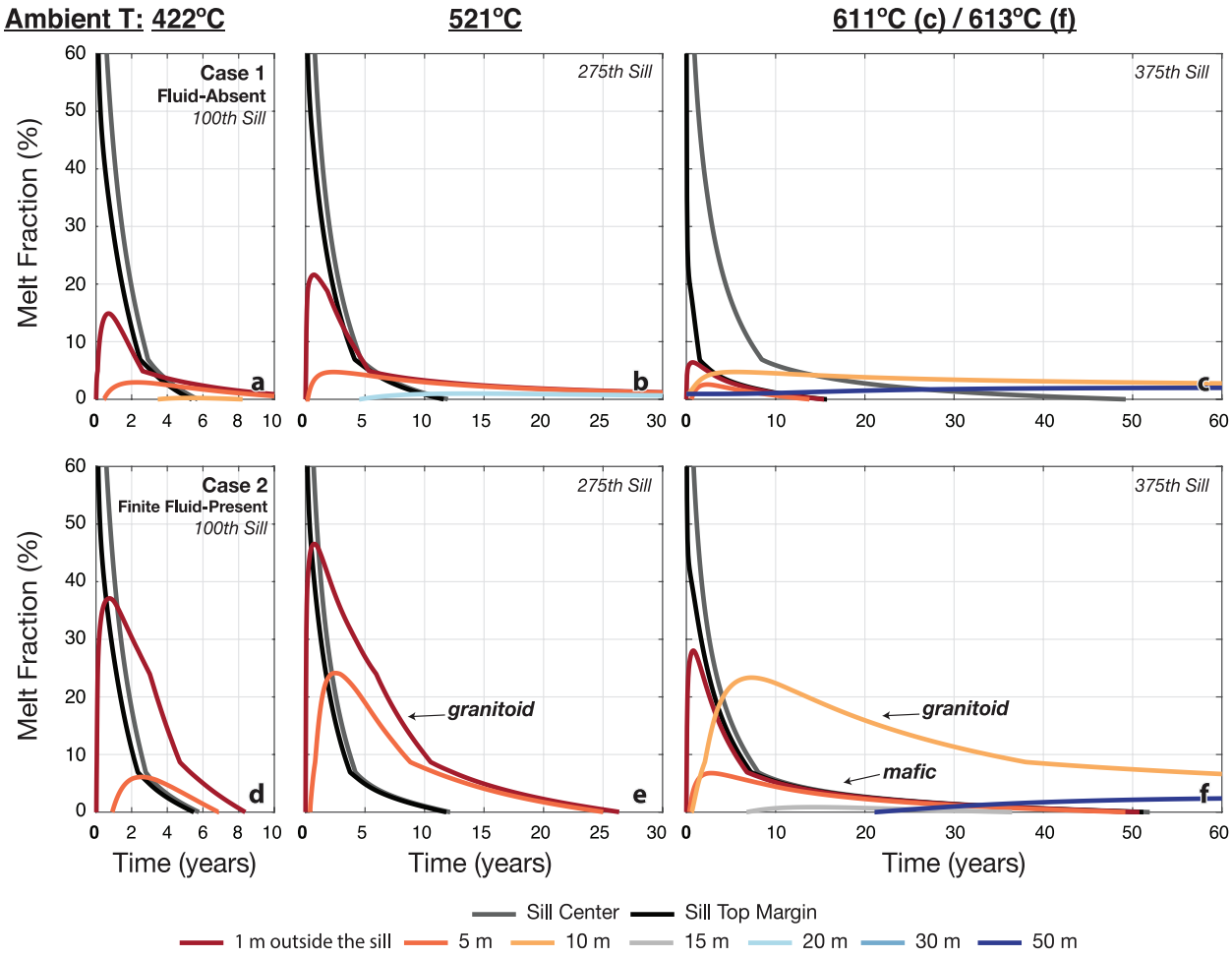

Figure c2-12. Melt fraction vs. time immediately after 10-m thick sill emplacement at the basaltic sill center (gray line), basaltic sill top margin (black line), and depths 1, 5, 10, 15, 20, 30, and 50 m above the sill margin (colored lines the same as in Figure 2-11). All cases are random emplacement of 10-m thick sill every 2 kyr into an initial depth range of 10-15 km. (a) the 100th sill, (b) the 275th sill, and (c) the 375th sill from a single simulation realization; all for fluid-absent F-T curves at 0.5 GPa (Figure 2-1b). (d-f) same as (a-c), except for finite fluid-present F-T curves at 0.5 GPa (Figure 2-1c). Arrows (in e-f) point to different lithology (granitoid vs. mafic sill) of the wall rock (see Figure 2-11).

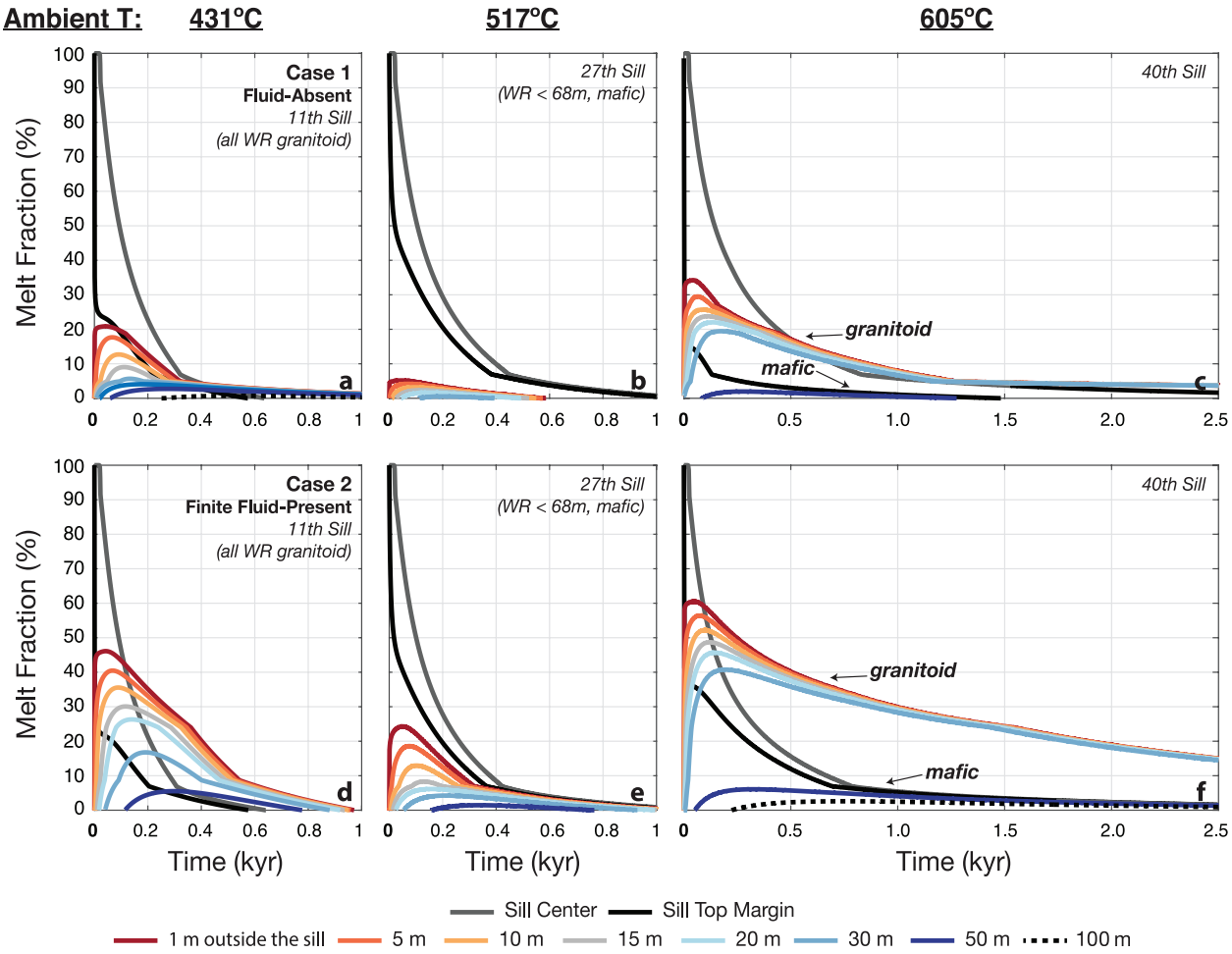

Figure 2-2-13. Melt fraction vs. time immediately after 100-m sill emplacement at the basaltic sill center (gray line), basaltic sill top margin (black line), and depths 1, 5, 10, 15, 20, 30, 50, and 100 m above the sill margin (colored lines the same as in Figure 2-11). All cases are random emplacement of 100-m thick sill every 20 kyr into an initial depth range of 10-15 km. (a) the 11th sill, (b) the 27th sill, and (c) the 40th sill from a single simulation; all for fluid-absent F-T curves at 0.5 GPa (Figure 2-1b). (d-f) same as (a-c), except for finite fluid-present F-T curves at 0.5 GPa (Figure 2-1c). Arrows (in c and f) point to different lithology (granitoid vs. mafic sill) of the wall rock (see Figure 2-11).

Effect of a Variable Distribution of Latent Heat across the Liquidus-Solidus Interval

An additional factor that may affect the cooling history of a basaltic sill and the transient heating of the adjacent wall rock is a non-linear distribution of latent heat across the liquidus-solidus interval. For the cases shown in Figures 7-10, latent heat is distributed linearly. In the two alternative cases (Figure A-4), where (1) 75% of the latent heat is released in the first 25% of crystallization and (2) 75% of the latent heat is released in the last 25% of crystallization, the time it takes the 100th basaltic sill to cool to 810°C (~80% crystallization at 0.3 GPa; Figure 1a),

is ~6 years longer and ~29 years shorter, respectively, compared to the ~120 years it takes for a linear distribution of latent heat (cf. Figure A-4c). Similarly, the time interval over which the adjacent wall rock, 10 m from sill margin, remains ≥740°C (≥30% melt fraction; finite fluid-present conditions, Figure 2-1c), is ~9 years longer and ~37 years shorter, respectively for case 1 and case 2 (cf. Figure A-4a).

The most important parameter to track is the difference in time between the duration of wall rock heating (e.g., 10 m above sill ≥ 740°C) and the time it takes the basaltic sill to crystallize to 80% (i.e,. to 810°C; Figure 2-1a), which marks the onset of fluid exsolution. For a linear distribution of latent heat, this time interval for the 100th sill (Figure 6) is 275 years, whereas for case 1 and case 2 (cf. Figure A-4a), the time interval is 3 years longer and 8 years shorter, respectively. Therefore, a non-linear distribution of latent heat has little effect on the relative time scale between the cooling of a basaltic sill and the transient heating of the adjacent wall rock.

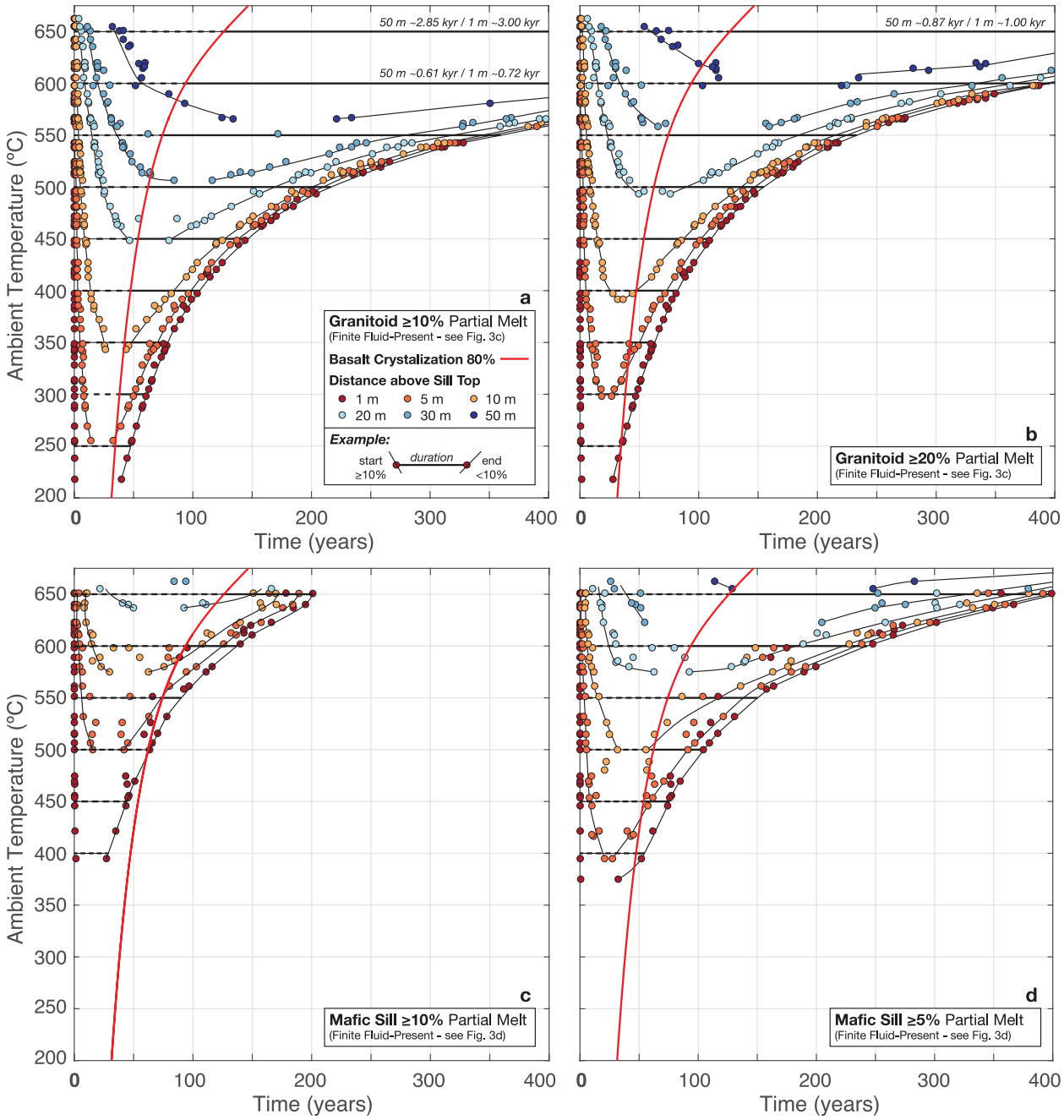

Figure 2-14. (a) Plot of ambient temperature versus time with superimposed isopleths of fluid-present granodiorite at fixed distances above the basaltic sill margin (color-coded; see legend) that contain ≥10% melt fraction at 0.5 GPa. Red line is the time it takes a newly emplaced basaltic sill to crystallize 80% (onset of fluid exsolution; Figure A-7). Bold isothermal lines denote time interval, for a specific initial ambient temperature, over which granitoid wall rock is under finite fluid-present conditions and thus contains ≥10% melt fraction. (b) Same as (a), but for granitoid with ≥20% melt fraction. (c) Same as (a), but for solidified mafic sills with ≥10% melt fraction. (d) Same as (a), but for solidified mafic sills with ≥5% melt fraction. Isopleth curves that connect the color-coded dots are hand drawn.

Transfer of Water from Basaltic Sills to Partial Melt of Adjacent Wall Rock

A final process we explore is the transfer of dissolved water from the basaltic sills into partial melts of the adjacent wall rock, and what conditions are required for this to occur. For example, the solubility limit for dissolved water in the melt is ~10 wt% in a basalt that is emplaced at a depth with an ambient pressure of 0.5 GPa (e.g., Behrens et al., 2001; Zhang et al., 2007). If the initial water content is ~3 wt% (Gazel et al., 2012), 10 wt% H_2O will be reached in the melt during late-stage crystallization. Therefore, exsolution of an H_2O-rich fluid phase is expected to occur by the time the sill center reaches 80% crystallization. Based on results from Bachmann and Bergantz (2006), migration of an exsolved fluid phase (via "gas sparging") through partially molten sill and wall rock is expected, and transport distances of 5-10 m are plausible in ~5-40 years. The question is whether the time duration for partial melting in the adjacent wall rock (e.g. Figure 2-14) matches the time scale required for the basaltic sill to crystallize ~80%, enabling transfer of a fluid phase to the adjacent wall rock.

In Figure 2-14a and b, the time it takes (relative to the instant of sill emplacement) for granitoid wall rock at specified distances (1, 5, 10, 20, 30, and 50 m) above the sill margin to reach a certain temperature, and thus melt fraction (finite fluid-present conditions), is shown. Superimposed on these plots are isopleths of melt fraction (10 and 20%) at each depth, based only upon the sill emplacements where all of the material up to that depth was granitoid. The valley shaped pattern for an isopleth of melt fraction in the wall rock, at a given distance from the sill margin, illustrates the initial, transient heating of the wall rock (i.e., at a given location relative to the sill margin, the 10% melt fraction moves downward as a function of ambient temperature), followed by the subsequent cooling of the wall rock (at a given location relative to the sill margin, the 10% melt fraction moves upward as a function of ambient temperature). Pairs

of same-colored points at the same ambient temperature denote the times after a given sill emplacement in which the wall rock partially melts above or solidifies below a certain melt fraction, where dot color corresponds to the distance from the sill margin. Spacing between those pairs of points is the time interval in which the wall rock at that distance from the sill has melt fraction above the indicated level. Also shown in this plot is a solid red curve that marks the time at which the center of a recently emplaced basaltic sill reaches 80% crystallization (Figure A-7b), and therefore exsolution of an H_2O-rich fluid phase. Tie lines located to the right of this curve mark the time interval where fluid-present conditions in granitoid wall rock are most likely to exist, owing to transfer of an exsolved H_2O-rich fluid. Therefore, the relevant melt fraction curves for both types of wall rock, granitoid and solidified mafic sills, are those for finite fluid-present conditions, which are also used for the melt fractions illustrated in Figure 2-6.

In Figure 2-14c and d, a similar pair of plots is shown, but in these two cases, the wall rock is solidified mafic sills and the isopleths are for 5 and 10% melt fractions (calculated for finite fluid-present conditions; Figure 2-1c) at each of the depths considered. The isopleths are based only upon the sill emplacements where all of the wall rock up to that depth was solidified mafic sill. The more refractory nature (i.e. lower melt fraction at a given T and H_2O content) of the mafic sills relative to granitoid is illustrated in Figure 2-14a-d. Melt fractions of ~5-10% do not develop under finite fluid-present conditions until ambient temperatures are ≥500°C and only within 1-5 m of the newly emplaced sill margin. In sharp contrast, melt fractions in finite fluid-present granitoid up to 20 m from the sill margin exceed 20%, for ~20 years and 10% for ~100 years. Despite the relatively refractory nature of the solidified mafic sills, their close spatial proximity to granitoid increases the chance that small degree partial melts from the mafic sills will develop hydraulic connectivity with the larger degree partial melts from the granitoid,

leading to interaction and mixing of compositionally distinct partial melts derived from two very different source rocks.

The efficient transfer of H_2O fluid from a crystallizing sill to the wall rock is more clearly demonstrated when the loss (i.e., advection) of H_2O fluid, and thus heat, from the hydrous basalt during late-stage crystallization is accounted for. For example, the loss of ~2 wt% H_2O fluid, with a heat content of ~3000 J/g at 700°C and 0.5 GPa (Burnham et al., 1969) out of a basaltic sill (>80% crystallized; Cp = ~1.4 J/g/K; Table 2-1) will lead to ~43°C of cooling. Moreover, the addition of this H_2O fluid into 50 m of wall rock will similarly induce another ~43°C of heating, and thus prolong the duration of the transient wall rock heating.

The conclusion, therefore, is that finite fluid-present F-T curves are relevant for granitoid and mafic sill lithologies in wall rock adjacent to newly emplaced sills. Once the ambient temperature is ~600°C, significant melt fractions develop that contain dissolved H_2O (Figure 2-6), but at levels below solubility limits owing to the limited amount of H_2O available from the basaltic sill. The formation of hydrous partial melts that are fluid undersaturated has implications for their rapid segregation and transport as discussed below.

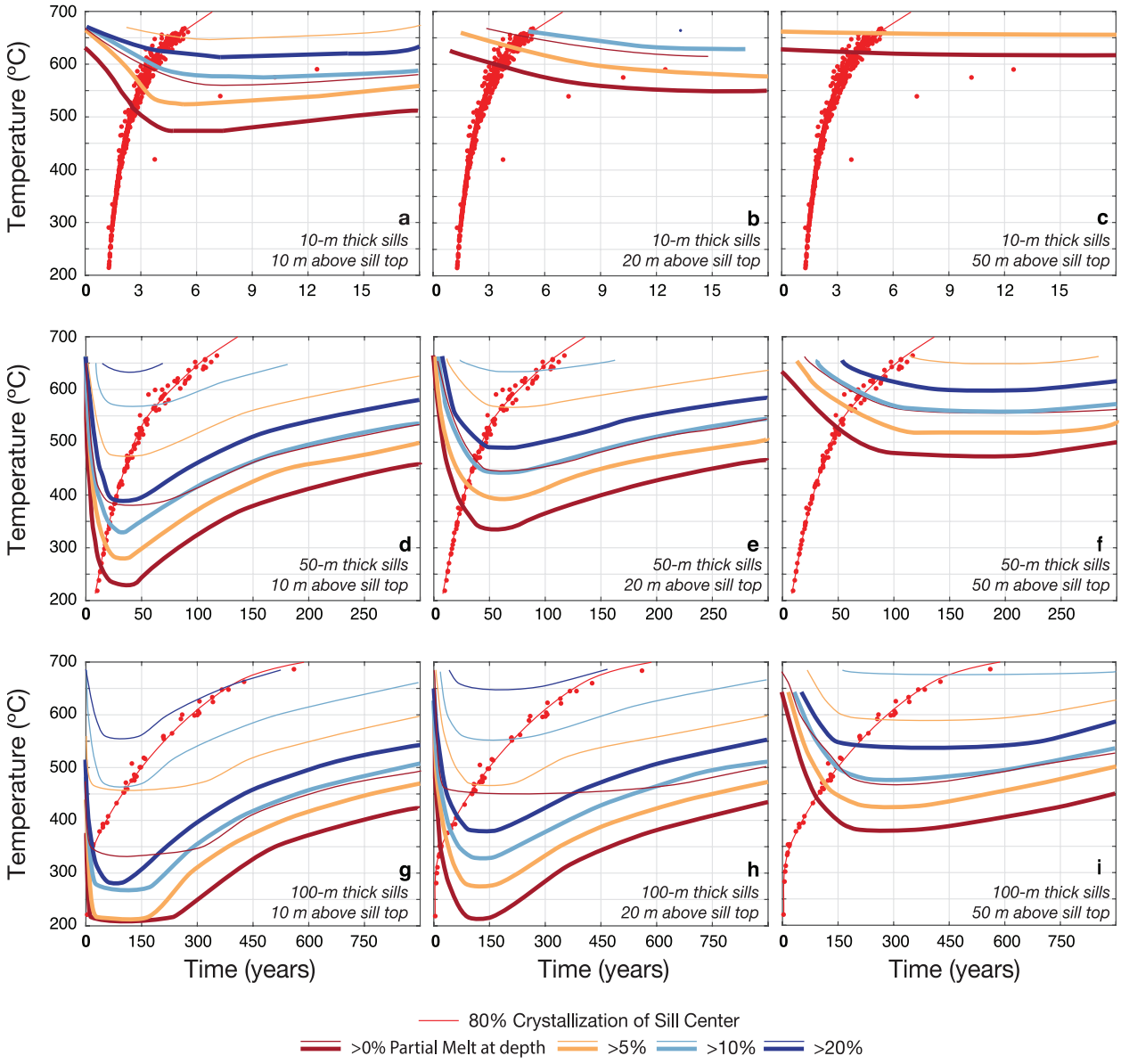

Figure 2-15. Plots of ambient temperature versus time with superimposed isopleths of finite fluid-present granodiorite (bold) and mafic sill (thin) partial melting windows. (a-c) Results for 10-m thick sills at 10, 20 and 50 m above the sill margin. (d-f) Results for 50-m thick sills at 10, 20 and 50 m above the sill margin. (g-i) Results for 100-m thick sills at 10, 20 and 50 m above the sill margin.

The Role of Variable Sill Thickness

Figure 2-15 presents a similar set of plots as shown in Figure 2-14, but in this case the effect of varying sill thickness (10, 50 and 100 m) is featured. The comparative results clearly illustrate that partial melting along the wall-rock margins of newly-emplaced sills is far more extensive for thicker (100-m) versus thinner (10-m) sills. In the case of 10-m thick sills, very

limited and transient (<20 years) partial melts form in the wall-rock margin above newly-emplaced sills, even when ambient temperatures are relatively high (≥ 600 °C). In contrast, in the case of 100-m thick sills, extensive (>20%) and long-lived (>300 years) melt fractions develop along a new sill margin, even when ambient temperatures are relatively low (~400 °C). These results underscore the role of variable sill thickness is controlling the extent and duration of partial melting along the wall-rock margins of a newly-emplaced sill, as well as the ambient temperature at which significant wall-rock partial melting can occur.

Discussion

Development of Crustal-Scale Thermal Profiles and Mixed Lithologies

Several factors influence, to varying degrees, the temperature-depth profile through the crustal column due to the influx of basaltic sills. Among the parameters explored in this study, three exert the strongest control: (1) random vs. fixed emplacement of sills, (2) the initial depth range of sill emplacement, and (3) the time interval over which a thickness of basalt is emplaced. These results are broadly consistent with previous work in the literature (e.g., Dufek and Bergantz, 2005; Annen et al., 2006; Leeman et al., 2008; Karakas and Dufek, 2015; Colón et al., 2018). An important factor additionally explored in this study is the development of a mixed crustal lithology as the crust is gradually heated through the periodic and random emplacement of basaltic sills. Once temperatures reach values that facilitate partial melting of wall rock, both the original granitoid as well as previously solidified mafic sills are eligible source rocks, leading to two sets of compositionally-distinct partial melts. Therefore, tracking the development of the mixed crustal lithology is as important as tracing the evolving thermal profile through the crust.

The results from this study show that crustal temperatures in the middle-upper crust can reach >600°C with varying proportions of mafic sills embedded within the granitoid crust, dependent on the rate of basalt emplacement, as well as the depth interval over which basalts are initially emplaced. For example, the higher the rate of emplacement, the less basalt is required to heat the crust to >600°C (Figure 2-4b) and thus the lower the ratio of solidified mafic sills to granitoid in the crustal column. Similarly, the deeper and broader the initial depth interval of basalt emplacement, a lower basalt:granitoid ratio is required to heat the crust >600°C (Figure A-6).

Importance of Hydrous Partial Melts of Wall Rock and their Transport

An additional factor of potential relevance to crustal-scale thermal profiles is the formation, and then advection, of partial melts along the wall-rock margins of newly emplaced sills. The high spatial and temporal resolution of our numerical model reveals the thermal consequences in adjacent wall rock in response to subsequent injections of 50-m thick basaltic sills once ambient crustal temperatures reach ~600°C. After a new sill is emplaced, temperatures in the adjacent wall rock will reach ≥700°C for ≥500 years within 50 m of the sill margin. It is further shown that basaltic sills with an initial H_2O content of 3 wt% will undergo 80% crystallization at the sill center within 100 years when the ambient temperature of the surrounding crust is ~600°C. After this much crystallization, the basaltic sill is expected to exsolve an H_2O-rich fluid phase, leading to finite fluid-present conditions for the adjacent wall rock at its solidus. Resulting melt fractions in granitoid and mafic-sill wall rock will reach ≥20% and ≥5%, respectively, within 30 and 20 m of the sill margin for ~300 and ~150 years, respectively. Given the close spatial association of mafic sills and granitoid in the crustal column

(Figure 6), it is expected that the relatively low-degree (~5%) partial melts from the mafic sills will interact with relatively high-degree (~20%) partial melts from the granitoid wall rock.

Once ambient crustal temperatures reach ~650°C, any subsequent emplacement of a 50 m sill will induce substantial partial melting of the adjacent wall rock (Figures 2-6 and 2-14). At relatively high melt fractions, the partial melts will be hydrous, but are expected to be fluid undersaturated owing to the limited amount of water available from the basaltic sills. Under these conditions, a large volume increase is created during partial melting. At 500 MPa, any dissolved water content less than 10 wt% will be fluid under-saturated, and the density of a minimum/eutectic melt partial melt from a granitoid (with ~5-9 wt% dissolved H_2O) will range from ~2360-2290 kg/m^3 (Lange, 1997; Ochs and Lange, 1999), which represents a volume increase of ~11-14%. Experimental studies confirm that partial melting reactions of crustal rocks that produce a positive change in volume lead to micro-cracking and melt-filled fractures (e.g., Connolly et al., 1997; Rushmer, 2001). The formation of near-vertical melt-filled fractures in granitoid wall rock will be further facilitated by the pre-existence of scattered aplite dikes (Lange, 2019), which are ubiquitous in the Sierra Nevada batholith. The near-eutectic bulk composition (high-SiO_2 rhyolite) of aplite dikes ensures extensive melting (limited only by the finite amount of H_2O present), and they are likely sites for melt-filled fractures to readily develop.

The rapid development of melt-filled fractures (through melting of aplite dikes) will facilitate the extraction of partial melt from the wall rock (e.g., Sleep, 1988). Once the melt-filled fractures exceed the critical length of a self-propagating dike, it is possible for segregation to occur through dike transport. The critical length at which a vertically oriented dike of constant volume can "self-propagate" is given by the relation, $K_c/(\Delta\rho g)]^{2/3}$, where K_c is the fracture

toughness (~1 MPa $m^{1/2}$; Gonnermann and Taisne, 2015). For a $\Delta\rho$ (rock-melt) of ~290-360 kg/m^3, critical lengths of ~43-50 m are obtained, which are on the same length scale of the partially melted wall-rock margins. If these partial melts segregate under fluid under-saturated conditions, their liquidus temperatures will decrease during ascent (owing to the positive dT/dP slope of their liquidus), which will prolong their transit through the crust despite conductive loss of heat (Waters and Lange, 2017).

The key point for this study is that rapid segregation and transport of these partial melts out of the wall rock is a viable hypothesis that merits further examination, because it will have major consequences to thermal profiles through the crust. The removal of these partial melts by advection will cool their source regions, and heat shallower levels of the crust where they are emplaced. Moreover, this process of melt advection will also alter the composition of the middle-upper crust.

Compositional Re-Working of Crust Due to Transport of Wall-Rock Partial Melts

Over time, the episodic vertical transport of small volumes of rhyolitic melt (i.e., partial melts of wall rock) into higher levels of the crust will gradually lead to a relatively large accumulation of Plio-Quaternary leucogranite in the upper crust, with a composition that is more evolved than the Mesozoic granodiorite that characterizes most of the exposed granitoid in this region (e.g., Oliver et al., 1993). The rhyolitic partial melts that form along the margins of newly-emplaced basalt sills will be derived from both previously solidified mafic sills and granitoid. Therefore, the two sets of partial melts will be characterized by distinctly different major- and trace-element concentrations, and these two distinctly different partial melts are likely to interact during their segregation and transport, given the close spatial proximity of

solidified mafic sills within granitoid wall rock (Figure 2-6). It is therefore likely that Plio-Quaternary leucogranite bodies of rhyolitic composition (73-75 wt% SiO_2) will form in the upper crust with major-element compositions dominated by the more voluminous partial melts of granitoid, but with concentrations of select trace elements (e.g., Sr) that are predominantly derived from the Sr-rich mafic sills (Cousens, 1996). Subsequent partial melting of these leucogranite bodies will lead to high-SiO_2 (76-77 wt%) rhyolites with relatively low Sr concentrations, but Sr-isotopic values that mirror those of the associated Long Valley basalts (Lange, 2013), which is a key feature of the Long Valley rhyolites (e.g., Metz and Mahood, 1991; Hildreth and Wilson, 2007; Halliday et al., 1984; Davies et al., 1994).

Conclusions and Future Work

There are three broad sets of conclusions that can be drawn from this study regarding the thermal evolution of the crust beneath the Long Valley caldera in eastern California, in response to the emplacement of basaltic magma. First, on the scale of tens of kilometers, as the crustal column gradually heats up due to the random emplacement of basaltic sills, a mixed crustal lithology (solidified mafic sills as well as granitoid) will develop. Importantly, the amount of basalt required to heat >10 km of the crustal column to ~600°C varies strongly with basalt emplacement rate and the depth interval of basalt emplacement. Therefore, the proportion of mafic sills to granitoid in the crustal column can vary by more than a factor of two (e.g., ~1:1 to <1:2), once crustal temperatures reach ~600°C. The abundance and composition of subsequent partial melts of this mixed crustal lithology, at a given T-P_{H2O} condition, will depend strongly on the ratio of mafic sill to granitoid. Therefore, tracking the development of the mixed crustal lithology is as important as tracing the evolving thermal profile through the crust.

A second major conclusion is that in order to accurately track the thermal evolution of the crust due to the influx of basaltic sills, attention must be paid to the transient heating and partial melting of the wall rock adjacent to newly emplaced sills, which depends on the thickness of the basaltic sills as well as the timescale and mechanism by which water is transferred from them to the adjacent wall rock. This requires numerical modeling at high spatial (1 m) and temporal (10-100's of years) resolution, as shown in Figures 7-10. The time scale for the crystallization of the basaltic sills (hundreds of years or less), resulting in the exsolution of a fluid phase, matches the time interval of transient heating of the wall rock. This indicates an effective transfer of water from the crystallizing sill to the wall rock, therefore finite fluid-present conditions prevail and extensive fluid-undersaturated partial melting of wall rock is expected, even when ambient temperatures are below the water-saturated solidus. Moreover, the wall-rock partial melts are expected to be derived from both granitoid and previously solidified mafic sills, and the two sets of compositionally distinct melts are likely to interact during segregation and ascent.

A third conclusion is that some of these wall-rock partial melts may undergo rapid segregation and transport via fractures, owing to large volume increases during partial melting and the development of melt-filled fractures within the adjacent wall rock (owing to melting of pre-existing aplite dikes), which exceed the critical length for dike self-propagation. The advection of these partial melts to higher levels in the crust via fractures will strongly affect the thermal and compositional profile through the middle and upper crust. This is an area of future work and we are currently developing a new numerical 2-D model that will include the advection of these partial melts, operating at the same high spatial (1 m) and temporal (1 hour) resolution as the 1-D model presented in this study.

Acknowledgements

This research was supported by the National Science Foundation (EAR-1855751), as well as discretionary research funds from the University of Michigan (UM). The first author was partially supported by a graduate student fellowship from the Department of Earth and Environmental Sciences at the UM. The model code, a run file, and representative output can be found at DOI: 10.5281/zenodo.3549797; more output available upon request.

References

Anderson, A.T., Davis, A.M., & Lu, F. (2000). Evolution of Bishop Tuff rhyolitic magma based on melt and magnetite inclusions and zoned phenocrysts. *Journal of Petrology*, 41(3), 449-473. https://doi.org/10.1093/petrology/41.3.449

Andersen, N.L., Jicha, B.R., Singer, B.S., & Hildreth, W. (2017). Incremental heating of Bishop Tuff sanidine reveals preeruptive radiogenic Ar and rapid remobilization from cold storage. *Proceedings of the National Academy of Sciences of the United States of America*, 114(47), 12407-12412. https://doi.org/10.1073/pnas.1709581114

Annen, C., Blundy, J.D., & Sparks, R.S.J. (2006). The genesis of intermediate silicic magmas in deep crustal hot zones. *Journal of Petrology,* 47(3), 505-539. http://doi.org/10.1093/petrology/egi084

Annen, C. (2017) Factors affecting the thickness of thermal aureoles. *Frontiers in Earth Science*, 5:82. doi: 10.3389/feart.2017.00082

Bachmann, O., & Bergantz, G.W. (2006). Gas percolation in upper-crustal silicic crystal mushes as a mechanism for upward heat advection and rejuvenation of near-solidus magma bodies. *Journal of Volcanology and Geothermal Research*. 149, 85-102. https://doi.org/10.1016/j.jvolgeores.2005.06.002

Bateman, P.C. (1992) Plutonism in the central part of the Sierra Nevada batholith, California. *U.S. Geological Survey Professional Paper,* 1483, 1-186.

Bailey, R.A. (1989). Geologic map of the Long Valley caldera, Mono-Inyo craters volcanic chain, and vicinity, eastern California. U.S. Geological Survey Map I-1933. https://doi.org/10.3133/i1933

Behrens, H., Meyer, M., Holtz, F., Benne, D. & Nowak, M. (2001). The effect of alkali ionic radius, temperature, and pressure on solubility of water in $MAlSi_3O_8$ melts (M=Li, Na, K, Rb). *Chemical Geology*, 174, 275-289. http://doi.org/10.1016/S0009-2541(00)00320-X

Bindeman, I.N. & Simakin, A.G. (2014). Rhyolites–hard to produce, but easy to recycle and sequester: Integrating microgeochemical observations and numerical models. *Geopshere*, 10(5), 930-957. https://doi.org/10.1130/GES00969.1

Bohrson, W. A. & Spera, F. J. (2001). Energy-constrained open system magmatic processes II: application of energy-constrained assimilation–fractional crystallization (EC-AFC) model to magmatic systems. *Journal of Petrology,* 42, 1019–1041. https://doi.org/10.1093/petrology/42.5.1019

Burnham, C.W., Holloway JR, Davis, N.F. (1969). Thermodynamic properties of water to 1000°C and 10,000 bars. Research and Development Progress Report No. 414, US Department of the Interior. https://doi.org/10.1130/SPE132

Chapman, D. S. & Furlong, K. P. (1992). Thermal state of the continental lower crust. In, Fountain, D. M., Arculus, R. & Kay, R. W. (Eds), *Continental Lower Crust. Developments in Geotectonics.* 23, 179–199.

Christiansen, R.L. (2001). The Quaternary and Pliocene Yellowstone volcanic field of Wyoming, Idaho, and Montana. *US Geological Survey Professional Paper*, 729 G, G1-G145. https://doi.org/10.3133/pp729G

Coleman, D.S., Bartley, J.M., Glazner, A.F., & Pardue, M.J. (2012). Is chemical zonation in plutonic rocks driven by changes in source magma composition or shallow-crustal differentiation? *Geosphere,* 8(6), p. 1568-1587.

Colón, D.P., Bindeman, I.N. & Gerya, T.V. (2018). Thermomechanical modeling of the formation of a multilevel, crustal-scale magmatic system by the Yellowstone plume. *Geophysical Research Letters,* 45, 3873-3879. https://doi.org/10.1029/2018GL077090

Connolly, J.A.D., Holness, M.B., Rubie, D., Rushmer, T. (1997). Reaction-induced microcraking: an experimental investigation of a mechanism for enhancing anatectic melt extraction. *Geology,* 25, 591-594. http://doi.org/10.1130/0091-7613(1997)025<0591:RIMAEI>2.3.CO

Cousens, B.L. (1996). Magmatic evolution of Quaternary mafic magmas at Long Valley caldera and the Devils Postpile, California: Effects of crustal contamination on lithospheric mantle-derived magmas. *Journal of Geophysical Research*, 101(B12), 27673-27689. https://doi.org/10.1029/96JB02093

Davies, G.R., Halliday, A.N., Mahood, G.A. & Hall, C.M. (1994). Isotopic constraints on the production rates, crystallization histories and residence times of pre-caldera silicic magmas, Long Valley, California. *Earth and Planetary Science Letters*, 125(4), 17-37. https://doi.org/10.1016/0012-821X(94)90204-6

Dormand, J., (1996). Numerical Methods for Differential Equations: A Computational Approach, pp. 368, CRC Press LLC, New York.

Du Bray, E.A., John, D.A., Cousens, B.L., Hayden, L.A. & Vikre, P.G. (2016). Geochemistry, petrologic evolution, and ore deposits of the Miocene Bodie Hills volcanic field, California and Nevada. *American Mineralogist*, 101(3), 644-677. https://doi.org/10.2138/am-2016-5440

Dufek, J. & Bergantz, G.W. (2005). Lower crustal magma genesis and preservation: a stochastic framework for the evaluation of basalt–crust interaction. *Journal of Petrology*, 46(11), 2167-2195. https://doi.org/10.1093/petrology/egi049

Fliedner, M.M., Klemperer, S.L. & Christensen, N.I. (2000). Three-dimensional seismic model of the Sierra Nevada arc, California, and its implications for crustal and upper mantle composition. *Journal of Geophysical Research*, 105(B5), 10899-10922. https://doi.org/10.1029/2000JB900029

Flinders, A.F., Shelly, D.R., Dawson, P.B., Hill, D.P., Tripoli, B. & Shen, Y. (2018). Seismic evidence for significant melt beneath the Long Valley Caldera, California, USA. Geology, 46(9), p. 799-802.

Frassetto, A.M., Zandt, G., Gilbert, H., Owens, T.J. & Jones, C.H. (2011). Structure of the Sierra Nevada from receiver functions and implications for lithospheric foundering. *Geosphere*, 7(4), 898-921. https://doi.org/10.1130/GES00570.1

Furlong, K. P., Hanson, R. B., and Bowers, J. R. (1991). "Modeling thermal regimes," in Contact Metamorphism, ed D. M. Kerrick (Chelsea, MI: Mineralogical Society of America), 437–498.

Gazel, E., Plank, T., Forsyth, D.W., Bendersky, C., Lee, C.-T., & Hauri, E.H. (2012). Lithosphere versus asthenosphere mantle sources at the Big Pine Volcanic Field, California. *Geochemistry, Geophysics, Geosystems,* 13(1), 1-25. https://doi.org/10.1029/2012GC004060

Gonnermann, H. & Taisne, B. (2015). Magma transport in dikes. In, Sigurdsson, H. (Ed.), *The Encyclopedia of Volcanoes* (pp. 215-224)

Gualda, G.A.R., Ghiorso, M.S., Lemons, R.V. & Carley, T.L. (2012). Rhyolite-MELTS: a modified calibration of MELTS optimized for silica-rich, fluid-bearing magmatic systems. *Journal of Petrology*, 53(5), 875-890. https://doi.org/10.1093/petrology/egr080

Halliday A.N., Fallick, A.E., Hutchinson, J. & Hildreth, W. (1984). A Nd, Sr, and O isotopic investigation into the causes of chemical and isotopic zonation in the Bishop Tuff, California. *Earth and Planetary Science Letters*, 68(3), 379-391. https://doi.org/10.1016/0012-821X(84)90123-7

Hardin, J. O., (2016). Geological analysis of aplite dikes, Texas Canyon Stock, Arizona. *Honors Thesis, University of Arizona, August 2016*.

Hetland, E.A., Simons, M. & Dunham, E.M. (2010). Postseismic and interseismic deformation due to fault creep I: Model description. *Geophysical Journal International*, 181(1), 81-98. http://dx.doi.org/10.1111/j.1365-246X.2010.04522.x

Hildreth, W. (2004). Volcanological perspectives on Long Valley, Mammoth Mountain, and Mono Craters: several contiguous but discrete systems. *Journal of Volcanology and Geothermal Research*, 136, 169-198. https://doi.org/10.1016/j.jvolgeores.2004.05.019

Hildreth, W., Fierstein, J., & Calvert, A. (2017). Early postcaldera rhyolite and structural resurgence at Long Valley Caldera, California. *Journal of Volcanology and Geophysical Research*, 335, 1-34. https://doi.org/10.1016/j.jvolgeores.2017.01.005

Hildreth, W. & Wilson, C.J.N. (2007). Compositional zoning of the Bishop Tuff. *Journal of Petrology*, 48(5), 951-999. https://doi.org/10.1093/petrology/egm007

Hofmeister, A.M. (1999). Mantle values of thermal conductivity and the geotherm from phonon lifetimes. *Science*, 283, 1699. https://doi.org/10.1126/science.283.5408.1699

Holbrook, W. S., Mooney, W. D. & Christensen, N. I. (1992). The seismic velocity structure of the deep continental crust. In, Fountain, D. M., Arculus, R. & Kay, R. W. (Eds), *Continental Lower Crust*. Amsterdam: Elsevier, pp. 1–43

Huang, W. & Russell, R.D. (2011). Adaptive moving mesh methods. *Applied mathematical sciences*. (Vol. 174). New York, NY: Springer. https://doi.org/10.1007/978-1-4419-7916-2

Huppert, H.E. & Sparks, R.S.J. (1988). The generation of granitic magmas by intrusion of basalt into continental crust. *Journal of Petrology*, 29(3), 599-624. https://doi.org/10.1093/petrology/29.3.599

Jackson, M.D., Cheadle, M.J. & Atherton, M.P. (2003). Quantitative modeling of granitic melt generation and segregation in the continental crust. *Journal of Geophysical Research*, 108(B7), 2332, https://doi.org/10.1029/2001JB001050

Karakas, O. & Dufek, J. (2015). Melt evolution and residence in extending crust: Thermal modeling of the crust and crustal magmas. *Earth and Planetary Science Letters*, 425, 131-144. https://doi.org/10.1016/j.epsl.2015.06.001

Kay, R. W., Kay, S. M & Arculus, R. J. (1992). Magma genesis and crustal processing. In, Fountain, D. M., Arculus, R. & Kay, R. W. (Eds), *Continental Lower Crust*. Amsterdam: Elsevier, pp. 423–445.

Johannes, W. & Holtz, F (1996). *Petrogenesis and Experimental Petrology of Granitic Rocks:* Minerals and Rock Series, Volume 22, Berlin, Springer-Verlag, 335 p. https://doi.org/10.1093/petroj/38.1.165

Lange, R.A. (1997). A revised model for the density and thermal expansivity of K_2O-Na_2O-CaOMgO-Al_2O_3-SiO_2 liquids from 700-1900 K: extension to crustal magmatic temperatures. *Contributions to Mineralogy and Petrology*, 130, 1-11. https://doi.org/10.1007/s004100050345

Lange, R.A. (2013). The origin of highly evolved, voluminous rhyolites by progressive, multiple episodes of partial melting: the resolution of several paradoxes. Geochemical Society Ingerson Lecture, Geological Society of America *Abstracts with Programs*, vol. 45, no. 7, p. 84.

Lange, R.A. (2019). Evidence for rapid transport of rhyolite melt during hydrous partial melting of granitoid: the critical role of pre-existing aplite dikes and fluid-undersaturated conditions. *American Geophysical Union Fall Meeting Abstracts,* V44A-01.

Leeman, W.P., Annen, C. & Dufek, J. (2008). Snake River Plain – Yellowstone silicic volcanism: implications for magma genesis and magma fluxes. *Geological Society, London, Special Publications*, 304, 235-259. https://doi.org/10.1144/SP304.12

Levander, A. & Miller, M.S. (2012). Evolutionary aspects of lithosphere discontinuity structure in the western U.S. *Geochemistry, Geophysics, Geosystems*, 13(7), Q0AK07. https://doi.org/10.1029/2012GC004056

Lim, S.H., Hetland, E.A. & Lange, R.A. (2012). Numerical models of transient partial melting of the lower crust during repeated emplacement of basalt sills and subsequent cooling due to advection of melt out of the lower crust. Abstract T31G-2708. Presented at 2012 Fall Meeting, AGU, San Francisco, Calif., 3-7 Dec.

Manley C.R., Glazner, A.F. & Farmer, G.L. (2000). Timing of volcanism in the Sierra Nevada of California: Evidence for Pliocene delamination of the basaltic root? *Geology*, 28(9), 811-814. https://doi.org/10.1130/0091-7613(2000)28<811:TOVITS>2.0.CO;2

McKenzie, D. (1984). The generation and compaction of partially molten rock. *Journal of Petrology*. 25(3), 713-765. https://doi.org/10.1093/petrology/25.3.713

Metz, J.M. & Mahood, G.A. (1991). Development of the Long Valley, California, magma chamber recorded in precaldera rhyolite lavas of Glass Mountain. *Contributions to Mineralogy and Petrology*, 106(3), 379-397. https://doi.org/10.1007/BF00324565

Noda, H., Dunham, E. & Rice, J., (2009). Earthquake ruptures with thermal weakening and the operation of major faults at low overall stress levels. *Journal of Geophysical Research*, 114, B07302, https://doi.org/10.1029/2008JB006143

Ochs, F.A. & Lange, R.A. (1999). The density of hydrous magmatic liquids. *Science*, 283(5406), 1314-1317. https://10.1126/science.283.5406.1314

Oliver, H.W., Moore, J.G. & Sikora, R.F. (1993). Internal structure of the Sierra Nevada batholith based on specific gravity and gravity measurements. *Geophysical Research Letters*, 20(20), 2179-2182. https://doi.org/10.1029/93GL01379

Petford, N. & Gallagher, K. (2001). Partial melting of mafic (amphibolitic) lower crust by periodic influx of basaltic magma. *Earth and Planetary Science Letters*, 193(3-4), 483-499. https://doi.org/10.1016/S0012-821X(01)00481-2

Rubin, A.M. (1995). Propagation of magma-filled cracks. *Annual Review of Earth and Planetary Sci*ences, 23, 287-336. https://doi.org/10.1146/annurev.ea.23.050195.001443

Rubin, A.M. (1998). Dike ascent in partially molten rock. *Journal of Geophysical Research,* 103, 20901-20919. https://doi.org/10.1029/98JB01349

Rudnick, R.L. & Gao, S. (2014). Composition of the continental crust. Treatise on Geochemistry, 2nd, 4, 1-51. https://doi.org/10.1016/B978-0-08-095975-7.00301-6

Rushmer, T. (2001). Volume change during partial melting reactions: implications for melt extraction, melt geochemistry and crustal rheology. *Tectonophysics*, 342, 389-405. https://doi.org/10.1016/S0040-1951(01)00172-X

Saleeby, J., Ducea, M.& Clemens-Knott, D. (2003). Production and loss of high-density batholitic root, southern Sierra Nevada, California. *Tectonics*, 22(6), 1064. https://doi.org/10.1029/2002TC001374

Simakin, A.G. & Bindeman I.N. (2012). Remelting in caldera and rift environments and the genesis of hot, "recycled" rhyolites. *Earth and Planetary Science Letters*, 337-338, 224-235. https://doi.org/10.1016/j.epsl.2012.04.011

Simon, J.I., Weis, D., DePaolo, D.J., Renne, P.R., Mundil, R. & Schmitt, A.K. (2014). Assimilation of preexisting Pleistocene intrusions at Long Valley by periodic magma recharge accelerates rhyolite generation: rethinking the remelting model. *Contributions to Mineralogy and Petrology*, 167, 955. https://doi.org/10.1007/s00410-013-0955-5

Sleep, N.H., (1988). Tapping of melt by veins and dikes. *Journal of Geophysical Research*, 93(B9), 10,255–10,272. https://doi.org/10.1029/jb093ib09p10255

Solano, J.M.S., Jackson, M.D., Sparks, R.S.J. & Blundy, J. (2014). Evolution of major and trace element composition during melt migration through crystalline mush: Implications for chemical differentiation in the crust. *American Journal of Science*, 314(5), 895-939. https://doi.org/10.2475/05.2014.01

Spera, F.J., & Bohrson, W.A. (2018). Rejuvenation of crustal magma mush: A tale of multiply nested processes and timescales. *American Journal of Science*, 318, 90-140. https://doi.org/10.2475/01.2018.05

Stachnik, J.C. Dueker, K., Schutt, D.L., & Yuan, H. (2008), Imaging Yellowstone plume - lithosphere interactions from inversion of ballistic and diffusive Rayleigh wave dispersion and crustal thickness data. *Geochemistry. Geophysics. Geosystems*., 9, Q06004, https://doi.org/10.1029/2008GC001992.

Thurber, C., Zhang, H., Brocher, T. & Langenheim, V. (2009). Regional three-dimensional seismic velocity model of the crust and uppermost mantle of northern California. *Journal of Geophysical Research*, 114, B01304, https://doi.org/10.1029/2008JB005766

Wallace, P.J., Anderson, A.T. & Davis, A.M. (1999). Gradients in H_2O, CO_2, and exsolved gas in a large-volume silicic magma system: Interpreting the record preserved in melt inclusions from the Bishop Tuff. *Journal of Geophysical Research*, 104(B9), 20097-20122. https://doi.org/10.1029/1999JB900207

Waters, L.E., & Lange, R.A., (2017). Why aplites freeze and rhyolites erupt: Controls on the accumulation and eruption of high-SiO2 (eutectic) melts. *Geology*, 45(11), 1019-1022. https://doi.org/10.1130/g39373.1

Wilson, C.J.N. & Hildreth, W. (1997). The Bishop Tuff: new insights from eruptive stratigraphy. *The Journal of Geology*, 105(4), 407-440. https://doi.org/10.1086/515937

Yuan, H., & Dueker, K. (2010). Crustal structure and thickness along the Yellowstone hot spot track: Evidence for lower crustal outflow from beneath the eastern Snake River Plain. *Geochemistry, Geophysics, Geosystems*. 11, 3. https://doi.org/10.1029/2009GC002787

Zandt, G., Hersh, G., Owens, T.J., Ducea, M., Saleeby, J. & Jones, C.H. (2004). Active foundering of a continental arc root beneath the southern Sierra Nevada in California. *Nature*, 431(7004), 41-46. https://doi.org/10.1038/nature02847

Zhang, Y., Xu, Z., Zhu, M. & Wang, H. (2007). Silicate melt properties and volcanic eruptions. *Review of Geophysics*, 45(4), RG4004, https://doi.org/10.1029/2006RG000216

CHAPTER 3

The Generation and Transport of Mixed Rhyolitic Melts Derived from Basaltic Intrusions and Partial Melting of Granitoid Wall Rock: Implications for the Origin of the Plio-Quaternary Magmatic Parent to the Bishop Tuff Rhyolite, Long Valley, CA.

Abstract

We present a new, high-resolution numerical model of the thermal evolution of the crustal column beneath Long Valley caldera, CA, a site of voluminous rhyolitic volcanism over the past 2.2 Myr, driven by the influx of basaltic magmas. This model, called the Transient High-resolution Partial Melting Simulation of the Crust (TIRAMISU), expands on previous work by incorporating the transport of secondary melts (i.e., partial melts of wall rock and residual melts of crystallizing basaltic sills), which significantly alter crustal-scale thermal and compositional profiles. In this study, we assume a single set of input parameters which are consistent with current understandings of magmatism in extensional tectonic settings, including: (1) basalt emplacement rate of 50 m per 5 kyr, with 3 km cumulative basalt emplaced, (2) randomly emplaced basaltic sills into an initial depth interval of 20–30 km, and (3) secondary sills randomly emplaced into an initial depth interval of 18–20 km. Secondary melt segregation, transport and emplacement at shallower depths is implemented through a physically inspired set of criteria. In these simulations, about 55–60% of the cumulative thickness of the emplaced basalt was transported to secondary sills as rhyolitic melt. About ~70% of all transported rhyolite was derived from granitoid wall rock and the remainder from basaltic sources (both partial melts of solidified sills and residual, fluid-saturated melt). These simulations demonstrate that the effect of secondary melt removal results in about 60ºC of cooling in the lower crust (over about

24-35 km) compared to when there is no secondary melt movement. The subsequent emplacement of secondary melts in the middle crust resulted in about 60°C of heating between 17-21 km, relative to simulations with no secondary melt transport. These findings show that the incorporation of the transport of secondary melts strongly alters crustal-scale thermal profiles. The Long Valley rhyolites are hydrous, and have are severely depleted in Sr, but they require H_2O transferred from local hydrous basalts which are also enriched in Sr. Volatile transfer without trace element contamination was also explored in this study, through tracking of the Sr concentration and isotopic signature of the secondary melts on the basis of average compositional values for the granitoid wall rock and basaltic input. Results indicate that basaltic sources contribute ~30% of the rhyolitic partial melt, yet they contribute ~60% of the Sr in the first stage of crustal melting. In addition, procedures to track other compositional parameters (e.g., Nd) are outlined, which will assist future numerical simulations in more tightly constraining the multi-stage process by which the Long Valley rhyolites were formed.

Introduction

High-silica rhyolite (≥ 75 wt% SiO_2), with a near-eutectic composition (i.e., a narrow liquidus-solidus interval of ~40 degrees), is the most differentiated silicate magma type on Earth and makes up some of the largest explosive eruptions in the western United States over the last 1 Myr (e.g., Yellowstone, Wyoming and Long Valley, California). An outstanding question is why high-SiO_2 rhyolite is so voluminous in extensional tectonic settings (e.g., at Long Valley, CA and Yellowstone, WY), and yet so scarce as an erupted whole-rock magma type at subduction zones (e.g., Hildreth, 2007).

Given the common association of high-SiO_2 rhyolite erupting bimodally with basalt in extensional tectonic settings, there is general consensus from numerical modeling that the influx of basaltic magma into granitoid crust is a fundamental driving force for the origin of high-SiO_2 rhyolites (e.g., Huppert and Sparks, 1988; Leeman et al., 2008; Karakas and Dufek, 2015; Colón et al., 2018). There is abundant geochemical evidence from both Yellowstone (e.g., Hildreth et al., 1991) and Long Valley rhyolites (e.g., Halliday et al., 1984; 1989; Davies et al., 1994; Simon et al., 2014) that both interstitial melt from basaltic intrusions and partial melts of pre-existing crust contribute to the formation of rhyolitic melts, but through a set of multi-stage, complex processes that are not tightly constrained.

The primary focus of this study is the origin of the high-SiO_2 rhyolites that have erupted from the Long Valley volcanic field, CA, over the last 2.2 Myr, including the Glass Mountain obsidians (~100 km^3; Metz and Mahood, 1991) and the caldera-forming eruption at ~765 ka (Andersen et al., 2017) of the Bishop Tuff (>600 km^3; Hildreth and Wilson, 2007). Most numerical thermal models that address the origin of rhyolites have focused on those derived from the Yellowstone plume (e.g., Leeman et al., 2008; Simakin and Bindeman, 2012; Bindeman and Simakin, 2014; Colon et al., 2018). However, a notable difference is that the Long Valley rhyolites have much higher H_2O contents (≤ 6.5 wt%; Wallace et al., 1999; Anderson et al., 2000; Roberge et al., 2013) than those from Yellowstone (≤3.5 wt% H_2O; Befus et al., 2012, 2014). This difference raises the question of the origin of dissolved H_2O in the Long Valley rhyolites. The source of the water in the Long Valley rhyolites cannot be pre-existing granitoid crust, which contains contents <0.6 wt% H_2O held in biotite and hornblende, and instead must ultimately be derived from associated basalts, shown to contain ~3-6 wt% H_2O (Jolles, 2020).

It is puzzling how this transfer of water occurs, given that the Long Valley basalts have notably high Sr concentrations (~1000-2000 ppm; Cousens, 1996), whereas the Glass Mountain obsidians (~100 km^3) and Early Bishop Tuff (>400 km^3) have remarkably low Sr contents (0.1-4 ppm and <30 ppm, respectively; Halliday et al., 1989; Hildreth and Wilson, 2007). To add to the complexity, the Long Valley high-SiO_2 rhyolites have Sr- and Nd-isotopic values that are most similar to associated basalts and not the pre-existing granitoid crust (e.g., Halliday et al., 1984, 1989; Davies et al., 1994; Cousens, 1996), as seen in Figure 3-1. A primary objective of this study is to understand how water and the Sr isotopic values were transferred from the basalts to the rhyolites, without contaminating them with their high Sr contents. While back-of-the-envelope calculations can relate amounts of partial melt with relevant concentrations through elemental partitioning, one aim of this study is to identify which specific ratio may occur in the first stage of secondary melt transport, to inform further calculations of Sr and other trace elements, under the initial condition constraints which Long Valley caldera presents.

This study builds directly on our previous work (Calogero et al., 2020), where we developed high-resolution numerical model of the thermal evolution of the crustal column beneath Long Valley caldera. The first part of that study examined how randomly emplaced basaltic sills of variable thickness, at various depth intervals, and at variable emplacement rates gradually heat the crust and lead to a variably mixed crustal lithology (solidified mafic sills and pre-existing granitoid). The second part focused on sill-scale processes that required high spatial (≥1 m) and temporal (≥ days) resolution. One of the key findings of Calogero et al. (2020) is that significant partial melting of wall rock occurs along the margins of newly emplaced basaltic sills, even when ambient crustal temperatures are sub-solidus. Transient heating of adjacent wall rock was shown to range over time scales (10^1–10^2 years) that match those for exsolution of volatiles

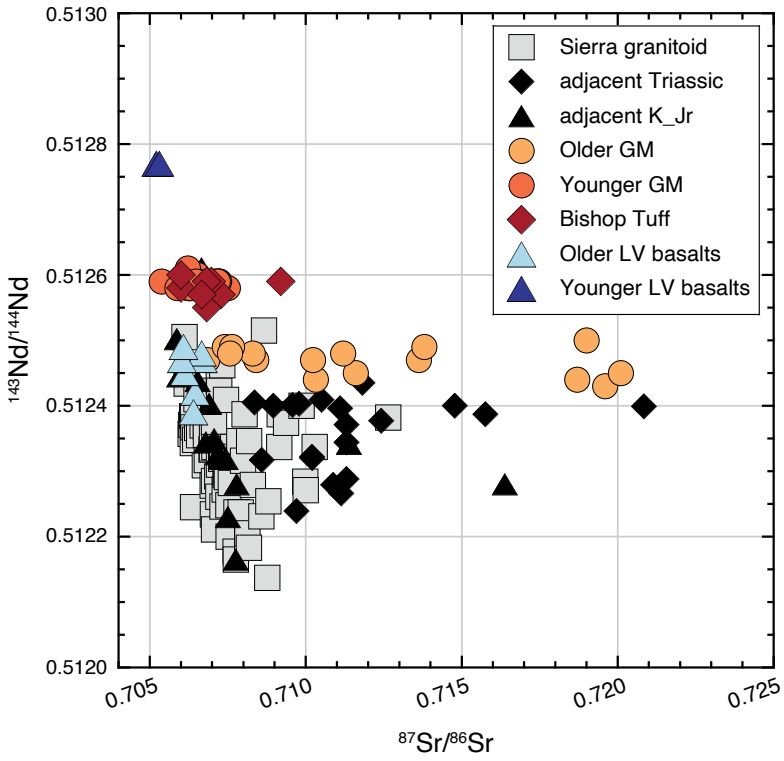

Figure 3-1. Plot of $^{143}Nd/^{144}Nd$ vs. $^{87}Sr/^{86}Sr$ isotopic compositions for plutonic and volcanic rock units relevant to the Long Valley magmatic system. Literature sources for these data are listed in Table 3-1. Triassic and Cretaceous-Jurassic granitoid units, which outcrop adjacent to the Long Valley caldera region, are shown by black diamond and black triangles; all other Sierra granitoid units (with $^{87}Sr/^{86}Sr$ values ≥0.706) are shown with gray boxes. Older and Younger GM refer to Glass Mountain rhyolites erupted along the northern margin of Long Valley caldera pre- and post 1.2 Ma, respectively. The Bishop Tuff rhyolite (>600 km^3 erupted at ~765 ka to form the Long Valley caldera; Andersen et al., 2017) is shown by dark red diamond. The Older and Younger Long Valley basalts refer to all high-MgO (>7 wt%) basalts that erupted pre- and post-caldera, respectively. All Sierra Nevada granitoid isotopic data are those measured (i.e., not age-corrected to initial values) since these are the relevant values for partial melting events in the Plio-Quaternary. Conversely, all the Long Valley rhyolite (i.e., GM and Bishop Tuff) isotopic data are corrected to values at the time of their eruption, since these are the relevant values when tracking the isotopic signature of their source rocks. Note that the Long Valley rhyolites all have Nd isotopic compositions that are shifted to higher values than those for granitoid in the crustal column, consistent with a strong influence from Long Valley basalts. Note also that the younger GM and Bishop Tuff rhyolites have an average Nd isotopic signature that is intermediate between the older and younger Long Valley basalts, which points to both suites of basalts playing a role in their origin.

from crystallizing basaltic sills. Owing to large volumes of fusion (>10%) during hydrous (fluid-undersaturated) partial melting of granitoid wall rock, combined with the regional pre-existence of ubiquitous, scattered aplite dikes (of near-eutectic, high-SiO_2 rhyolite composition), transport of wall-rock partial melts will readily occur in melt-filled fractures that exceed the critical length

of a self-propagating dike (see Calogero et al., 2020 for a discussion) and the critical width to keep from freezing during transport, which is discussed further below.

In this study, we present a significant expansion of the numerical thermal model presented in Calogero et al., (2020), which we refer to as TIRAMISU (Transient hIgh-Resolution pArtial MeltIng Simulation of the crUst). This model, which we have ported to the Julia programming language (Bezanson et al., 2017), addresses thermal diffusion at the crustal, kilometer-scale, while still achieving high-resolution at the meter scale in magma injections, as sills, and the surrounding wall rock. We furthermore incorporate the segregation and ascent of partial melts when temporal and spatial criteria are met. TIRAMISU maintains high spatial resolution over both the region of the primary basaltic sill and the secondary rhyolitic sill, when it occurs. This high resolution allows us to capture the details of the localized partial melting of the wall-rock and is crucial to be able to address potential secondary rhyolitic melt ascent. Here we include an exploration of the likely geochemical intermixing, during segregation and ascent, of wall-rock partial melts with fluid-saturated interstitial melts from adjacent, crystallizing basaltic sills. The whole-rock compositions of ascending melts have three possible sources: (1) hydrous (fluid-undersaturated) partial melts of granitoid, (2) hydrous (fluid-undersaturated) partial melts of previously solidified basaltic sills, and (3) hydrous (initially fluid-saturated) interstitial melts from crystallizing basaltic sills. The relative contribution from each of these sources will control the major- and trace-element compositions of the mixed rhyolitic melts, including their water concentrations and isotopic signatures, and in TIRAMISU we rigorously track the extent of physical and compositional contribution from each source.

The primary goals of this study are three-fold: (1) To present a new thermal model capable of addressing the transport of partial melts at high resolution through the application of

temporal and spatial criteria in determining the extent of available partial melt (variably intermixed with interstitial melt of crystallizing basaltic sills). (2) To track the composition of these ascending melts. (3) To evaluate the resulting thermal and compositional profile of the crustal column. The ascent of partial melts significantly alters the crustal-scale thermal profile by cooling their source regions and heating shallower levels of the crust where they are emplaced. In addition, gradual accumulation of melts in in the upper-middle crust will create a relatively large volume of Plio-Quaternary leucogranite, with a whole-rock composition and isotopic signature that is substantially different than that of the Mesozoic granitoid that forms the pre-existing crustal basement beneath Long Valley, CA.

Tectonic and Geochemical Background for Numerical Modeling

A broad overview of the tectonic and geological setting of the Long Valley magmatic system, located along the western margin of the Basin and Range extensional province in eastern California, is presented in Calogero et al. (2020). The most salient aspects for this study are reviewed here, in addition to relevant geochemical information from the literature on the basement rocks beneath Long Valley as well as the various volcanic products erupted in the region. The underlying crustal column (≤ 32 km; Fliedner et al., 2000) is dominated by Mesozoic granitoid of the Sierra Nevada batholith. Triassic-Jurassic granitoids outcrop along the eastern margin of Long Valley (e.g., Barth et al., 2011), whereas Cretaceous granitoids predominate along the western margin (e.g., Oliver et al., 1993; Coleman and Glazner, 1997). A summary of the average Nd and Sr isotopic values (and concentrations) of these granitoid rocks is provided in Table 3-1.

Basaltic volcanism in the region began ~4.5 Ma (Bailey, 1989), derived by partial melting of subduction-modified lithosphere during Basin and Range extension (e.g., Cousens, 1996; Cousens et al., 2012), and has continued into the Holocene (e.g., Hildreth, 2004). The Long Valley basalts that erupted before and after the caldera-forming eruption of the Bishop Tuff (~765 ka; Andersen et al., 2017) fall into two compositionally distinct groups. The older basalts have a more enhanced arc geochemical signature (e.g., elevated K, Sr, Nd concentrations), as well as higher $^{87}Sr/^{86}Sr$ and lower $^{143}Nd/^{144}Nd$ values relative to the younger basalts (Table 3-1).

Average	**Sr (ppm)**	**Nd (ppm)**	**$^{87}Sr/^{86}Sr$**	**$^{143}Nd/^{144}Nd$**	**D_{Sr}**	**D_{Nd}**
SN Granitoid (>0.706) ***[1]***	490	22	0.7085	0.51233		
Triassic Granitoid ***[2]***	258	16	0.7121	0.51236		
K–Jr Granitoid ***[3]***	500	20	0.7079	0.51236		
Older Long Valley Basalt ***[4]***	1477	53	0.7064	0.51245		
Young Long Valley Basalt ***[5]***	563	16	0.7053	0.51277		
Older Glass Mountain ***[6]***	2	20	0.7135	0.51247		
Younger Glass Mountain ***[7]***	2	20	0.7066	0.51259		
Avg. E/T Bishop Tuff ***[8]***	13	21	0.7070	0.51258		
Parent to E/T Bishop Tuff ***[9]***	32	32	0.7070	0.51258	3.2	1.89
SN Granodiorite ***[10]***	450	20	0.708	0.51235	3.2	3.5
Older Long Valley Basalt ***[11]***	1300	50	0.706	0.51245	2	0.45
Younger Long Valley Basalt ***[11]***	550	16	0.705	0.51277	2	0.15
Emplaced Leucogranite ***[10]***					3.2	1.89

Table 3-1. Geochemical data used in numerical simulations [1] Average of all Sierra Nevada granitoid east of $^{87}Sr/^{86}Sr \geq 0.706$ line (NAVDAT, 2014) [2] Average of Triassic granitoid adjacent to Long Valley caldera (Barth et al., 2011) [3] Average of K-Jr granitoid (e.g., Tuolomne) adjacent to Long Valley caldera (Kistler et al., 1986; Cousens, 1996; Coleman & Glazner, 1997; Economos et al., 2010) [4] Average of Pliocene-Older Long Valley basalt >7 wt% MgO (Cousens, 1996) [5] Average of post-caldera Long Valley basalt >7 wt% MgO (Cousens, 1996) [6] Average of older (>1.2 Ma) Glass Mountain rhyolites (Halliday et al., 1989; Davies et al., 1994) [7] Average of younger (<1.2 Ma) Glass Mountain rhyolites (Halliday et al., 1989; Davies and Halliday, 1998) [8] Early/Transitional Bishop Tuff (>400 km3 high-SiO_2 rhyolite) (Halliday et al., 1984; Davies and Halliday, 1998) [9] Estimates of Sr and Nd concentrations and bulk D_{Sr} and D_{Nd} for parent to E/T Bishop rhyolite from Jolles (2020) [10] Average values for Mesozoic granodiorite and Plio-Quaternary leucogranite wall rock; estimates of bulk D_i from Prowatke and Klemme (2006) and Jolles (2020); values used in numerical simulations [11] Average values for older and younger Long Valley basalts (Cousens, 1996); estimates of bulk D_i from Klein et al. (1997) and Pertermann and Hirschmann (2002); values used in numerical simulations.

The influx of Plio-Quaternary basalts into the crustal column beneath Long Valley eventually led to the effusive eruption of ~100 km^3 of high-SiO_2 rhyolite between 2.2 and 0.8 Ma to form the Glass Mountain (GM) complex (Metz and Mahood, 1991). These highly differentiated rhyolites fall into two isotopically distinct groups, also separated in time (pre- and post-1.2 Ma; Halliday et al., 1989). The older GM rhyolites have higher $^{87}Sr/^{86}Sr$ and lower $^{143}Nd/^{144}Nd$ values relative to the younger GM rhyolites (Halliday et al., 1989; Davies et al., 1994; Davies and Halliday, 1997). Interestingly, both groups of GM rhyolites have nearly identical Sr and Nd concentrations (<4 and ~22 ppm, respectively; Metz and Mahood, 1991), despite their notable difference in isotopic signatures. The caldera-forming eruption of the Bishop Tuff at ~765 ka (Andersen et al., 2017) produced ~600 km^3 of zoned rhyolite (77-73 wt% SiO_2; Hildreth and Wilson, 2007) over the course of ~6 days (Wilson and Hildreth, 1997). Of this volume, >400 km^3 is high-SiO_2 rhyolite (77-76 wt%) and is isotopically indistinguishable from the younger GM rhyolites (see Figure 3-1), although the Bishop rhyolite contains slightly higher Sr concentrations and slightly lower Nd concentrations (Table 3-1).

Following the catastrophic Bishop Tuff eruption, ~100 km^3 of low-SiO_2 rhyolite (called the "Early" post-caldera rhyolite by Bailey, 1989) were erupted from ~750-640 ka (Hildreth et al., 2017). Within the last 600 kyr, ≤8 km^3 of rhyolite was erupted within the caldera (Hildreth, 2004; Simon et al., 2014). A summary of their geochemical characteristics is found in Hildreth et al. (2017).

Numerical Methods

Numerical Model

Our simulation tool presented here, TIRAMISU, is an extension of that we presented in Calogero et al. (2020), with the major addition that we now include secondary transport of partial melts. TIRAMISU is implemented in Julia (Bezanson et al., 2017). Julia is a scripted language, similar to Python or Matlab, but numerical benchmark algorithms in Julia have computation speeds approaching those benchmarks implemented in C (https://julialang.org/benchmarks/; accessed Jan. 2021). Specifically, we solve for the evolution of temperature and transient melting in response to episodic emplacements of basaltic magma in sills, which in this 1-D simulation are horizontal layers with infinite lateral extent. In TIRAMISU we include the ability to allow for a stage of secondary movement of melt within the crustal column, which is triggered if criteria described below are met. TIRAMISU includes tracking of the compositional evolution of the full crust as a consequence of the secondary melt transport.

TIRAMISU is a finite-difference solution to the 1-D transient thermal diffusion equation, with heterogeneous material properties,

$$\rho C_p \frac{\partial T}{\partial t} + \rho L \frac{\partial F}{\partial t} = \frac{\partial}{\partial x} k(x) \frac{\partial T}{\partial x} \quad (1)$$

where ρ is density, C_p is specific heat capacity, L is the latent heat, $k(x)$ is thermal conductivity, T is temperature, F is melt fraction, t is time, and x is depth. The finite difference method in TIRAMISU includes variable spatial resolution, achieved through non-uniform node spacing, and temporal resolution, achieved through an adaptive Runge-Kutta solution. Our finite difference approach is described fully in Calogero et al. (2020) and we refer readers there for details of the discretization of the diffusion equation and our finite-difference numeric solution.

TIRAMISU includes the ability to vary the thicknesses, initial temperatures, and times of emplacements of each of the basaltic sills, either at specific locations or randomly within a depth range. In the present simulations, we assume uniform thicknesses, temperatures, and periodic emplacements of all basaltic sills, with the depth of the basaltic sills determined randomly. Basaltic sills are 50 m thick and are emplaced every 5 kyr, consistent with reasonable emplacement rates for extensional tectonics (e.g., Karakas & Dufek, 2015). Sills have an initial temperature of 1150ºC, and are placed randomly within an initial depth range of 20–30 km. The depth range evolves during the simulation, thickening as basaltic sills are emplaced, and thinning as those sills thermally compact or when secondary melt is extracted and moved up the crustal column. Simulations were run for at least 60 cycles, where a cycle is the duration between emplacements of the basaltic sills (60 sills emplaced every 5 kyr results in a simulation time of 300 kyr). For reference, the maximum temperature difference for a 1 million year simulation at a rate of 1 sill per 10 kyr is <5ºC (5 m spacing cooler vs. 1 m spacing; cf. Figure 2-3).

Immediately after sill emplacement, we solve Equation (1) for the evolution of temperature, solidification of the sill, and transient melting of the surrounding crust, on the high-resolution node mesh. Each time a basaltic sill is emplaced in the crust, we redistribute node positions in order to resolve the basaltic sill and surrounding crust with high node density, while also allowing lower node density far from the sill, where the curvature of temperature fields is gentler. To simplify the code, the number of nodes is used at every time step is constant. In TIRAMISU, the adaptation of the node positions is simpler than that used in Calogero et al. (2020), with nodes spaced evenly with a prescribed minimum spacing within the sill, as well as over a region above and below the sill equal to the sill half-thickness. Within TIRAMISU every sill has to be defined by at least three nodes, corresponding to the top, center, and bottom of the

sills, whether those sills are primary or secondary sills and regardless of the degree of solidification of those sills. Note that in the simulations presented here, the most recent sills are defined by far more than three nodes, although past sills that have completely solidified and whose temperature has equilibrated to the surrounding crust may be defined by three nodes. Node spacing then increases roughly geometrically away from the sill. In the node distribution, we ensure that all material boundaries are respected, including all past sills, regardless of their level of cooling and solidification. As a result of this, node spacing away from the sills may not increase perfectly geometrically and some regions of the domain may have nodal spacings below the minimum node spacing, for instance, if two past sills were randomly placed very near each other. Higher spatial resolution, as well as the accumulation of more sills within the domain, result in slower run times, as the time steps in the finite difference solution are also smaller. For example, a 600-node simulation without secondary melt transport, and with 5 m minimum spacing, requires about 9 minutes of computation time on a circa 2015 desktop workstation per emplacement cycle. In contrast, a 1200 node simulation with the same basaltic sill emplacement history and a 2 m minimum spacing, requires about 75 minutes per cycle, regardless of whether secondary melt transport occurs during a cycle.

We specified a 2 m minimum resolution in simulations that included a secondary melt transport stage, and 5 m minimum resolution in simulations only considering the solidification of the primary basaltic sills. We used 1200 total nodes in simulations with secondary melt transport, allowing sufficient nodes to capture the details of partial melting of wall rock, as well as model the solidification of the thinner secondary sills. Simulations in which secondary melt transport is not considered use 600 total nodes, which we found is sufficient density to resolve the cooling of only the primary basaltic sills.

In the present version of TIRAMISU, secondary melt transport is triggered when two criteria are met, one temporal and one spatial. The temporal criterion is based upon the timing of H_2O exsolution from the primary basaltic sill into wall rock, which is dependent on the basalt melt fraction-temperature (FT) relationship, ambient temperature, and to a lesser degree the local lithology, as identified in Calogero et al., (2020). The spatial criterion is rooted in the simulation resolution and is chosen to maximize the thickness included in the secondary melt. A discussion on how each criterion is identified and applied within TIRAMISU is presented in the "Transport of Rhyolitic Melts" section below. The secondary melt includes residual basaltic melt and partial melt of the surrounding crust, and we refer to the region over which melt is removed as the "evacuated region". Whenever melt is segregated and transported, new material boundaries are created to demarcate the evacuated region, as the composition of that region will change. When secondary melt is extracted from wall rock adjacent to the basaltic sill, the evacuated region also has additional material boundaries associated with the residual primary sill. Secondary melt is moved instantaneously from the location of the primary sill to shallower depths in the crust. By assuming the melt moves instantaneously, we assume that as the secondary melt does not deposit heat to the surrounding crust which it moves through, nor does melt accumulate anywhere other than in the secondary sill.

The secondary melt is more evolved than its compositional sources, and the evacuated source regions become more refractory upon melt segregation. These compositional changes are taken to account within TIRAMISU, allowing the ability to simulate the petrological evolution of the crust. In addition to material property changes in the evacuated region, the solidus temperature also increases, as a proxy for what mineralogical changes occur when a partial melt is removed from the source.

Initial conditions and material boundary evolution

We assume an initial model of 40 km depth, with the Moho depth at 35 km. We apply a 20ºC/km geothermal gradient, consistent with the seismically imaged lithosphere-asthenosphere boundary at 60 km depth in the Basin & Range (Levander & Miller, 2012). Material properties of the basaltic sills reflect Long Valley basalts (Cousens, 1996; Table 2). We assume a granitoid composition extending from the surface to 32 km depth, with material properties reflective of the Sierra Nevada batholith (Table 3-2). The lower crust, initially extending from 32 to 35 km, is assumed to be broadly amphibolite, and the underlying mantle is peridotite; and we use the same material properties for both as presented in Annen et al. (2006).

Tracking the composition of secondary (rhyolitic) melts undergoing transport

There are three distinct sources for the melts which are available to be moved to a secondary sill: (1) partial melts of the granitoid, (2) partial melts of previously solidified mafic sills, and (3) residual melt of crystallizing basaltic sills. In this study, the melt fraction versus temperature (FT) curves for hydrous (finite fluid present) granitoid and basalt presented in Calogero et al. (2020) are employed. Under identical temperature and P_{H2O} conditions, higher-degree partial melts will be derived from wall-rock made of granitoid than solidified mafic sills (e.g., melt fractions of 30 vs. 5% respectively at 750°C and 0.5 GPa; Calogero et al., 2020). Irrespective of melt fractions, hydrous partial melts of granitoid will be near-eutectic melts (e.g., Johannes and Holtz, 1996), and thus broadly constrained to be high-SiO_2 (>75 wt%) rhyolites. In the case of mafic sills, low-degree (<10%) partial melts are typically low-SiO_2 (≥70 wt%) rhyolite (e.g., Sisson et al., 2005). Similarly, during late-stage crystallization of basaltic sills,

		Mantle	Lower Crust	Granitoid	Basalt	Granitoid *(Evac)*	Solidified Mafic Sill *(Evac)*	Rhyolite ***from Granitoid***	Rhyolite ***from Basalt***
Density (solid) $\boldsymbol{kg/m^3}$ *[1]*	ρ_S	3400	3050	2700	3100	2750	3200	2650	2650
Density (melt) $\boldsymbol{kg/m^3}$ *[2]*	ρ_M			2400	2510	2425	2550	2300	2325
Specific Heat *[3]* $\boldsymbol{J/(kg \cdot K)}$	Cp	1131	1390	1200	1300	1200	1300	1200	1200
Latent Heat *[3]* $\boldsymbol{10^3 J/kg}$	L		3.5	2.7	4.0	2.7	4.0	2.7	2.7
Conductivity *[3]* $\boldsymbol{J/(s \cdot m \cdot K)}$	k	3.4	2.6	2.8	2.6	2.8	2.6	2.8	2.8
Melt Compaction		0	0	0.08	0.1	0.08	0.1	0.08	0.08

Table 3-2 Material Properties References: [1] Holbrook et al. (1992); Kay et al. (1992) [2] Lange (1997); Ochs and Lange (1999); Guo et al. (2014) [3] Lesher and Spera (2015)

interstitial melts after 80-90% crystallization will approach low-SiO_2 rhyolite melt compositions as well. The expectation is that mixtures of partial melts of granitoid and solidified mafic sills, along with interstitial melts of crystallizing basaltic sills, will contain >70 wt% SiO_2 and are thus classified as rhyolitic. Their subsequent crystallization, after ascent and emplacement, will lead to leucogranitic plutonic bodies, distinct from the largely granodiorite composition (~66 wt% SiO_i, on average) of the eastern Sierra Nevada batholith (e.g., Oliver et al., 1993), which makes up the upper crust under Long Valley.

In addition to the evolved SiO_2 content of the ascending melts, it is also of interest to track their Sr and Nd concentrations and isotopic compositions. This requires that the bulk partition coefficient for these two elements be known for the different parental source rocks, as well as their initial Sr and Nd concentrations and isotopic compositions. A summary of average values of these data for the various parental sources, obtained from the literature, is provided in Table 3-1. These data are currently employed within TIRAMISU to track the Sr concentration and isotopic signature of all melts undergoing transport. (In the near future, the Nd concentration and isotopic signature will also be tracked.)

To model the Sr concentration in partial melts of granitoid and solidified mafic sills, the model equation for equilibrium melting/crystallization is employed:

$$\frac{C_i^{liq}}{C_i^{parent}} = \frac{1}{(F+D_i^{bulk}-FD_i^{bulk})} \tag{2}$$

where C_i^{liq} is the concentration of element *i* in the interstitial liquid, C_i^{parent} is the initial concentration of element *i* in the bulk parent, *F* is the melt fraction, and D_i^{bulk} is the bulk partition coefficient for element *i* (in this case, *i* = Sr) between the partial melt and the wall-rock granitoid or mafic sill. The method for deriving melt fraction information during the numerical simulation and the tracking of Sr concentration in the partial melt is addressed below. Equation

(2) can also be applied to late-stage crystallization of the basaltic sill to track the evolving Sr concentration of the residual melt. Because the bulk D_{Sr} is ~3.2 and ~2 for granitoid and basalt, respectively, Sr behaves compatibly and is not preferentially partitioned into the melt phase. This causes the concentration of Sr in the transported rhyolite melt to be lower than in the original source rocks.

Transport of Rhyolitic Melts

Transport Criteria

The present version of TIRAMISU used two physically motivated criteria to trigger the secondary ascent and emplacement of rhyolite melt. The first criterion is of a temporal nature and is related to volatile transfer from the basaltic sill to the wall rock. In Calogero et al. (2020), we determined that the transfer of volatiles from the cooling sill to the surrounding wall-rock, is expected to occur when the sill center reaches ≥75% crystallization for a basaltic magma with an initial water content of 3 wt% H_2O (the latter is from Jolles, 2020). After 75% crystallization, the residual melt will contain ≥12 wt% H_2O and thus volatile exsolution is expected. Here, it is assumed that once volatile exsolution within the crystallizing sill occurs, segregation of residual melt is enabled by gas-driven filter pressing (e.g., Sisson and Bacon, 1999). In addition, transfer of exsolved volatiles to adjacent wall rock leads to hydrous partial melting conditions (see Calogero et al., 2020, for a detailed discussion). We take a conservative view here and assume volatile release from the sill occurs when the sill center attains at least 80% crystallization. This can occur so long as ambient temperatures remain below about 815ºC, which is the temperature at which basalt will be 80% solidified, using the FT relationship for basalt (cf. Figure 2-1a). This forms the basis of the temporal criterion, which will be reached for every basaltic sill.

The second criterion to trigger a secondary ascent of melt movement is of a spatial nature, and it is motivated by the ubiquitous existence of pre-existing aplite dikes in granitoid crust. These dikes have high-SiO2 rhyolite composition (e.g., Glazner et al., 2008) and during partial melting of granitoid wall rock, they will become 100% melt-filled fractures that additionally draw in partial melt from the surrounding granitoid (e.g., Lange, 2019). Critical lengths (≤40 m) and widths (≥10 cm) for self-propagation of these molten dikes over transport distances of several vertical kms are readily attained. For example, as discussed in Calogero et al. (2020), critical lengths (l_c) are calculated from the relation $l_c = (K_c/[\Delta\rho g])^{2/3}$, where K_c is the fracture toughness (~1 MPa $m^{1/2}$ for granitoid; Gonnerman and Taisne, 2015). Note that the K_c value for granitoid is likely an overestimate in this case because the melt in these fractures will likely flow, outside their melt source region, along the interface between solidified aplite dikes and granitoid wall rock. For a $K_c \leq 1$ MPa $m^{1/2}$ and a $\Delta\rho$ (rock-melt) of ~400 kg/m^3, critical lengths of ≤ 40 m are obtained, which are on the length scale of the partially melted wall-rock margins. Critical widths (w_c) for melt-filled fractures, to ensure transport without solidification, are calculated from the relation given in Petford et al. (1993), $w_c = 1.5(S_m/S_{ff}^2)^{3/4}(\mu kH/\Delta\rho g)^{1/4}$, where H is vertical transport distance (~10 km), k is thermal diffusivity (~8 x 10^{-3} cm^2/s), μ is melt viscosity (~10^5 Pa-s), S_m and S_{ff} are the Stefan numbers, $S_m = L/C_p(T-T_{ff})$ and $S_{ff} = L/C_p(T_m-T_w)$, L is latent heat of solidification, C_p is the specific heat, T_w is the solidus temperature of melt, T_{ff} is the far-field temperature of the crust through which the dike is traversing, and T_m is the temperature of the melt. For T_{ff} values of ~550-650°C, critical widths (for ~10 km of vertical transport) range from ~100-10 cm, and again, are readily attained (i.e., consistent with aplite dike widths observed in granitoid).

The spatial criterion for melt transport is implemented in TIRAMISU to ensure that material boundaries of the secondary sill and the crustal region from which melt is removed are resolvable by our finite-difference solution. Specifically, we require that the cumulative thickness of partial melt in the wall-rock above the basaltic sill to be at least the minimum node spacing (2 meters in these simulations) at any time after the center of the basaltic sill achieves 80% crystallization (i.e., between onset of volatile exsolution and complete solidification). In the simulations presented here, there is partial melting within a 100 m region above a crystallizing basaltic sill (i.e., double the thickness of one emplaced basaltic sill).

In order to calculate the amount of partial melt in the region, we assume melt fraction varies linearly between nodes, which we integrate to determine the amount of partial melt in the crustal column. We express the amount of partial melt in terms of the thickness of the melt if all of the partial melt was extracted from the given depth range (i.e., the volume per lateral dimensions). Considering just two nodes, located at depths x_i and x_{i+1}, with melt fractions F_i and F_{i+1}, respectively, the equivalent thickness of the melt between these nodes is

$$h_i = \frac{m}{2}({x_{i+1}}^2 - {x_i}^2) + b(x_{i+1} - x_i), \quad (3)$$

where m is the slope of the melt fraction between the nodes,

$$m = \frac{F_{i+1} - F_i}{x_{i+1} - x_i}, \quad (4)$$

and b is the intercept of the interpolant related to F_{i+1} and x_{i+1}. The total thickness of the melt, H, in the 100 m region above the basaltic sill is then the sum of h_i over the nodes in that region. In order to pass the spatial criteria and trigger the removal of partial melt from this region, we assume that H must be greater than, or equal to, the minimum spatial resolution allowed in the finite difference mesh. For the simulations in which secondary melt movement is allowed, we use a minimum node spacing of 2 m, and hence $H \geq 2$ m in order for a transport of rhyolite melt

to be triggered. For the simulation presented in this study, for 60 primary basaltic sills, both criteria were passed 50 times. All failed cases had $H < 2$ m due to the new sill having been injected within previously compositionally reworked portions of the crust, which have higher solidus temperatures than un-touched granitoid.

Building the Transportable Melt Package

When the two criteria for secondary melt movement are met in TIRAMISU, we extract the residual melt within the basaltic sill, along with the partial melt above the sill, to a new sill higher in the crustal column. Furthermore, if there is melt present at the base of the basaltic sill, and wall-rock partial melts exist within a similar, 100 m thick region below the sill, we assume permeability such that these wall-rock partial melts are also included in the transported melt. The evacuated region is composed of the basaltic sill along with the 100 m above and, potentially, below the sill. The evacuated regions may also include previously solidified mafic sills if the most recent solidifying sill was placed near an old sill. The full package of the melt that is extracted from the evacuated region is composed of residual melt from the sill (low-silica rhyolite), and partial melt from the surrounding wall rock (broadly rhyolitic, dependent on the local lithology).

To determine the emplacement temperature for the secondary sill, we take the average temperature, weighted by the proportion of contributed partial melt, within the region the melt is evacuating:

$$T_{new} = \sum_1^q T_k \frac{f_k}{f_{total}}, \quad (5)$$

where f_k is the proportion of partial melt between each node pair:

$$f_k = \frac{h_k}{x_{i+1} - x_i}, \quad (6)$$

for k ∈ [1,q] node segments spanning the evacuated region. T_k is the temperature at each node, and f_{total} is the sum of all f_k. We then apply a linear FT relationship for the new sill, where the liquidus is the ascent temperature, and the solidus is the same as that for granitoid (cf. Figure 2-1c).

Strontium Concentration and Isotopic Signature of Transported Melts

TIRAMISU tracks element concentration in the transported rhyolite melts. Given the eruptions of low-Sr rhyolites in the same region as high-Sr basalts from LV, and the availability of partitioning data for Sr from basalt and granitoid (Table 3-1), it was chosen as the first element explored in this study. We use Equation (2) to determine the proportion of Sr contributed to the partial melt between each node pair within the evacuated region. Sr concentration is then determined in the new sill with a weighted approach similar to the temperature, but considers contributions from the two sources separately:

$$Sr_g = \sum_1^q Sr_{g,k} \frac{f_{g,k}}{f_{g,total}}, \tag{7a}$$

$$Sr_b = \sum_1^q Sr_{b,k} \frac{f_{b,k}}{f_{b,total}}, \tag{7b}$$

$$Sr_{new} = \frac{H_g}{H_{new}}\left(Sr_g\right) + \frac{H_b}{H_{new}}\left(Sr_b\right), \tag{8}$$

where H_g and H_b are the thickness contributions from granitoid and basalt respectively, and their sum is H_{new}. Sr_g and Sr_b are the proportions of Sr contributed from each material, and the calculations are weighted by the proportions of partial melt, f_g and f_b, from each material separately.

We assume a Sr isotopic ratio ($^{87}Sr/^{86}Sr$) of 0.706 for rhyolite derived from basalt sills, and 0.708 for rhyolite extracted from the granitoid wall rock (Table 3-1; cf. Figure 3-1). We then determine the isotopic ratio of Sr in the new sill by computing:

$$Sr_{isotopic} = \frac{Sr_g H_g}{Sr_{new} H_{new}} * 0.708 + \frac{Sr_b H_b}{Sr_{new} H_{new}} * 0.706. \quad (9)$$

Lastly, we assign the material properties for the new sill. For this process, we again are mindful of the proportions contributed to the new melt from granitoid and mafic sources. As part of the generalization incorporated in TIRAMISU, the material properties, may which differ significantly depending on the source, have their values calculated based on the proportion of melt contributed by each source. In this study, we only expect variability in the densities of the different rhyolite contributions (Table 3-2).

Updating the Evacuated Region

When the secondary melt is extracted, the evacuated region thins. New material boundaries are added at the highest and lowest depths in the crustal column from which melt is being extracted from, if there are no material boundaries at those locations already. Each material segment of the evacuated region is then compressed by the thickness of melt being removed from that portion, and we move every deeper material border up by that thickness. For example, a 40 m thick region with 10 meters of melt removed total would be reduced to a 30 m segment, and every deeper material border would be adjusted upwards by 10 meters.

To update FT relationships, we average temperature across each portion of the evacuated region that is of a constant material type and assign these as the new solidus temperatures. We then re-calculate the melt fractions, slopes, and intercepts for subsequent inflection points. Because the bulk composition of rocks in the evacuated region changes when the melt is

extracted, we ascribe updated material properties for each region, relative to an assumed average 20% partial melt from granitoid and average 5% partial melt from basaltic sources, as given in Table 3-2.

Extraction of melt from the evacuated region results in cooling due to the loss the of heat (i.e., enthalpy) in the mass of transported rhyolite. We calculate the amount that the temperature drops due to the evacuation of melt by dividing an enthalpy of 10^5 J/(kg*K) by the specific heat capacity of the evacuated material. This results in an immediate average ~80ºC temperature drop over the evacuated region.

Secondary Sill Emplacement

In TIRAMISU, when melt is extracted from the evacuated region associated with the basaltic sill, that melt is instantaneously moved to a new, secondary sill, which is emplaced randomly within an initial depth range of 18–20 km. As with the region in which basaltic sills are emplaced, the base of the region evolves as secondary sills continue to be emplaced. The material properties of the new sills are determined from evacuated rhyolitic melt, as described above.

In order to maintain the integrity of thermal diffusion along the whole crustal column beyond the transport event, we redistribute the finite difference nodes to include two high resolution regions covering both the primary and secondary sills. High spatial resolution is maintained in and around the primary basaltic sill, over the same thickness as during primary emplacement, even though the evacuated region itself has been shortened. Additionally, high spatial resolution at the minimum node spacing is enforced in and around the new secondary rhyolitic sill, the extent of which is variable based upon that sill's thickness, but rounded to the nearest meter as our lowest node spacing in the presented results is 2 meters. The center point is

then identified, between the two sills, and half of the nodes available are assigned above and half below the center point, as though they were two independent primary sill emplacement events, with the nodes spreading out, roughly geometrically away from each sill. As discussed above, the spreading of the nodes is not perfectly geometric, as we ensure that every material boundary has a node upon it. If during the redistribution of nodes, two nodes overlap or are spaced less than the minimum prescribed spacing (discounting material boundaries that are closer than the minimum), the model domain is increased by five times the specified minimum node spacing, and one of the (near) overlapping nodes is moved to the base of the domain. Note that even though there is no remaining melt in the primary sill location, the sill still has residual heat, and thus the curvature of the temperature field is potentially still large. We then proceed to compute the solidification of the secondary sill, along with the evolution of temperatures throughout the entire domain, until a new basaltic sill is emplaced within the lower crust.

Results

We explore three aspects pertinent to the Long Valley magmatic system. First, we discuss the effect of the secondary advection of melts within the crust on the crustal geothermal profile. We demonstrate that the secondary advection of melts results in a cooler lower crust, with elevated temperatures throughout the upper crust, as expected. Second, we examine the thickness of rhyolite melt generated from each lithology, cumulatively over time, and discuss the role that both partial melt of granitoid (and solidified mafic) wall rock and interstitial melt from crystallizing basaltic sills play in producing more rhyolitic melt than either end member could alone. Thirdly, we consider the compositional evolution through the Sr concentration and isotopic ratio in rhyolitic melts built from granitoid and basaltic sources. We demonstrate the

need for multiple stages of rhyolite segregation and transport events to align with the extreme geochemical signatures of the Long Valley rhyolites.

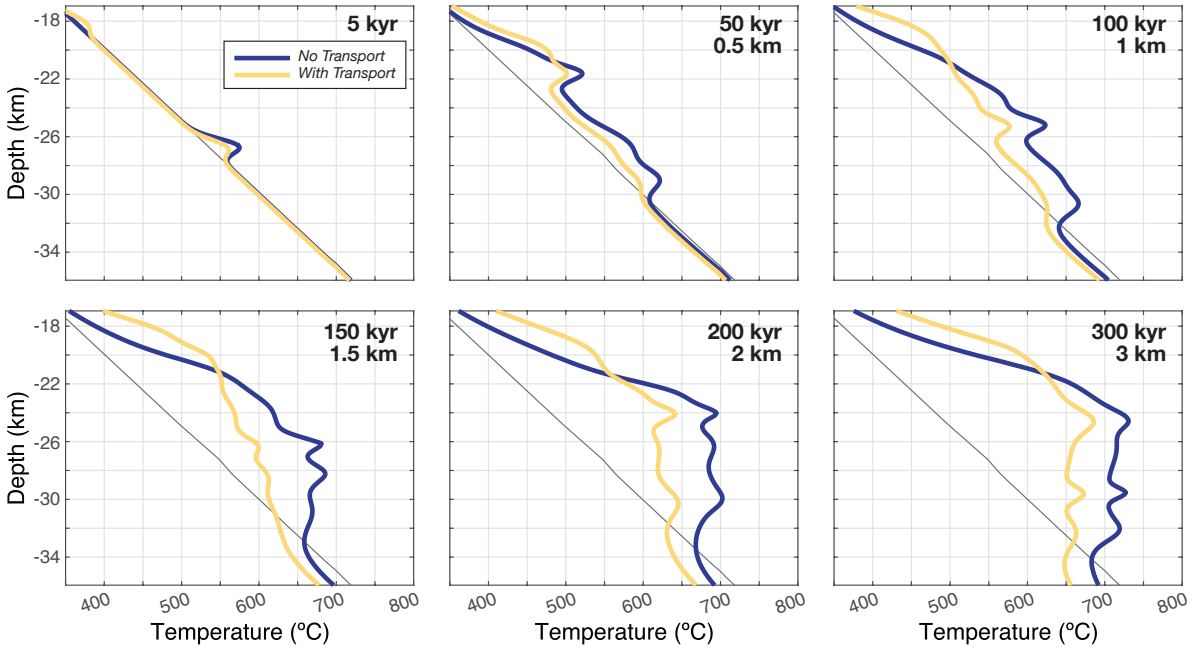

Figure 3-2 Plots illustrating the evolving thermal profile through the crustal column as a function of time (i.e., cumulative thickness of basalt emplacement), for a basalt emplacement rate of 50 m/5 kyr; basaltic sills are emplaced randomly in an initial depth interval of 25-30 km. The blue line shows the thermal profile when no transport of secondary (rhyolitic) melts are permitted, whereas the yellow line shows the change in the thermal profile due to the removal of secondary melt from their source regions and subsequent random emplacement between an initial 18-20 km depth interval. Note the cooling and heating effect, respectively, due the removal and emplacement of secondary (rhyolitic melts).

The effect of secondary melt advection on the crustal thermal profile

We ran two simulations, both of which were driven by identical histories of basaltic sill emplacements within an initial 20-30 km interval. In the first simulation there was no secondary melt transport. This simulation follows previously published simulations of randomized magma emplacement (e.g., Annen et al., 2006; Leeman et al., 2008; Karakas & Dufek, 2015; Calogero et al., 2020). In the second simulation, we allow for secondary advection of partial and residual

melt that exists within a region centered around the sill center, assuming that the criteria for secondary melt movement are met. These secondary sills are instantaneously emplaced within an initial 18-20 km depth interval. The petrology of the new sill and the evacuated region (i.e., the lower crustal region in which the secondary melts derive from, including the primary sill, adjacent crust, and potentially previously emplaced and solidified sills) are updated accordingly via relative adjustments made to the material properties. In comparing the two simulations, our main focus was to evaluate the consequence of the second stage of melt migration on the thermal profile of the crust.

In Figure 3-2, we show six snapshots of the thermal profile at times 5, 50, 100, 150, 200, and 300 kyr. As we emplace basaltic sills into the lower crust every 5 kyr, the times in Figure 3-2 correspond to 5 kyr of cooling after the 1st, 10th, 20th, 30th, 40th, and 60th basaltic sill is emplaced, respectively. In both simulations, the geotherms at 5 kyr demonstrate the heating of the lower crust in the region where the single basaltic sill was emplaced (~26.5 km). However, in the simulation with secondary advection, the temperatures near the basaltic sill are lower due to cooling in the evacuated region, and the associated heating where the secondary sill was emplaced (~18.25 km). As that secondary sill was emplaced in the upper crust at about 0.098 kyr, there has been ~4.9 kyr of diffusion of heat from that sill in these geotherms.

In later simulation times, as more basaltic sills invade the lower crust, there is an expanded region of crust in which basaltic sills are emplaced in both simulations (at 200 kyr basaltic sills are emplaced from ~20–32 km). Due to this expanding region in which basaltic sills are emplaced, along with the diffusion of heat from those sills, both simulations result in elevated temperatures in a broad region of the lower crust; however, the lower crustal temperatures are cooler in the simulation in which secondary melt advection is considered, while

they were hotter in the upper crust. At 200 kyr, lower crustal temperatures reach ~675ºC in the simulation without secondary melt advection, while they are ~625ºC in the simulation with advection. These elevated lower crustal temperatures result in significant deviation of the geothermal gradient from the initially assumed 20ºC/km (Figure 3-2).

In the simulation with secondary advection, the upper crust or lower crust are hotter or cooler, respectively, than the simulation without the secondary advection (Figure 3-2). The depth at which the geotherms in the two simulations is the same is around 21 km, which we refer to as the cross-over depth, and which stays more-or-less static throughout the simulation. Above the cross-over depth, the temperatures are hotter in the simulation with secondary sills, whereas the crust is cooler below the cross-over depth, compared to simulations with only primary basaltic sills. The cross-over depth of ~21 km in this simulation is an artifact of the random realization of emplaced sills used in the simulations, as there were no primary sills injected above 21 km after the 17th basaltic sill was emplaced at 80 kyr. The cross-over depth will vary with different realizations of depths where basaltic sills are emplaced.

A key takeaway is the fact that the difference in temperatures between the two simulations is up to 60ºC. The maximum difference in temperatures is built up by 200 kyr, with an associated 2 km of emplaced basalt, and then is maintained for the remainder of the simulation. The implication is that the temperature of the lower crust is reaching a quasi-steady-state when the secondary advection is considered, in contrast to a longer period of increasing lower crustal temperatures when only the primary basalt emplacement is considered. In this quasi-steady-state, the flux of heat due to the invasion of basaltic sills is being roughly balanced by the net effect of the diffusion of that heat out of the lower crust along with the movement of the upper crust along with the secondary advected melt. To determine whether the evolution

towards a quasi-steady-state is a manifestation of these particular sill emplacement histories, or is a universal feature, would require more and longer simulations, which we save for future study. Finally, even though the incorporation of a secondary stage of advection of melt results in a hotter upper crust, the average temperature of the entire crust is cooler than when the secondary melt migration is ignored.

Thickness of advected rhyolite melt relative to thickness of emplaced basalt

One of the over-riding motivations of this study is to determine how much rhyolite melt can be extracted from the crustal column relative to the amount of basalt emplaced into the granitoid crust. For the basalt emplacement rate used in this study (50 m per 5 kyr) and the initial interval for its emplacement (20–30 km), the amount of rhyolite that met the advection criteria is illustrated in Figure 3-3a, where we show the cumulative thickness of the advected rhyolite melt, and the thickness proportions coming out of either granitoid, which includes both untouched and reworked granitoid, or basalt, which includes residual melt from the crystallizing sill and partial melt of previously emplaced mafic sills scattered along the crustal column. After 1, 2, and 3 km of basalt are emplaced, approximately 0.5, 1.1 and 1.7 km of rhyolite are advected, respectively.

The proportions of advected rhyolite and its source contributions are plotted relative to the cumulative basalt thickness in Figure 3-3b. Here, it is seen that the relative amount of rhyolite that is transported to secondary sills ranges from ~50-60% of the basalt thickness, with a close to 1:2 ratio of rhyolite to basalt. We attribute the oscillations in the thickness in the granitoid contribution to the greater variance of initial ambient temperatures early in the simulation. Thefirst few sills randomly intruded ambient temperatures between 400-600ºC (cf.

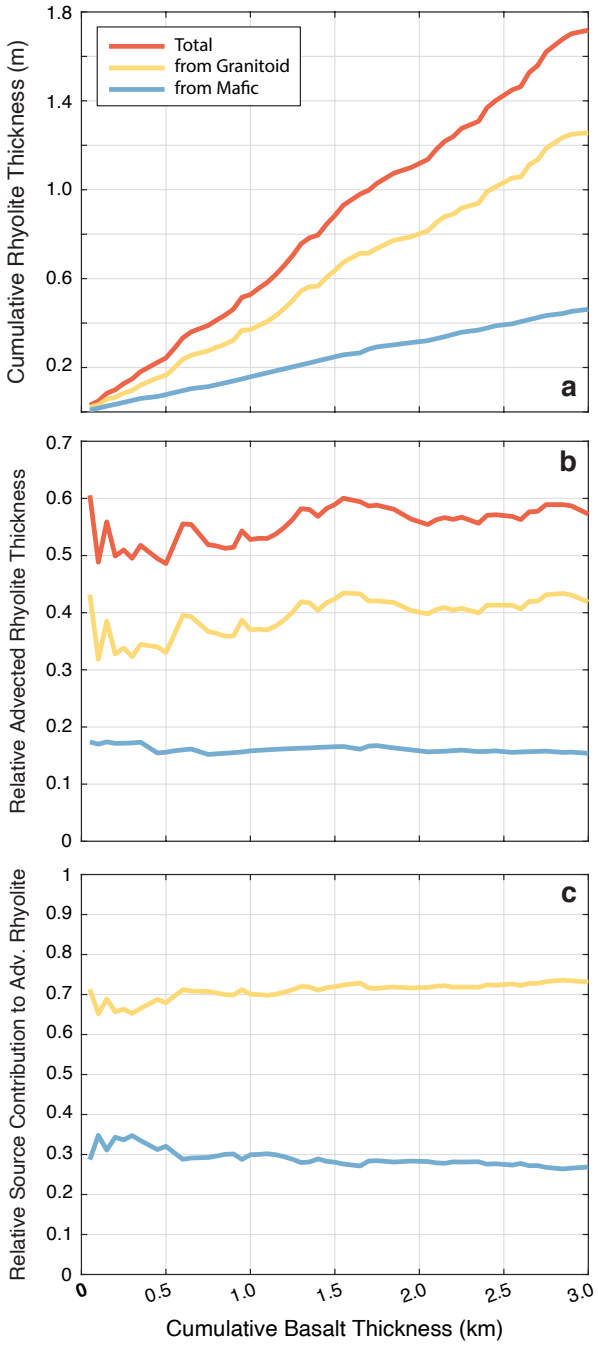

Figure 3-3. (a) Plot of cumulative thickness of rhyolite melt (red line), which passes criteria for transport and emplacement higher in the crustal column, as a function of cumulative thickness of basalt emplaced in the deeper crust. After 3 km of basalt is emplaced, approximately 1.7 km of rhyolite is produced and transported. Contributions to the total thickness of rhyolite derived from granitoid (yellow line) and basalt (red line) are also shown. (b) Proportion of transported rhyolite (~50-60%) relative to thickness of basalt emplaced is shown. Rhyolite derived from granitoid wall rock is ~40% of basalt thickness, whereas rhyolite derived from basalt is ~15% of its emplaced thickness. (c) The proportion of transported rhyolite that is derived from granitoid is ~70% (yellow line), whereas that derived from basalt is ~30% (blue line).

Figure 3-2), but by 150 kyr, after 1.5 km of basalt has been emplaced, any new sill is emplaced in the crust with ambient temperatures between about 540–620ºC.

Another outstanding question is what proportion of the advected rhyolite is derived from pre-existing granitoid versus basaltic sills. The answer to this question is shown in Figure 3-3c, where ~70% of all advective rhyolitic melt is derived from granitoid and ~30% is from basalt. There appears to be only a slight increase in the amount of rhyolite derived from granitoid (about 68–72%) as a function increasing ambient temperature. The conclusion is that although basalt is an important source of advected rhyolite melt, the granitoid source is dominant. This raises the question of whether or not the Sr (and Nd) isotopic composition of advected rhyolite is also dominated by the granitoid source, which appears to counter the analyzed isotopic signature of erupted Long Valley rhyolites (cf. Figure 3-1). In the following section, we evaluate the evolution of the Sr concentration and isotopic composition of the advected rhyolite over time.

The Sr composition of the advected rhyolite melt

In Equation (2), there are three key parameters that control the concentration of Sr in the transported rhyolite melt: (1) the Sr concentration in the source rock (granitoid vs. basalt), (2) the bulk partition coefficient for Sr (bulk D_{Sr}) between the rhyolite melt and source rock, and (3) melt fraction. We show that the average Sr concentration in the advected rhyolite melt is ~380 ppm (Figure 3-4a), and the majority ranges between 250 and 440 ppm. This demonstrates the first stage in what must be a multi-stage process of additional partial melting events to drive down the Sr concentration of evolved rhyolite melts to eventually reflect those historically erupting from LV. An overview of these additional processes is provided in the Discussion section below.

Rhyolite melt extracted from granitoid is consistently lower in Sr compared to that derived from basalt, owing to the fact that the initial Sr concentration is lower and the bulk D_{Sr} is higher for the granitoid relative to the basalt. We find that the relative proportion of Sr in the rhyolite derived from basalt consistently exceeds the relative amount of rhyolite melt derived from basalt, which is illustrated in Figure 3-4d. Hence although only ~30% of the advected rhyolite is derived from basalt (Figure 3-3c), up to ~60% of the Sr concentration in the rhyolite is sourced from basalt, which has major implications for the Sr isotopic composition of the rhyolite melt.

In addition to Sr concentration, we also calculate the isotopic concentration of Sr in the rhyolitic melts. A histogram of these results is provided in Figure 3-4b, and we find an average $^{87}Sr/^{86}Sr$ value of 0.7068, which falls between the initial values for granitoid wall rock (0.708) and Long Valley basalts (0.706). In Figure 3-4c plot the Sr isotopic values against the cumulative basalt thickness. The scatter here demonstrates the various conflicting controls at play. During the first few basalt sill emplacements, the geothermal gradient is still relatively linear (Figure 3-2), and the shallow transport events had a higher ratio of basalt to granitoid rhyolite contribution ratio, resulting in lower isotopic ratios (<0.7066), compared to the deeper events, which were emplaced at a higher ambient temperature. As more basalt sills are emplaced, the thermal profile at depth grows hotter and the mixed lithology develops in tandem. The key point illustrated here is that increasing complexity diffuses the strength of either control (ambient temperature vs. local lithology) on the isotopic composition of the rhyolite melt.

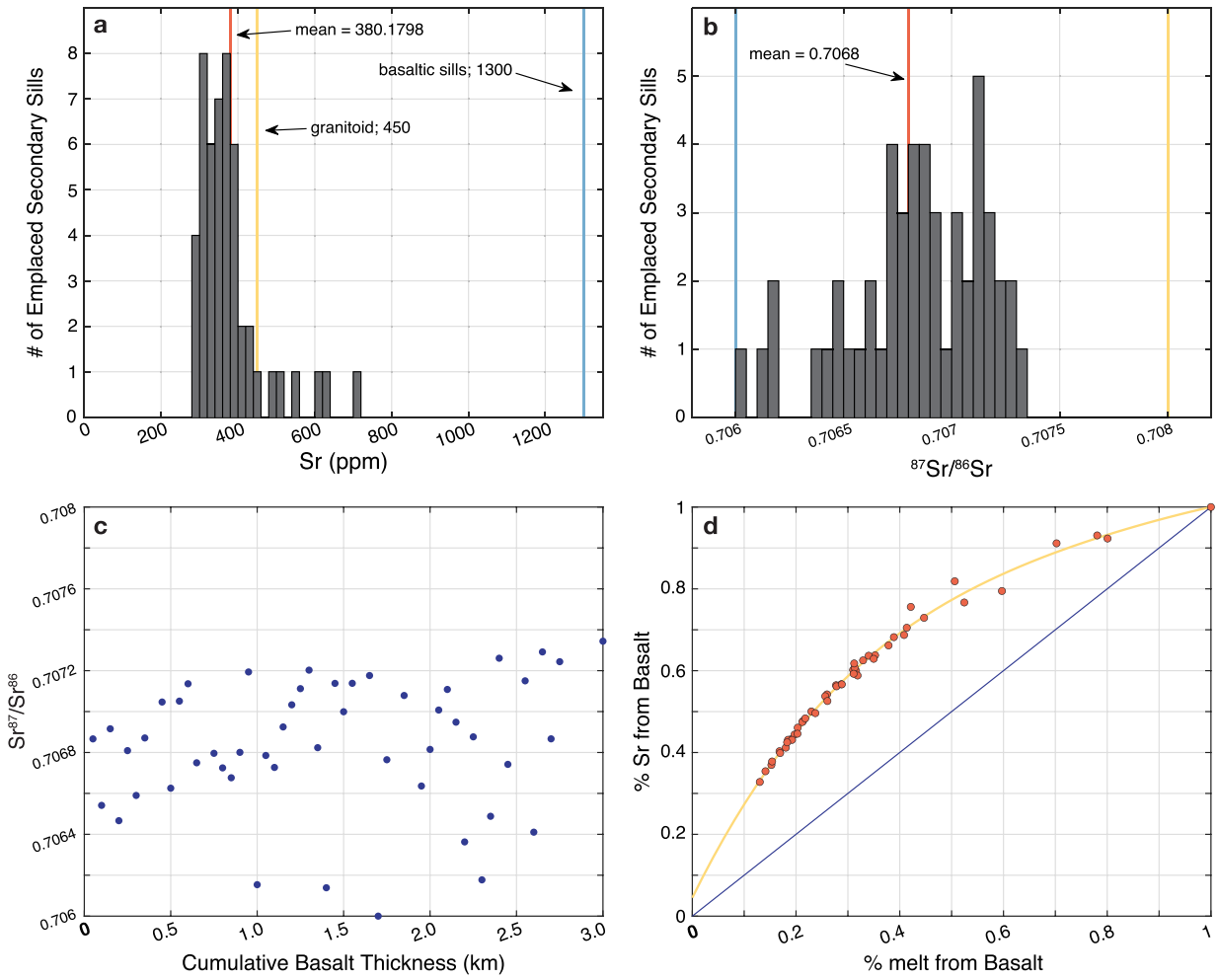

Figure 3-4. (a) Histogram showing the Sr concentration (ppm) of emplaced secondary sills (rhyolite melts) in the simulation after 3 km of basalt emplaced (depicted by the yellow line in Figure 3-2). The mean Sr content is 380 ppm (most range between 420 and 240 ppm), which is significantly lower than the basalt Sr concentration (1300 ppm) and slightly below the average Sierran granitoid Sr concentration (450 ppm). This result illustrates the shift to lower Sr contents in secondary (rhyolitic) melts compared to source rocks, but still higher than those in erupted Long Valley rhyolites (<30 ppm; see text). (b) Histogram showing the Sr isotopic composition of emplaced secondary sills (rhyolite melts) in the simulation after 3 km of basalt emplaced. The mean Sr isotopic ratio is 0.7068, which is broadly intermediate between the average ratios for granitoid and basalt endmembers, but considerable variation is shown. (c) Plot of Sr isotopic ratio in emplaced secondary sills as a function of cumulate basalt thickness emplaced. The results show that there is no trend in the scatter of Sr isotopic values with time (i.e., the amount of basalt emplaced). (d) Plot illustrating the relative amount (%) of Sr in emplaced secondary sills (rhyolite melt) that is derived from basalt (vs. granitoid) relative to the total amount (%) of rhyolite derived from basalt (vs. granitoid). The thin grey line is the 1:1 line. The results show that the Sr content in transported rhyolite is disproportionately derived from the basaltic source. When the overall amount of transported rhyolite is ~30% derived from basalt (see Fig. 3-3c), the amount of Sr in the transported rhyolite is ~60% derived from basalt.

Discussion

Factors controlling the crustal-scale thermal profile

One of the primary questions posed in this study was how does the ascent of rhyolite melt, which forms in response to the influx of basalt into the crust, change crustal-scale thermal profiles? An anticipated and verified effect is that it leads to relative cooling of the rhyolite source region and relative heating in the region where rhyolite is emplaced. For the specific input parameters (e.g., basalt emplacement rate, depth interval of basalt emplacement, etc.) used in this study, the magnitude of the relative cooling and heating in each region is ~60° C in both cases (Figure 3-2). To further evaluate factors that control crustal-scale thermal profiles, when the transport of rhyolitic melts is included, it is necessary to explore a wide variety of basalt emplacement rates, different depth intervals for basalt (and rhyolite) emplacements, and longer time durations. This will be the focus of near-term future work.

A remaining question is to what extent will the temperature of the lower crustal column continually warm with increasing cumulative basalt emplacement? If the lower crust does continue to warm, will the rate of warming be moderated by the growing formation and removal of rhyolite melt? Here, we employed only a single set of input parameters in our numerical simulation. In the near future, we intend to vary these input parameters to systematically explore their relative effect on crustal-scale thermal profiles. This will allow us to address whether the temperature difference between the thermal profiles in the deep crust evolves, either with or without secondary melt transport, as a function of the driving parameters. Considering a suite of basalt emplacement histories will allow us to determine if the ~60º difference seen here is unique to these simulations, and if not, to what level the various input parameters control the maximum difference in temperatures when secondary transport is or is not considered. For instance, is the

difference in temperatures predominantly controlled by FT relations of the rhyolite source rocks, heat capacity and enthalpy values, and/or basalt emplacement rates?

Controls on the amount of rhyolite formed and transported relative to basalt input

In this study, we show that the amount of transportable rhyolite formed by the influx of basalt into the deep crust was approximately 50–60% of the thickness of basalt emplaced. This is a notably high percentage of evolved melt per unit thickness of basalt emplaced, and it reflects the efficiency of rhyolitic melt production sourced from both partial melts of wall rock and residual melts from basaltic sills. The involvement of only one parental source, in the absence of the other, leads to far lower amounts of rhyolite formed. In the end-member case where only basalt differentiation is permitted without the involvement of any partial melts of granitoid wall rock, our simulations show that only about 17% of the thickness of basalt would be available to migrate to the upper-crust as rhyolite (Figure 3-3b). After ~3 km of basalt emplacement, < 0.5 km of rhyolite would have been emplaced at higher crustal levels (Figure 3-3a). This underscores the enhanced fertility of the crustal column, in terms of rhyolite production, when basalt invades granitoid rather than mafic crust.

In the alternative end-member case, where only the heating of pre-existing granitoid crust is permitted with no contribution of melt from basalt, there would also be a significant reduction in the production of rhyolite melt. If exsolved water is permitted to be transferred from basalt to adjacent wall rock, we show that amount of rhyolite formed and transported would be ~40% of the thickness of basalt input into the crust (~1.2 km rhyolite per 3 km of basalt, Figure 3-3). However, in the absence of any water derived from basalt, the granitoid wall rock (where its only source of water is biotite and hornblende; ~0.6 wt% H_2O in the bulk rock) is notably more

refractory. From the FT curves in Calogero et al. (2020; cf. Figure 2-1), melt fractions in fluid-absent granitoid are approximately 25% lower than those in cases where ~2 wt% H_2O is added to granitoid from exsolved water of adjacent basaltic sills. Therefore, with no material mass from the basalt (including water) involved, the amount of rhyolite that would form by heating the granitoid crust, would be only ~10% of the thickness of basalt emplaced (i.e., ~0.3 km of rhyolite transported after 3 km of basalt is emplaced).

These two end-member cases underscore the central importance of both sources of rhyolitic melt, from the granitoid wall-rock and the solidifying basaltic sill. Moreover, the exsolved water from the basaltic sills is critical in controlling the amount of rhyolite that forms, and can be transported to the shallow crust. In the case of the Long Valley volcanic system, which has produced >800 km^3 of rhyolite over the last 2.2 Myr (Hildreth, 2004), it is noteworthy that the crustal column beneath Long Valley contains an unusual thickness of granitoid that extends down to 32 km depth (due to a prolonged history of Mesozoic subduction; e.g., Fliedner et al., 2000). It is also significant that the Long Valley basalts contain high water contents (3-6 wt%; Jolles, 2020), a reflection of their source from subduction-modified lithosphere (Cousens, 1996). Both of these unique features of the Long Valley geological setting clearly played a key role in enabling the production of voluminous rhyolite in this region.

Tracking the evolution of Sr (and Nd) composition in rhyolite: evidence of multiple partial melting events to form the Long Valley rhyolites

In this study, one of the key compositional parameters that is tracked in the rhyolite melts is the Sr concentration and isotopic signature. Our results show that the average Sr concentration in about 1.7 km of rhyolite emplaced in the middle crust is on average 380 ppm and has an

isotopic signature on average of 0.7068, which is intermediate between the endmember values assigned to the granitoid (0.708) and basalt (0.706). The Sr concentration is lower than that assigned to the granitoid (450 ppm) and basalt (1300 ppm), and it represents a first-generation of rhyolite formation. More than one partial melting event is needed to drive Sr concentrations down to the levels seen in the high-SiO_2 rhyolite from Long Valley (<30 ppm; Halliday et al., 1984, 1989).

At least two factors will control the evolving composition of further generations of rhyolitic melts, driven by the continued influx of basaltic melts into the crustal column. First, if the initial set of rhyolitic melts (secondary melts formed by the primary influx of basalt into the crust) solidify to form the granitoid wall rock into which new basaltic sills are emplaced, subsequent partial melts will reflect this change in granitoid composition. Second, it is possible that the composition of the basaltic influx may also change with time. The younger suite of Long Valley basalts (i.e., erupted post-caldera; Cousens, 1996) are notably lower in Sr concentration (~550 vs ~1300 ppm) and Sr isotopic signature (0.705 vs. 0.706) than the older Long Valley basalts (Table 3-1). The effect of these expected changes to the composition of granitoid wall rock and newly emplaced basaltic sills on the composition of second-generation rhyolitic melts are broadly evaluated utilizing a simplified set of calculations.

We apply Equation (2) to different proportions of granitoid to basalt, assuming a constant melt fraction of 0.2 for to granitoid and 0.05 for basalt. The initial Sr concentration of the granitoid and basalt are taken as 450 and 1300 ppm, respectively. The results are shown in Figure 3-5a-c, where the % Sr in rhyolite melt derived from basalt, the overall Sr concentration in rhyolite, and the overall Sr isotopic signature in rhyolite, are plotted as a function of % rhyolite melt derived from basalt. When approximately 30% of the rhyolite melt is derived from

basalt (and the remainder from granitoid), chosen to mirror the results from this study in Figure 3-3c, approximately 64% of the Sr in the rhyolite melt is derived from basaltic sources. This leads to a Sr concentration in the combined rhyolitic melt of 313 ppm and an Sr isotopic signature of 0.7067. This outcome is broadly similar, though different in detail, to that found in the more rigorous approach taken in this study, and it suggests that these simplified calculations are instructive and can be used to guide input parameters for future numerical simulations.

In a second set of simplified calculations, we explore the effect of using the first-generation of transported rhyolite as the granitoid wall rock and the younger Long Valley basalts as the basaltic influx, on the Sr composition of second-generation rhyolites. In this case, we apply a constant melt fraction of 0.3 to the granitoid (to reflect its change in composition) and 0.05 to basalt. When the relevant Sr concentrations, isotopic signatures and bulk partition coefficients are employed, the results indicate that rhyolite melts, if proportioned in the same way as first generation (~70% from granitoid and ~30% from basalt; Figure 3-4c), will contain ~171 ppm Sr and have an isotopic signature of ~0.7060 (Figure 3-5d-f). If the older Long Valley basalts are employed, then the resulting rhyolitic melt (~70% from granitoid and ~30% from basalt) will contain ~287 ppm Sr and have an isotopic signature of ~0.7062. These results broadly illustrate the impact that the evolving compositions of both the wall-rock granitoid and basaltic influx will have on the composition of second- and third-generation rhyolitic melts, and they underscore the need explore these compositional changes in future numerical simulations.

A second question that can be addressed with these simplified calculations is how does the Nd composition (concentration and isotopic signature) of rhyolitic melts evolve in parallel with the Sr composition? In this case, the Nd concentrations, isotopic signatures and bulk partition coefficients from Table 3-1 are employed, and input into Equation (2), as done for Sr.

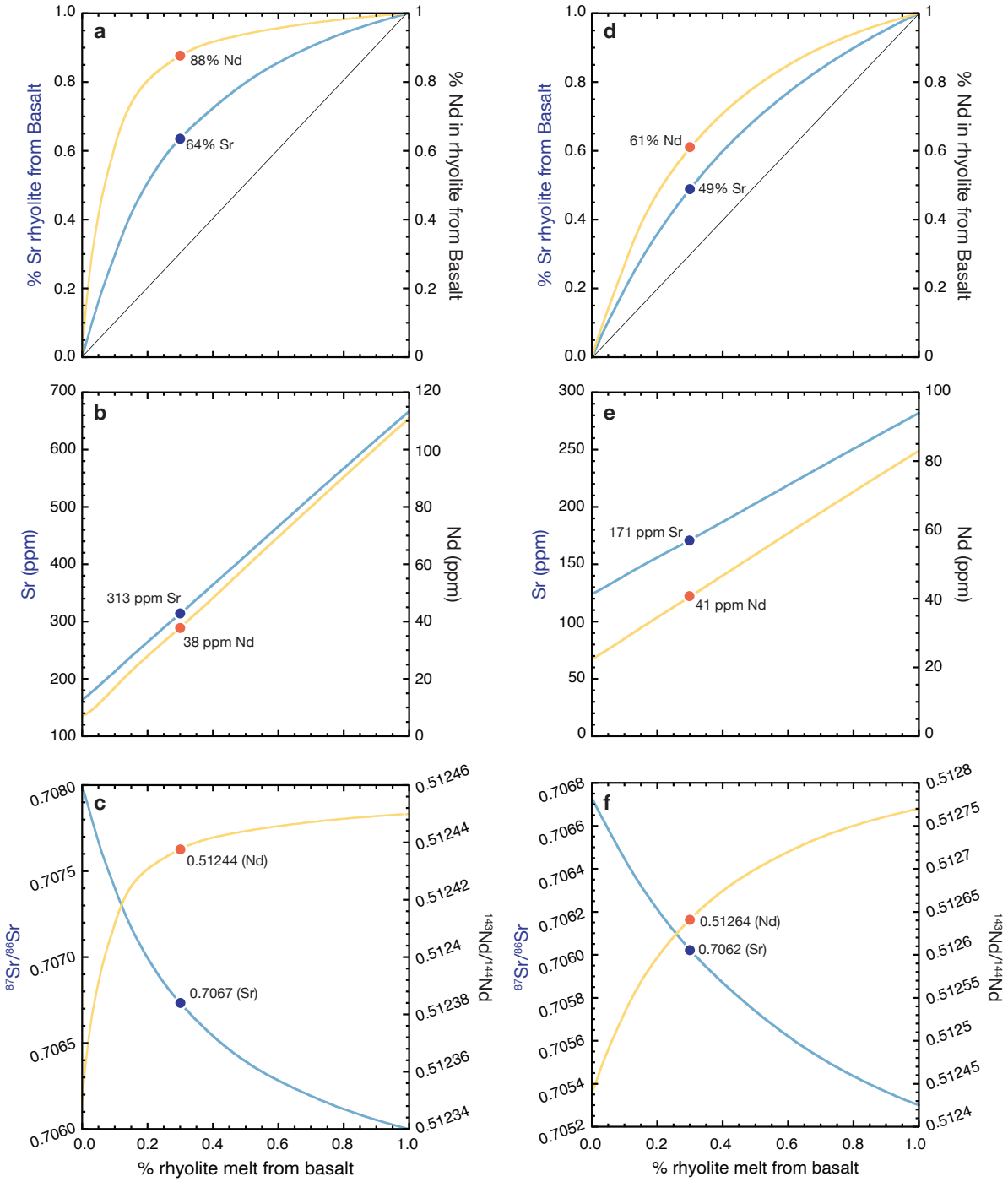

Figure 3-5. Simplified calculations, using Equation 2 and compositional data from Table 3-1, illustrating the evolving concentration and isotopic signature of Sr (blue line) and Nd (yellow line), in both first-generation rhyolite melt (i.e., secondary sills) shown in (a), (b) and (c) and second-generation rhyolite melt shown in (d), (e) and (f). For first-generation melts, the data for average granitoid and older Long Valley basalt (Table 3-1) is employed (see text for details). For second-generation melts, the first-generation rhyolite melt composition (when 30% is derived from basalt; see large circle on colored lines) is used for leucogranite wall rock and the younger Long Valley basalt is used for basalt influx. (a) Calculated % Sr (blue line) and % Nd (yellow line) in first-generation rhyolite melt as function of % rhyolite melt derived from older Long Valley basalt; (b) Same as (a) for calculated Sr and Nd

concentrations; (c) Same as (a) for calculated Sr and Nd isotopic signatures. (d) Calculated % Sr (blue line) and % Nd (yellow line) in second-generation rhyolite melt as function of % melt derived from younger Long Valley basalt; (e) Same as (d) for calculated Sr and Nd concentrations; (f) Same as (d) for calculated Sr and Nd isotopic signatures. The results illustrate how Sr and Nd concentrations and isotopic signatures evolve between first- and second-generation rhyolitic melts, and they will be used to guide future numerical simulations of multiple basalt emplacement events at progressively shallower crustal depths.

The results are shown in Figures 3-5, and the most important finding is that the Nd in rhyolitic melts will largely be derived from basaltic inputs, irrespective of relative proportions of melt derived from granitoid. This pattern is caused by the highly compatible behavior of Nd in titanite-bearing granodiorite relative to rhyolite melt (Prowatke & Klemme, 2006) and the incompatible behavior of Nd in basaltic crystalline assemblages relative to interstitial melt (Table 3-1). For granodiorites (dacitic in composition), the presence of titanite ($CaTiSiO_5$) contributes strongly to the compatible behavior of Nd during partial melting, whereas for leucogranites (where sphene is absent and the primary repository for Nd is allanite) the bulk partition coefficient for Nd is lower (though still compatible; see Table 3-1 for values and references). The purpose here is to point out these differences and to obtain broad constraints on the expected behavior of Nd (in parallel to that of Sr) during the formation of rhyolite driven by the influx of basalt into the crust.

The first generation of rhyolitic melt to form (70% from granodiorite and 30% from older Long Valley basalts) will contain ~38 ppm Nd (intermediate between the granitoid and basalt Nd concentrations) and have a Nd isotopic composition (0.51244) that is dominated by the basaltic source (~13% from granitoid and ~87% from basalt; Figure 3-5a-c). For a second generation of rhyolite, formed by younger Long Valley basalt injected within leucogranite (i.e., first-generation rhyolite), the Nd concentration is slightly higher (~39 ppm) and its Nd composition is again strongly dominated by the basaltic source. It is also possible that a mixture of older and younger Long Valley basalts may be emplaced into the crust during the formation of second- and third-generation rhyolitic melts. The key point here is that it is possible to track changes in the

Nd composition (concentration and isotopic signature) of first-, second- and third-generation rhyolitic melts in future versions of our numerical model. Through the employment of more compositional parameters (e.g., both Sr and Nd), and continued tracking to identify reasonable portions of physical source contributions, the constraints tighten on plausible scenarios for how the influx of basalt into the crustal column beneath the Long Valley caldera drove the formation of such voluminous, yet highly differentiated, rhyolites.

Summary of planned model development going forward

In TIRAMISU, both the temporal and spatial criteria for evacuation of partial and residual melt, while motivated by experiments and previous modeling, are admittedly short-cuts to modeling of a secondary stage of melt migration. Additionally, the exact specifics of the two criteria will result in a change in evolution of temperature and composition over the crust. For instance, allowing a secondary melt migration earlier in the solidification of the basaltic sill, say at the time that a basaltic sill reaches 75% crystallization instead of 80%, could allow for more melt in the wall rock to be captured as well, particularly at cooler ambient conditions (cf. Figure 2-14). On the other hand, requiring more solidification of the basaltic sill before a secondary melt movement was permitted would likely result in less melt, both from the wall rock and the basaltic sill. The second criterion is motivated by issues of spatial resolution, requiring enough melt to be able to resolve a secondary sill and the collapse of the evacuated region. There will be two competing situations at play if this spatial criterion was changed. An increase in the thickness of the melt required to be present, requiring more partial melt to persist late in the basalt solidification period, will result in less contribution of the surrounding crust on the rhyolitic melt. A stricter spatial criterion will also only be satisfied with overall higher ambient

temperatures, indicating less rhyolite production and only from hotter sections of the crust. We save investigation of the criteria, and development of a more robust strategy for evacuating melt as a focus of a future study.

Because we allow for fully generalized basaltic sill emplacement histories, including depth and time of emplacement, temperature, and thickness, TIRAMISU can be used to explore a myriad of cases. Additionally, the region over which sills are emplaced does not need to be static throughout the simulation, for instance we can consider a case where the window in which sills are emplaced shoals through the simulation. The movement of where sills are emplaced could be pre-ordained based upon basalt-granitoid ratio, or the emplacement location could be based on factors such as average ambient temperature within the emplacement interval. If the region in which basaltic sills are emplaced shoals enough to overlap with the depth ranges in which secondary rhyolitic sills are placed, then this would inherently promote multiple stages of crustal reworking. Moreover, distance over which secondary melt travels up the crustal column is not a fixed value, rather it depends on ambient temperatures and assumptions of fracture width and network, relevant for molten aplite dikes. We recognize the secondary segregation and transport process cannot be truly instantaneous, and that there are factors such overburden pressure relative to the volume increase of fluid-undersaturated partial melts (>10%; Lange, 1997; Ochs & Lange, 1999), among others. We intend to explore a more dynamics-based secondary sill emplacement scheme in future work.

Conclusions

We present a new numerical simulation too, TIRAMISU, which solves for the evolution of temperatures, transient partial melting/solidification, and compositional changes in response to

episodic emplacement of basaltic sills in the crust. TIRAMISU includes possible transport of partial and residual melts to secondary sills. TIRAMISU follows from the numerical solution in Calogero et al. (2020), and achieves spatial resolution on order of a meter and temporal resolution on order of days, while still being able to simulate tens of kilometers of the crustal column over millions of years of repeated basaltic sills invading the crust. TIRAMISU includes (1) broad input generalization for the factors involved in individual sill emplacements, (2) the removal of secondary (i.e., rhyolitic) melt from the deep crust and its subsequent emplacement as sills higher in the crustal column, and (3) the tracking of the compositional evolution of individual trace elements (i.e., Sr) in secondary melt, and whole rock evolution at the crustal, km-scale. TIRAMISU is the first simulation tool in the geological literature, that we are aware of, to directly include the transport of secondary melt, which greatly affects the thermal and compositional profile of the crust. While our motivation for development of TIRAMISU, and the focus of this paper, was the Long Valley caldera in eastern California, it is our hope that TIRAMISU will have applicability to broader locations.

We implement a new set of criteria to trigger the removal of wall-rock partial melt adjacent to newly emplaced basaltic sills, together with residual melt from fluid-saturated, crystallizing sills. These newly developed criteria for secondary melt transport are rooted in previously established understanding of the relative timescales of fluid saturation during crystallization and the partial melting of wall rock (Calogero et al., 2020), together with a recognition of the ubiquitous presence of aplite dikes as an available mechanism for transport. Using these criteria, the simulation results are geologically reasonable, in terms of both the relative amount (i.e., thickness) and composition (i.e., rhyolitic) of melts that are subsequently emplaced as sills higher in the crustal column. Nevertheless, the choices of criteria can be

modified and varied in future studies to explore how their changes affect the thermal and compositional profile of the crustal column.

The simulations presented here demonstrate that the removal of secondary melt from the deep crust leads to cooling, while the emplacement of that melt at shallower depths leads to warming. While this result was fully anticipated, this study is the first to quantify the effect. With the sill emplacement history used in these simulations (basalt emplacement rate of 50 m per 5 kyr, basalt randomly emplaced between an initial 20–30 km interval, secondary melts randomly emplaced between an initial 18–20 km interval), the difference in thermal profiles between simulations with no secondary melt transport versus with secondary transport is up to about 60°C of cooling where secondary melts were removed and about 60°C of warming where they were emplaced. The transport of secondary melts significantly alters crustal-scale thermal profiles, and thus must be included in models exploring how the influx of basaltic magma heats the crust, driving magmatism and volcanism.

TIRAMISU also tracks the Sr (and Nd) composition of secondary melts (i.e., first-, second- and third-generation melts) formed by the influx of basalt into a thermally and compositionally evolving crustal column. While we've only focused on these two, a wide number of major and trace elements can be tracked within the existing architecture of TIRAMISU. Consideration of more elements will lead to tighter constraints on the number of differentiation events (i.e., extraction of wall-rock partial melts and residual melts in basaltic sills) and the composition of the source rocks involved. Exploring these variations in numerical simulations will be an active area of our future work.

A final key conclusion of these simulations is that the production of rhyolitic melts, driven by the influx of basaltic magma into the crust, is greatly enhanced if residual melt from

crystallizing, hydrous basalt and partial melt of granitoid wall rock are both involved and closely interact. It is shown in this study that the transfer of water from the basaltic sills plays a critical role in the production of significant partial melting of granitoid. The effectiveness of that volatile transfer in driving partial melting is heightened if adjacent wall rock, over meter-scale distances from the basaltic sill, is involved, which is only captured because of the high spatial and temporal resolution within TIRAMISU. Moreover, melt fractions are greatly increased if the wall rock is granitoid rather than basaltic. It is proposed that the fact that an unusually thick layer of granitoid is present beneath the Long Valley caldera region (~32 km; Fleidner et al., 2000), together with the relatively hydrous nature of the Long Valley basalts (~3-6 wt% H_2O; Jolles, 2020), has enabled the production of voluminous and highly differentiated rhyolites from the Long Valley caldera over the last 2.2 Myr.

Acknowledgements

This research was supported by the National Science Foundation (EAR-1855751), as well as discretionary research funds from the University of Michigan (UM). The first author was partially supported by a graduate student fellowship from the Department of Earth and Environmental Sciences at the UM. TIRAMISU is still in development and will be publicly disseminated when this chapter is submitted for publication.

References

Anderson, A.T., Davis, A.M., & Lu, F. (2000). Evolution of Bishop Tuff rhyolitic magma based on melt and magnetite inclusions and zoned phenocrysts. *Journal of Petrology*, 41(3), 449-473. https://doi.org/10.1093/petrology/41.3.449

Andersen, N.L., Jicha, B.R., Singer, B.S., & Hildreth, W. (2017). Incremental heating of Bishop Tuff sanidine reveals preeruptive radiogenic Ar and rapid remobilization from cold

storage. *Proceedings of the National Academy of Sciences of the United States of America*, 114(47), 12407-12412. https://doi.org/10.1073/pnas.1709581114

Annen, C., Blundy, J.D., & Sparks, R.S.J. (2006). The genesis of intermediate silicic magmas in deep crustal hot zones. *Journal of Petrology,* 47(3), 505-539. http://doi.org/10.1093/petrology/egi084

Bailey, R.A. (1989). Geologic map of the Long Valley caldera, Mono-Inyo craters volcanic chain, and vicinity, eastern California. U.S. Geological Survey Map I-1933. https://doi.org/10.3133/i1933

Barth, A.P., Walker, J.D., Wooden, J.L., Riggs, N.R. & Schweickert, R.A.. (2011). Birth of the Sierra Nevada magmatic arc: Early Mesozoic plutonism and volcanism in the east-central Sierra Nevada of California. *Geosphere,* 7, 877-897.

Befus, K.S., Gardner, J.E., & Zinke, R.W. (2012) Analyzing water contents in unexposed glass inclusions in quartz crystals. *American Mineralogist*, 97, 1898-1904.

Befus, K.S., Zinke, R.W., Jordan, J.S., Manga, M. & Gardner, J.E. (2014) Pre-eruptive storage conditions and eruption dynamics of a small rhyolite dome: Douglas Knob, Yellowstone volcanic field, USA. *Bulletin of Volcanology,* 76:808. https://doi.org/10.1007/s00445-014-0808-8

Bezanson, J., Edelman, A., Karpinski, S., & Shah, V.B., (2017). Julia: A fresh approach to numerical computing. *SIAM Review*. 59:1, 65-98.

Bindeman, I.N. & Simakin, A.G. (2014). Rhyolites–hard to produce, but easy to recycle and sequester: Integrating microgeochemical observations and numerical models. *Geopshere*, 10(5), 930-957. https://doi.org/10.1130/GES00969.1

Calogero, M.A., Hetland, E.A., & Lange, R.A. (2020) High-resolution numerical model of heat and volatile transfer from basalt to wall rock: application to the crustal column beneath Long Valley caldera, CA. *Journal of Geophysical Research: Solid Earth*, 125, e2018JB016773. https://doi.org/10.1029/2018JB016773

Coleman, D.S. & Glazner, A.F. (1997). The Sierra Crest magmatic event: rapid formation of juvenile crust during the Late Cretaceous in California. *International Geology Review,* 39, 768-787.

Colón, D.P., Bindeman, I.N. & Gerya, T.V. (2018). Thermomechanical modeling of the formation of a multilevel, crustal-Scale magmatic system by the Yellowstone plume. *Geophysical Research Letters,* 45, 3873-3879. https://doi.org/10.1029/2018GL077090

Cousens, B.L. (1996). Magmatic evolution of Quaternary mafic magmas at Long Valley caldera and the Devils Postpile, California: Effects of crustal contamination on lithospheric mantle-derived magmas. *Journal of Geophysical Research*, 101(B12), 27673-27689. https://doi.org/10.1029/96JB02093

Cousens, B., Henry, C.D., & Gupta, V. (2012). Distinct mantle sources for Pliocene-Quaternary volcanism beneath the modern Sierra Nevada and adjacent Great Basin, northern California and western Nevada, USA. *Geosphere,* 8(3), 562-580. https://doi:10.1130/GES00741.1

Davies, G.R., Halliday, A.N., Mahood, G.A. & Hall, C.M. (1994). Isotopic constraints on the production rates, crystallization histories and residence times of pre-caldera silicic magmas, Long Valley, California. *Earth and Planetary Science Letters*, 125(4), 17-37. https://doi.org/10.1016/0012-821X(94)90204-6

Davies, G.R. & Halliday, A.N. (1998) Development of the Long Valley rhyolitic magma system: Strontium and neodymium isoope evidence from glasses and individual phenocrysts. *Geochimica et Cosmochimica Acta,* 62, 3561-3574.

Dormand, J., (1996). Numerical Methods for Differential Equations: A Computational Approach, pp. 368, CRC Press LLC, New York.

Dufek, J. & Bergantz, G.W. (2005). Lower crustal magma genesis and preservation: a stochastic framework for the evaluation of basalt–crust interaction. *Journal of Petrology*, 46(11), 2167-2195. https://doi.org/10.1093/petrology/egi049

Economos, R.C., Memeti, V., Paterson, S.R, Miller, J.S., Erdmann, S. & Zak, J. (2010). Causes of compositional diversity in a lobe of the Half Dome granodiorite, Tuolumne batholith, central Sierra Nevada, California. *Earth and Environmental Science Transactions of the Royal Society of Edinburgh*, 100, 173-183.

Fliedner, M.M., Klemperer, S.L. & Christensen, N.I. (2000). Three-dimensional seismic model of the Sierra Nevada arc, California, and its implications for crustal and upper mantle composition. *Journal of Geophysical Research*, 105(B5), 10899-10922. https://doi.org/10.1029/2000JB90002

Guo, X. , Lange, R.A. and Ai, Y. (2014) Density and sound speed measurements on model basalt (An-Di-Hd) liquids at one bar: New constraints on the partial molar volume and compressibility of the FeO component. Earth and Planetary Science Letters, 388, 283-292. http://dx.doi.org/10/1016/j.epsl.2013.12.005

Halliday, A.N., Fallick, A.E., Hutchinson, J. & Hildreth, W. (1984). A Nd, Sr, and O isotopic investigation into the causes of chemical and isotopic zonation in the Bishop Tuff, California. *Earth and Planetary Science Letters*, 68(3), 379-391. https://doi.org/10.1016/0012-821X(84)90123-7

Halliday, A.N., Mahood, G.A., Holden, P., Metz, J.M., Dempster, T.J., & Davidson, J.P. (1989) Evidence for long residence times of rhyolitic magma in the Long Valley magmatic system: the isotopic record in precaldera lavas of Glass Mountain. *Earth and Planetary Science Letters*, 94, 274-290.

Hildreth, W. (2004). Volcanological perspectives on Long Valley, Mammoth Mountain, and Mono Craters: several contiguous but discrete systems. *Journal of Volcanology and Geothermal Research*, 136, 169-198. https://doi.org/10.1016/j.jvolgeores.2004.05.019

Hildreth, W. (2007). Quaternary magmatism in the Cascades-Geological Perspectives. U.S. *Geological Survey Professional Paper* 1744, 125 p.

Hildreth, W., Fierstein, J., & Calvert, A. (2017). Early postcaldera rhyolite and structural resurgence at Long Valley Caldera, California. *Journal of Volcanology and Geophysical Research*, 335, 1-34. https://doi.org/10.1016/j.jvolgeores.2017.01.005

Hildreth, W. & Wilson, C.J.N. (2007). Compositional zoning of the Bishop Tuff. *Journal of Petrology*, 48(5), 951-999. https://doi.org/10.1093/petrology/egm007

Holbrook, WS., Mooney, W.D. & Christensen, N.I. (1992). The seismic velocity structure of the deep continental crust. In D.M. Fountain, R. Arculus, & R.W. Kay (Eds.), Continental Lower Crust (pp. 423-445). Amsterdam: Elsevier.

Huang, W. & Russell, R.D. (2011). Adaptive moving mesh methods. *Applied mathematical sciences*. (Vol. 174). New York, NY: Springer. https://doi.org/10.1007/978-1-4419-7916-2

Huppert, H.E. & Sparks, R.S.J. (1988). The generation of granitic magmas by intrusion of basalt into continental crust. *Journal of Petrology*, 29(3), 599-624. https://doi.org/10.1093/petrology/29.3.599

Jackson, M.D., Cheadle, M.J. & Atherton, M.P. (2003). Quantitative modeling of granitic melt generation and segregation in the continental crust. *Journal of Geophysical Research*, 108(B7), 2332, https://doi.org/10.1029/2001JB001050

Karakas, O. & Dufek, J. (2015). Melt evolution and residence in extending crust: Thermal modeling of the crust and crustal magmas. *Earth and Planetary Science Letters*, 425, 131-144. https://doi.org/10.1016/j.epsl.2015.06.001

Kistler, R.W., Chappell, B.W., Peck, D.L. & Bateman, P.C. (1986). Isotopic variation in the Tuolumne Intrusive Suite, central Sierra Nevada, California. *Contributions to Mineralogy and Petrology,* 94, 205-220.

Johannes, W. & Holtz, F (1996). *Petrogenesis and Experimental Petrology of Granitic Rocks:* Minerals and Rock Series, Volume 22, Berlin, Springer-Verlag, 335 p. https://doi.org/10.1093/petroj/38.1.165

Jolles J.S.R. (2020). Insights on the temperatures, mechanisms and timescales of voluminous (>600 km^3) high-SiO_2 (75-77 wt%) rhyolite melt generation at Long Valley, CA. University of Michigan, Ann Arbor, Ph.D. thesis

Kay, R.W., Kay, S.M. & Arculus, R.J. (1992). Magma genesis and crustal processing. In D.M. Fountain, R. Arculus, & R.W. Kay (Eds.), Continental Lower Crust (pp. 423-445). Amsterdam: Elsevier.

Klein, M., Stosch, H.G., & Seck, H.A. (1997). Partitioning of high field-stragnth and rare-earth elements between amphibole and quartz-dioritic to tonalitic melts: An experimental study. *Chemical Geology,* 138(3-4), 257-271. https://doi.101016/S0009-254(97)00019-3.

Lange, R.A. & Carmichael, I.S.E. (1990). Thermodynamic properties of silicate liquids with an emphasis on density, thermal expansion and compressibility. In, Nicholls, J and Russel, K. (Eds) Mineralogical Society of America, Reviews in Mineralogy: Modern Methods of Igneous Petrology, 24, 25-64.

Lange, R.A. (1997). A revised model for the density and thermal expansivity of K_2O-Na_2O-CaOMgO-Al_2O_3-SiO_2 liquids from 700-1900 K: extension to crustal magmatic temperatures. *Contributions to Mineralogy and Petrology*, 130, 1-11. https://doi.org/10.1007/s004100050345

Leeman, W.P., Annen, C. & Dufek, J. (2008). Snake River Plain – Yellowstone silicic volcanism: implications for magma genesis and magma fluxes. *Geological Society, London, Special Publications*, 304, 235-259. https://doi.org/10.1144/SP304.12

Lesher, C.E. & Spera, F.J. (2015). Thermodynamic and transport properties of silicate melts and magmas. In, Sigurdsson, H. (Ed.), *The Encyclopedia of Volcanoes* (pp. 113-141)

Levander, A. & Miller, M.S. (2012). Evolutionary aspects of lithosphere discontinuity structure in the western U.S. *Geochemistry, Geophysics, Geosystems*, 13(7), Q0AK07. https://doi.org/10.1029/2012GC004056

Metz, J.M. & Mahood, G.A. (1991). Development of the Long Valley, California, magma chamber recorded in precaldera rhyolite lavas of Glass Mountain. *Contributions to Mineralogy and Petrology*, 106(3), 379-397. https://doi.org/10.1007/BF00324565

NAVDAT (2014) The Western North American Volcanic and Intrusive Rock Database. https://www.navdat.org

Ochs, F.A. & Lange, R.A. (1999). The density of hydrous magmatic liquids. *Science*, 283(5406), 1314-1317. https://10.1126/science.283.5406.1314

Oliver, H.W., Moore, J.G. & Sikora, R.F. (1993). Internal structure of the Sierra Nevada batholith based on specific gravity and gravity measurements. *Geophysical Research Letters*, 20(20), 2179-2182. https://doi.org/10.1029/93GL01379

Pertermann, M. & Hirschmann, M.M. (2002). Trace-element partitioning between vacancy-rich eclogitic clinopyroxene and silicate melt. *American Mineralogist,*87, 1365-1376.

Prowatke, S. & Klemme, S. (2006). Rare earth element partitioning between titanite and silicate melts: Henry's law revisited. *Geochimica et Cosmochimica Acta,*70, 4997-5012.

Roberge, J., Wallace, P.J. & Kent, A.J.R. (2013) Magmatic processes in the Bishop Tuff rhyolitic magma based on trace elements in melt incusions and pumice matrix glass. *Contributions to Mineralogy and Petrology,* 165, 237-257.

Saleeby, J., Ducea, M.& Clemens-Knott, D. (2003). Production and loss of high-density batholitic root, southern Sierra Nevada, California. *Tectonics*, 22(6), 1064. https://doi.org/10.1029/2002TC001374

Simakin, A.G. & Bindeman I.N. (2012). Remelting in caldera and rift environments and the genesis of hot, "recycled" rhyolites. *Earth and Planetary Science Letters*, 337-338, 224-235. https://doi.org/10.1016/j.epsl.2012.04.011

Simon, J.I., Weis, D., DePaolo, D.J., Renne, P.R., Mundil, R. & Schmitt, A.K. (2014). Assimilation of preexisting Pleistocene intrusions at Long Valley by periodic magma recharge accelerates rhyolite generation: rethinking the remelting model. *Contributions to Mineralogy and Petrology*, 167, 955. https://doi.org/10.1007/s00410-013-0955-5

Sisson, T.W. & Bacon, C.R. (1999) Gas-driven filter pressing in magmas. *Geology*, 27(7), 613-616.

Sisson, T.W., Ratajeski, K., Hankins, W.B., & Glazner, A.F. (1999) Voluminous granitic magmas from common basaltic sources. *Contributions to Mineralogy and Petrology*, 148, 635-661.

Wallace, P.J., Anderson, A.T. & Davis, A.M. (1999). Gradients in H_2O, CO_2, and exsolved gas in a large-volume silicic magma system: Interpreting the record preserved in melt inclusions from the Bishop Tuff. *Journal of Geophysical Research*, 104(B9), 20097-20122. https://doi.org/10.1029/1999JB900207

Wilson, C.J.N. & Hildreth, W. (1997). The Bishop Tuff: new insights from eruptive stratigraphy. *The Journal of Geology*, 105(4), 407-440. https://doi.org/10.1086/515937

Zandt, G., Hersh, G., Owens, T.J., Ducea, M., Saleeby, J. & Jones, C.H. (2004). Active foundering of a continental arc root beneath the southern Sierra Nevada in California. *Nature*, 431(7004), 41-46. https://doi.org/10.1038/nature02847

CHAPTER 4
Conclusion

In the previous chapters, I addressed many questions surrounding the nature of rhyolite generation as a consequence of basalt influx in the crust, with particular consideration for the unique tectonic and geochemical setting of Long Valley caldera, California. Chapter 2 presented a 1-D numerical model which I developed, achieving high spatial (1 meter) and temporal (< day) resolution, while still calculating the temperature evolution over the ~40-kilometer crust, and over millions of years. The adaptive resolving power of this numerical model allows simulations to capture the whole crustal-scale and local sill-scale responses to an instantaneous emplacement of basaltic magma at depth.

Chapter 2 presented several simulations, testing various aspects of magmatic emplacement in the crust, revealing that the emplacement geometry, emplacement rate and sill thickness exert the strongest controls on crustal scale thermal evolution, in agreement with previous numerical modeling (e.g., Huppert & Sparks, 1988; Petford & Gallagher, 2001; Jackson et al., 2003; Dufek & Bergantz, 2005; Annen et al., 2006; Leeman et al., 2008; Karakas & Dufek, 2015; Colón et al., 2018). Additionally, I identified that the melt fraction-temperature relationships for basalt and wall rock, with H_2O content specifically considered, plays a significant role in the extent of partial melting. Time scales for H_2O exsolution from crystallizing

basaltic sills and for transient partial melt generation from neighboring wall rock with variations depending on sill-scale ambient temperature were quantified on the order of 10–100s of years.

Given the high volatile content of the Long Valley basalts (3–6 wt% H_2O; Jolles, 2020), fluid-undersaturated high-SiO_2 rhyolitic partial melts of wall rock together with interstitial low-SiO_2 rhyolitic melts derived from the crystallizing basalts, which are fluid-saturated upon segregation, may undergo secondary transport along melt-filled fractures facilitated by the ubiquitous pre-existing scattered aplite dikes in the Sierra Nevada batholith (Lange, 2019). This viable hypothesis became the basis for Chapter 3, where I explored the thermal and compositional consequences of secondary melt segregation and transport.

In Chapter 3, I developed new simulation tool, TIRAMISU (Transient hIgh-Resolution pArtial MeltIng Simulation of the crUst), implemented in the Julia programming language (Bezanson et al., 2017). TIRAMISU is an extension of the model presented in Chapter 2, and includes the ability to allow for a stage of secondary melt transport within the crustal column, triggered if specific criteria are met. I use a temporal criterion, based on volatile release from a crystallizing basaltic sill, and a spatial criterion, requiring cumulative partial melt above the primary basaltic sill to be resolvable given model resolution constraints. TIRAMISU also includes compositional tracking of the full crust as a consequence of secondary melt transport, focusing on Sr concentration in the simulations presented in Chapter 3. Sr was chosen due to its paradoxical constraints on the Long Valley volcanic system. There is extreme depletion of Sr in LV high-SiO_2 rhyolites (<25 ppm; Hildreth, 1979; Metz & Mahood, 1991) relative to the surrounding Sierra Nevada batholith (~490 ppm; NAVDAT, 2014) and the Sr-rich LV basalts (1000–2000 ppm early and ~550 ppm late; Cousens, 1996), while the Sr isotopic signature of the

LV rhyolites is low (~0.7068; e.g., Davies & Halliday, 1998) showing the influence of mantle-derived basalt.

The scientific results of the simulations in Chapter 3 are fourfold. (1) There is a heating and cooling effect along the crustal thermal profile where secondary melts were emplaced and extracted from respectively, which resulted in a quasi-steady-state gain/loss of ~60ºC with transport compared to without transport after about 150 kyr, for a basalt emplacement rate of 5 km per 5 kyr. While the heating/cooling of the crust when secondary melt transport is considered was anticipated, this is the first time to our knowledge it has been quantified, and the degree of temperature variation will be tested in future work at additional basalt emplacement rates. (2) For 3 km of basalt emplaced, about 1.7 km of rhyolite was generated and transported to the upper crust, with a cumulative 70% relative contribution of partial melt from granitoid on average and the remaining ~30% derived collectively from partial melts of solidified mafic sills and interstitial melts of crystallizing basalts. The finite availability of volatiles in the eruptive basalts of Long Valley (3–6 wt%; Jolles, 2020), coupled with the thick granitoid basement (32 km; e.g., Fieldner et al., 2000), makes this extensive melting possible. (3) We observe 380 ppm Sr on average in the secondary rhyolites, and an average $^{87}Sr/^{86}Sr$ of 0.7068. (4) Even though about 30% of the rhyolitic melt is derived from basaltic sources, approximately 60% of the Sr can be attributed to basaltic sources. These results, which are for the first generation of rhyolites, can be used to constrain simplified calculations of Sr, and other trace elements such as Nd, in investigating the geochemistry of second and third generation of rhyolites, and so on.

TIRAMISU continues to be expanded, and in the near future, incorporation of Nd concentration and isotopic signature tracking will aid in further constraining the stages of rhyolite melting to generate a geochemically accurate parent for the Bishop tuff, as identified by

Jolles (2020). A rigorous evaluation of the crustal thermal response and extensiveness of secondary melt generation at additional emplacement rates and under other emplacement geometries will expand the power of this numerical study.

When granitoid is heated, aplite dikes, which are ubiquitous pre-existing high-SiO_2 rhyolites formed during late-stage crystallization of granitoid, will melt entirely. Their fracture channels may act as transport fractures in granitoid (e.g, Lange, 2019) through self-propagation, should a critical fracture length be achieved (Gonnermann & Taisne, 2015), but there is more rigorous work ahead to evaluate the efficacy of this process and any further constraint criteria it may impose on the triggering of secondary melt transport. The volume of melt from an aplite will be substantially overwhelmed by partial melts of granitoid. Evacuation of aplite melts from the lower crust will form a pressure gradient, which will tend to draw partial melts from granitoid crust into the pre-existing fracture. Melts in TIRAMISU are moved an arbitrary distance up the crustal column, and while we use distances that are geologically informed, in order to be more dynamically consistent, the calculation of the distance over which secondary rhyolitic melts will ascend up the crustal column needs to be included in TIRAMISU. The critical width of a dike, which allows melt to ascend at a rate fast enough to keep it from solidifying as it moves to the shallower, and cooler, crust can be estimated (Petford et al., 1993), but rigorously including this critical width in a 1D model is not straightforward. Dikes in which melt ascends are near-vertical and so a consideration of their widths in simulations requires at least a 2D model. As 2D models pose significant additional computational cost, and at this time are not tractable for these multi-resolution simulations, aspects of critical width of the dikes needs to be mapped. I intend to explore methods to essentially map the notion of critical width into our 1D simulations. There are other geophysical factors that influence the ascent of melt in

the crust, which are more straightforward to incorporate in TIRAMISU. These factors include depth-induced overburden pressure relative to the internal pressure generated from volume expansion of fluid-undersaturated melting, the density of magma while it remains above its liquidus relative to when crystallization initiates, and the effect of reaching fluid saturation during ascent. There is an expectation that the liquidus of ascending fluid-undersaturated rhyolitic magmas will decrease during ascent, due to the positive dT/dP of their liquidus, which would prolong transit through the crust despite conductive loss of heat (Waters & Lange, 2017). The end-goal is to replace the prescribed depths at which secondary melts are placed in the current version of TIRAMISU, with dynamically consistent rules for the ascent of the secondary melts, including realistic ascent times rather than the instantaneous ascent currently assumed in TIRAMISU.

TIRAMISU is a tool, and while our development of it was focused on one geologic setting, it is my ultimate aim that TIRAMISU be applied to a wide range of volcanic systems. Other large caldera-forming eruptions, such as the high-SiO_2 rhyolitic eruptions from Yellowstone caldera, would be the most direct next targets for TIRAMISU. However, I am also interested in applying TIRAMISU to subduction zone magmatism, which will require consideration of different secondary melt transport triggers, as aplite dikes are absent in mafic wall rocks. Lastly, the model presented in this study is in 1-D, with sills implicitly horizontal and with infinite extent. In future work, I will consider basaltic melts with finite dimensions and track coeval thermal profiles at some distance apart, over a 2D or 3D volcanic network Extending from 1D simulations to 2D or 3D would allow realistic volumes of secondary rhyolitic melt, with finite volatile and geochemical compositions, to be constrained, although these higher dimension simulations would require other computational solutions to achieve the high spatial

and temporal resolutions required to capture transient melting/solidification, while still being able to simulate the evolution of the entire crust over millions of years.

References

Annen, C., Blundy, J.D., & Sparks, R.S.J. (2006). The genesis of intermediate silicic magmas in deep crustal hot zones. *Journal of Petrology,* 47(3), 505-539. http://doi.org/10.1093/petrology/egi084

Bezanson, J., Edelman, A., Karpinski, S., & Shah, V.B., (2017). Julia: A fresh approach to numerical computing. *SIAM Review*. 59:1, 65-98.

Colón, D.P., Bindeman, I.N. & Gerya, T.V. (2018). Thermomechanical modeling of the formation of a multilevel, crustal-Scale magmatic system by the Yellowstone plume. *Geophysical Research Letters,* 45, 3873-3879. https://doi.org/10.1029/2018GL077090

Connolly, J.A.D., Holness, M.B., Rubie, D., Rushmer, T. (1997). Reaction-induced microcraking: an experimental investigation of a mechanism for enhancing anatectic melt extraction. *Geology,* 25, 591-594. http://doi.org/10.1130/0091-7613(1997)025<0591:RIMAEI>2.3.CO

Cousens, B.L. (1996). Magmatic evolution of Quaternary mafic magmas at Long Valley caldera and the Devils Postpile, California: Effects of crustal contamination on lithospheric mantle-derived magmas. *Journal of Geophysical Research*, 101(B12), 27673-27689. https://doi.org/10.1029/96JB02093

Davies, G.R. & Halliday, A.N. (1998) Development of the Long Valley rhyolitic magma system: Strontium and neodymium isoope evidence from glasses and individual phenocrysts. *Geochimica et Cosmochimica Acta,* 62, 3561-3574.

Dufek, J. & Bergantz, G.W. (2005). Lower crustal magma genesis and preservation: a stochastic framework for the evaluation of basalt–crust interaction. *Journal of Petrology*, 46(11), 2167-2195. https://doi.org/10.1093/petrology/egi049

Gonnermann, H. & Taisne, B. (2015). Magma transport in dikes. In, Sigurdsson, H. (Ed.), *The Encyclopedia of Volcanoes* (pp. 215-224)

Hildreth, W. (1979) The Bishop Tuff: evidence for the origin of compositional zonation in silicic magma chambers. In: Chapin, C.E. & Elston, W.E. (eds) Ash-flow tuffs. Geological Society of America Special Paper, 180, 43-75.

Huppert, H.E. & Sparks, R.S.J. (1988). The generation of granitic magmas by intrusion of basalt into continental crust. *Journal of Petrology*, 29(3), 599-624. https://doi.org/10.1093/petrology/29.3.599

Jackson, M.D., Cheadle, M.J. & Atherton, M.P. (2003). Quantitative modeling of granitic melt generation and segregation in the continental crust. *Journal of Geophysical Research*, 108(B7), 2332, https://doi.org/10.1029/2001JB001050

Karakas, O. & Dufek, J. (2015). Melt evolution and residence in extending crust: Thermal modeling of the crust and crustal magmas. *Earth and Planetary Science Letters*, 425, 131-144. https://doi.org/10.1016/j.epsl.2015.06.001

Jolles J.S.R. (2020). Insights on the temperatures, mechanisms and timescales of voluminous (>600 km^3) high-SiO_2 (75-77 wt%) rhyolite melt generation at Long Valley, CA. University of Michigan, Ann Arbor, Ph.D. thesis

Lange, R.A. (2019). Evidence for rapid transport of rhyolite melt during hydrous partial melting of granitoid: the critical role of pre-existing aplite dikes and fluid-undersaturated conditions. *American Geophysical Union Fall Meeting Abstracts,* V44A-01.

Leeman, W.P., Annen, C. & Dufek, J. (2008). Snake River Plain – Yellowstone silicic volcanism: implications for magma genesis and magma fluxes. *Geological Society, London, Special Publications*, 304, 235-259. https://doi.org/10.1144/SP304.12

Metz, J.M. & Mahood, G.A. (1991). Development of the Long Valley, California, magma chamber recorded in precaldera rhyolite lavas of Glass Mountain. *Contributions to Mineralogy and Petrology*, 106(3), 379-397. https://doi.org/10.1007/BF00324565

Petford, N. & Gallagher, K. (2001). Partial melting of mafic (amphibolitic) lower crust by periodic influx of basaltic magma. *Earth and Planetary Science Letters*, 193(3-4), 483-499. https://doi.org/10.1016/S0012-821X(01)00481-2

Waters, L.E., & Lange, R.A., (2017). Why aplites freeze and rhyolites erupt: Controls on the accumulation and eruption of high-SiO2 (eutectic) melts. *Geology*, 45(11), 1019-1022. https://doi.org/10.1130/g39373.1

Appendices

Appendix A

Supplemental Material for Chapter 2

Supplement A-1 ThermEvolAM numerical model for sill emplacement, transient partial melt generation, and heating of the crust

This supplement (MATLAB files and functions) can be retrieved from Github via Zenodo (zenodo.org) or from the *Journal of Geophysical Research: Solid Earth* at:

Calogero, M. A., Hetland, E. A., & Lange, R. A. (2020). High-resolution numerical modeling of heat and volatile transfer from basalt to wall rock: Application to the crustal column beneath Long Valley caldera, CA. *Journal of Geophysical Research: Solid Earth*, 125, e2018JB016773. https://doi.org/10.1029/2018JB016773

Zenodo doi: 10.5281/zenodo.3549797

Supplement A-2 Figures regarding the mechanism and timescale of heat and volatile transfer at the crustal- and sill-scale from basalt to wall rock

In the Supporting Information for this manuscript, seventeen figures are provided. These figures provide background information that are not central to the main body of the paper, but provide additional information that may be of interest to the reader. Figure A-1 is pair of maps, first of the greater Basin and Range province, and second of the Long Valley Caldera. Figure A-2 provides a benchmark for the Runge-Kutta time-stepping scheme. Figure A-3 illustrates the initial conditions for all further simulations within this manuscript. Figure A-4 shows the nearly negligible results of a variable distribution of latent heat across the liquidus-solidus interval to crustal thermal profile. Figure A-5 similarly shows the results of varying sill thickness, while maintaining emplacement rate, at the crustal scale. Figure A-6 demonstrates the thermal effect of varying the initial emplacement depth range, whether deeper or broader, to the crustal thermal profile. Figure A-7 illustrates how the ambient temperature in the crust increases during sill progression (but variably due to differences in sill-emplacement depth), and its effect on the time scale for a basaltic sill to reach 80% crystallization. Figures A-8 through A-11 are the same as Figures 2-7 through 2-10 in the main body of the text, but for 0.3 GPa instead of 0.5 GPa. Figures A-12 through A-14 supplement Figure 2-12, exploring the sill scale thermal and melt fraction evolution for a system where all sills are 10-m thick. Figures A-15 through A-17 supplement Figure 2-13 in the main body of the text, exploring the sill scale thermal and melt fraction evolution for a system where all sills are 100-m thick.

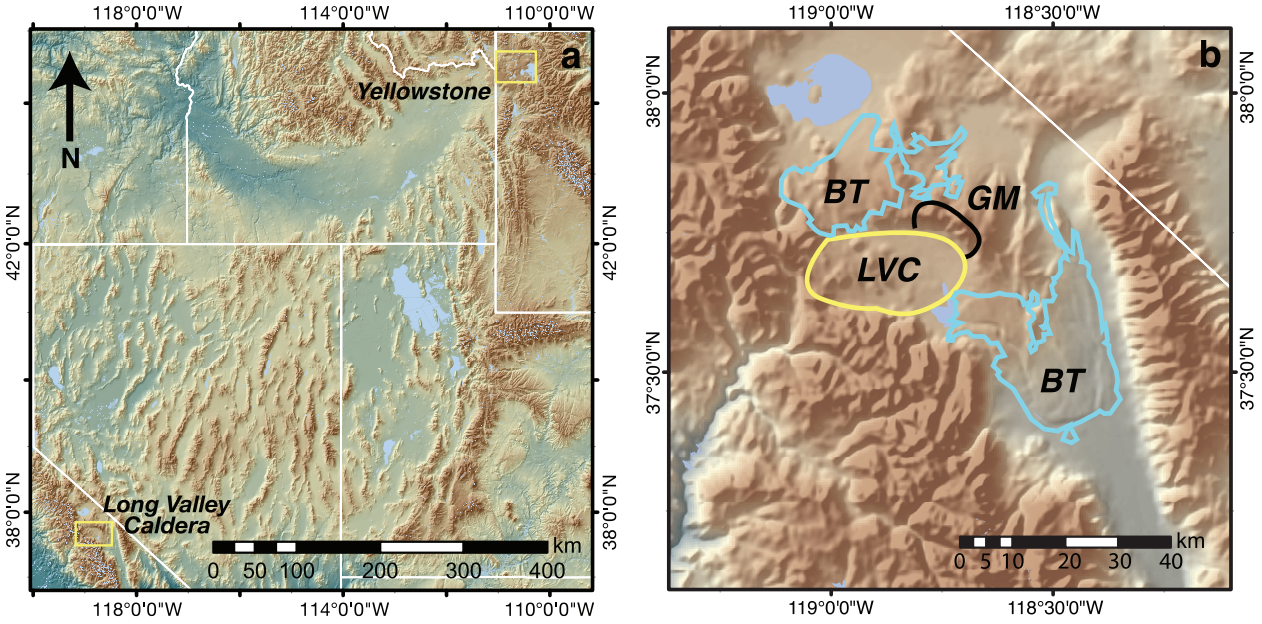

Figure A-1 (a) Map of Basin and Range province in western U.S.; Yellowstone, WY, and Long Valley, CA, are sites of super-volcano eruptions of high-SiO2 rhyolite <1 Ma. (b) Blow-up of Long Valley caldera, California; modified from Hildreth & Wilson (2007). BT is Bishop Tuff, LVC is Long Valley caldera, and GM is Glass Mountain.

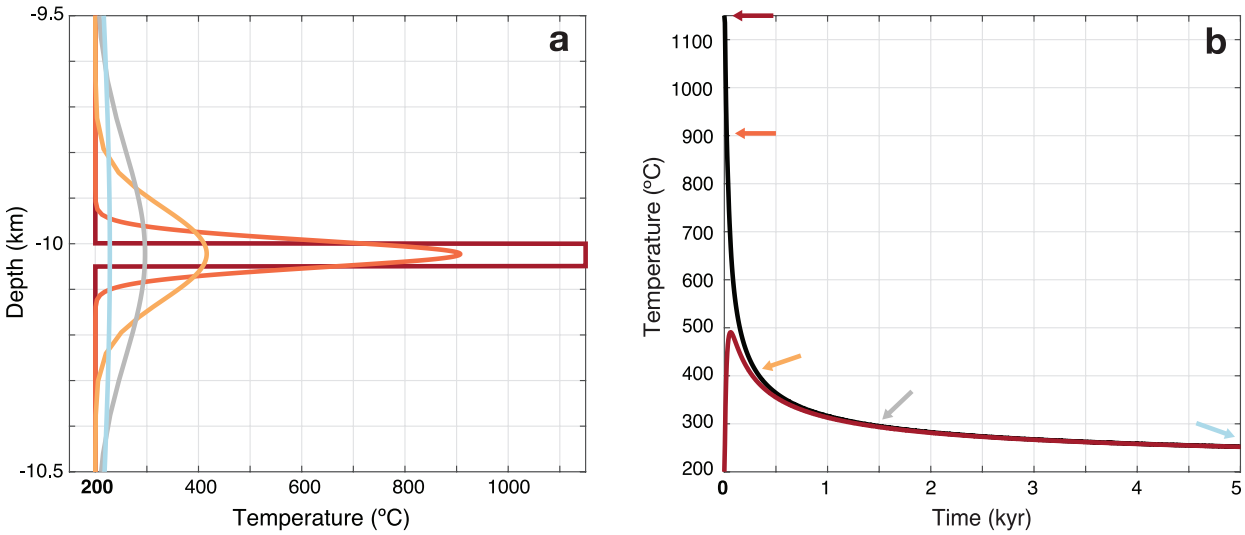

Figure A-2. A simulation was run with a crust that was top to bottom basaltic, using the 0.3 GPa F-T curve from Figure 2-1a. The crust was assigned a uniform temperature of 200ºC from top to bottom. A 50-m thick basaltic sill was then emplaced with its top surface at 10 km depth, and was allowed to cool. (a) A thermal profile of the cooling of the sill and the subsequent heating and cooling of the nearby crust above and below the sill. The curves are color coded for time stamps, pointed out from (b). (b) Shows the thermal evolution for the center of the sill (black) and 1 m outside of the sill (maroon).

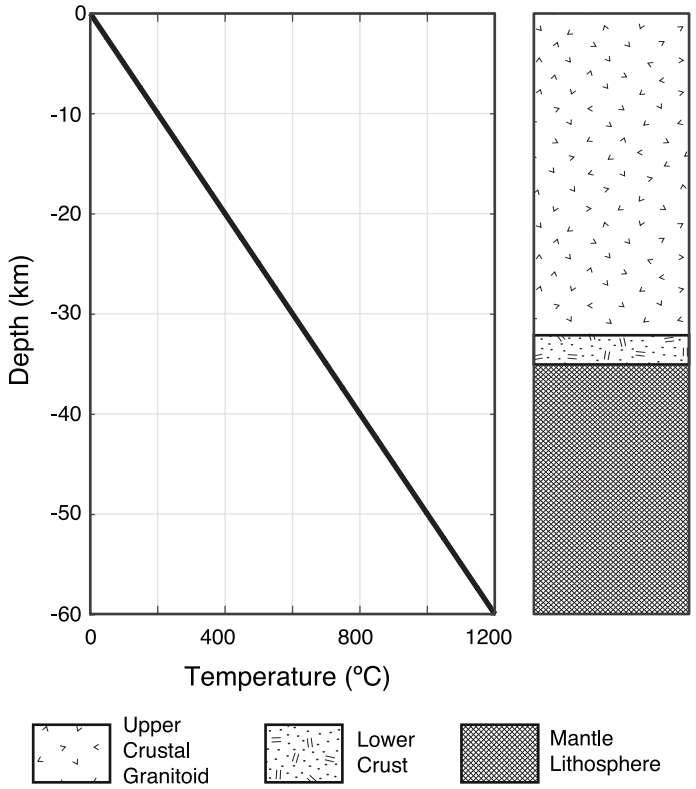

Figure A-3 Initial conditions for all numerical simulations in this study. Linear geotherm is 20ºC/km from the surface to the lithosphere-asthenosphere boundary (LAB) at 60 km depth. Temperatures at the surface and LAB are held fixed.

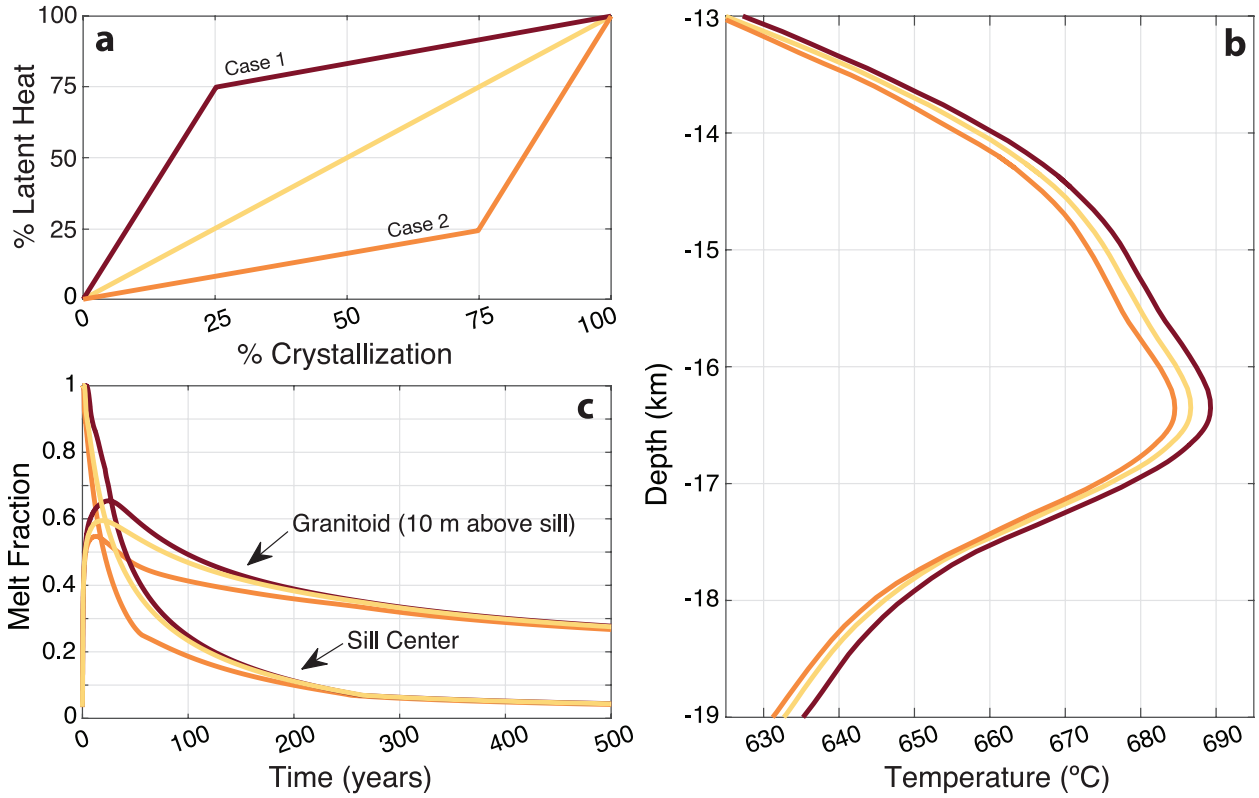

Figure A-4 (a) Plot of % latent heat released as a function of % crystallization in basaltic sill; default is a linear trend (solid yellow line). Case 1 (maroon) is a release of 75% of latent heat during first 25% of crystallization, and case 2 (orange) is release of 75% of latent heat during last 25% crystallization. (b) Blow-up of the thermal profile through crust using the same parameters as shown in Figure 2b in main text. Illustrates small changes in temperature ≤5 degrees across all three cases. (c) Sill-scale crystallization/melt fraction profile through the 100th sill and adjacent wall rock under fluid-present conditions (at 0.3 GPa; see Figure A-11). Although there is a difference in the time interval over which the basaltic sill crystallizes to 80% and over which the wall rock (10 m from sill margin) remains ≥30% molten, which depends on how latent heat is distributed across the liquidus-solidus interval, there is little difference among the three cases between time it takes sill in (c) to reach 80% crystallization and time the wall rock (10 m above sill) remains ≥30% melt fraction afterwards; case 1 = 278 years; linear = 275 years; case 2 = 267 years.

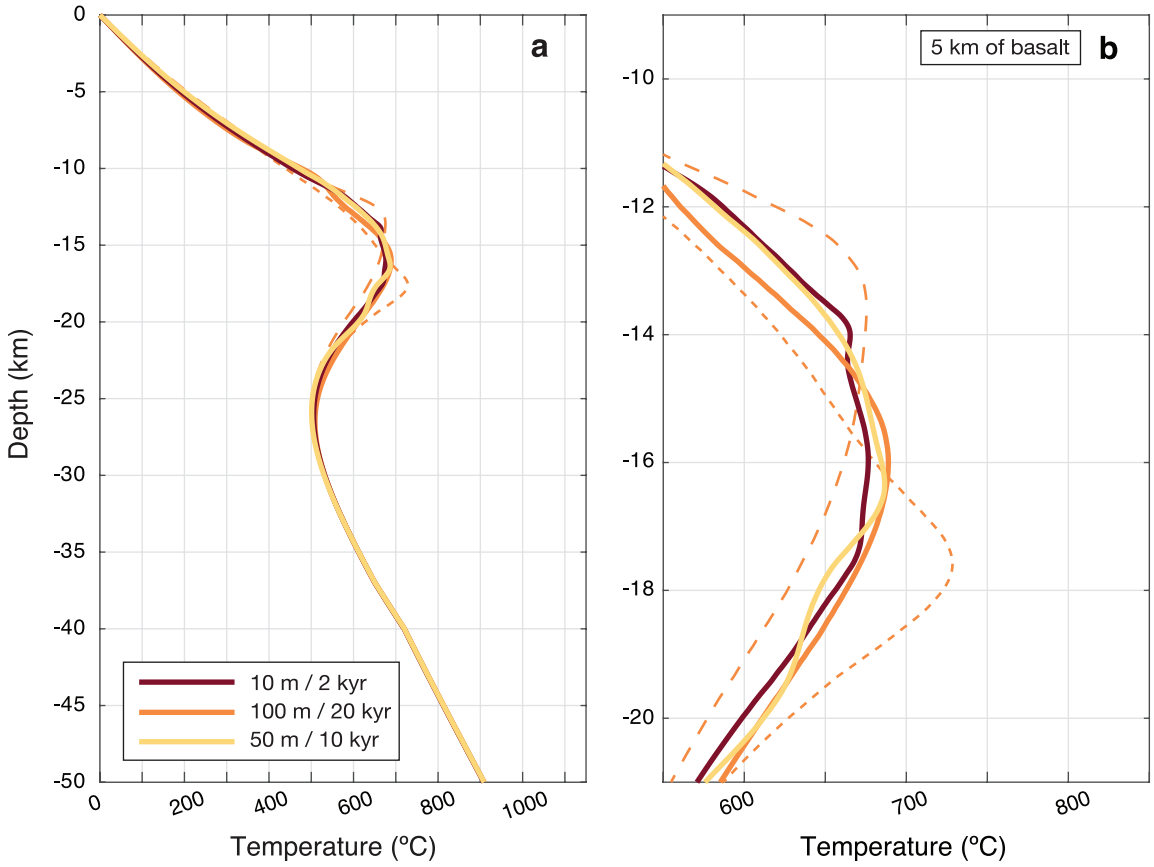

Figure A-5. (a) Thermal profile and (b) zoomed in thermal profile for emplacement of sills of varying thicknesses, into an initial 10-15 km window (10-20 km after 1 Myr in all cases). For the 100-m thick sill case, 3 simulations were run, one of which overlapped well with the 10-m and 50-m thick simulations, and ones where the final few sills were shallow, and another where the final few sills were deeper. This illustrates the sensitivities at the crustal scale thermal profile when dealing with large, infrequent magma injections. The 50 m/10 kyr (yellow) curve is the same from Figure 2-2b in the body of the paper. All simulations use fluid-absent F-T curves at 0.3 GPa (Figure 2-1b).

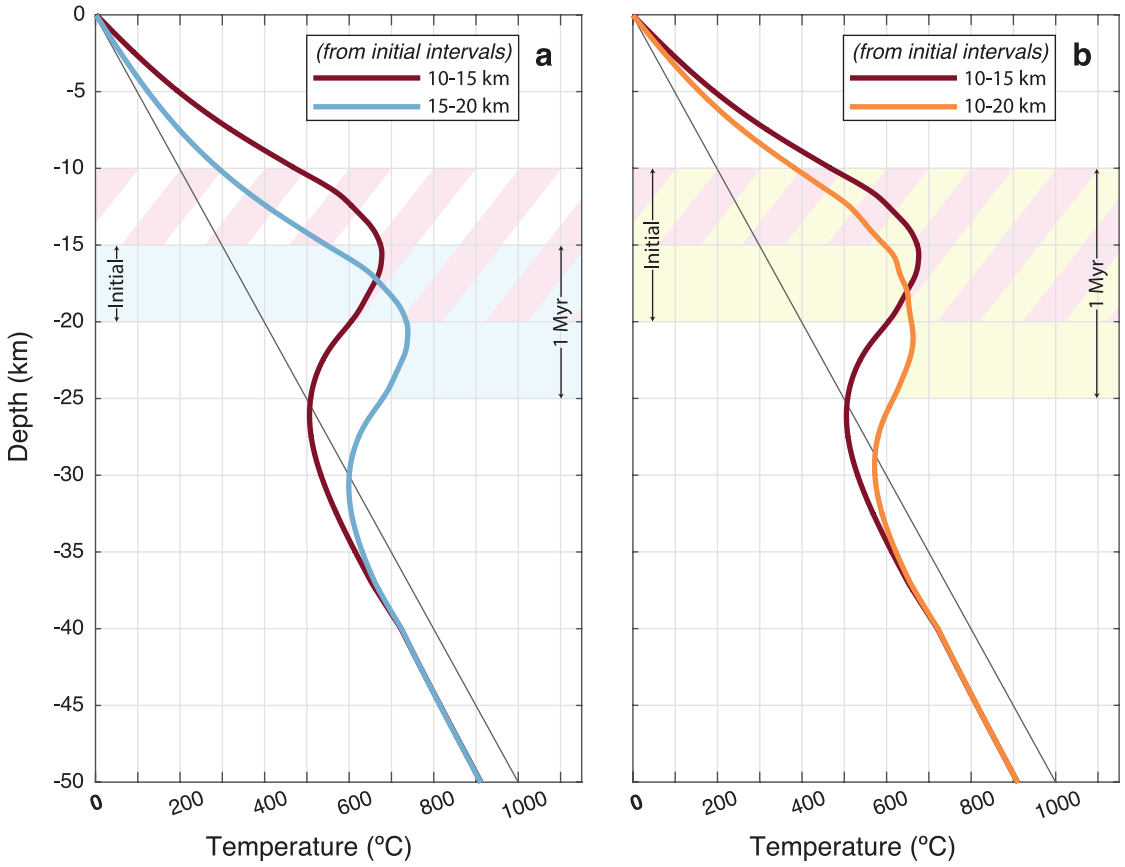

Figure A-6 Average thermal profile (maroon color) after 1 Myr of random-depth emplacement (50 m sill every 10 kyr; fluid-absent at 0.3 GPa, Figure 2-2b) for an initial depth range of 10-15 km. Pink hatched region denotes the initial and final depth range in this case. This thermal profile is compared to those for two other initial depth ranges: (a) 15-20 km (blue), where light blue shaded region highlights the initial and final (after 1 Myr) depth ranges. These two initial depth ranges, which span 5 km, result in basalt to granitoid ratios of 1:1 after 1 Myr. (b) 10-20 km (orange), where yellow shaded region highlights the initial and final (after 1 Myr) depth ranges. The final basalt to granitoid ratio is 1:2 when the initial depth range spans 10 km.

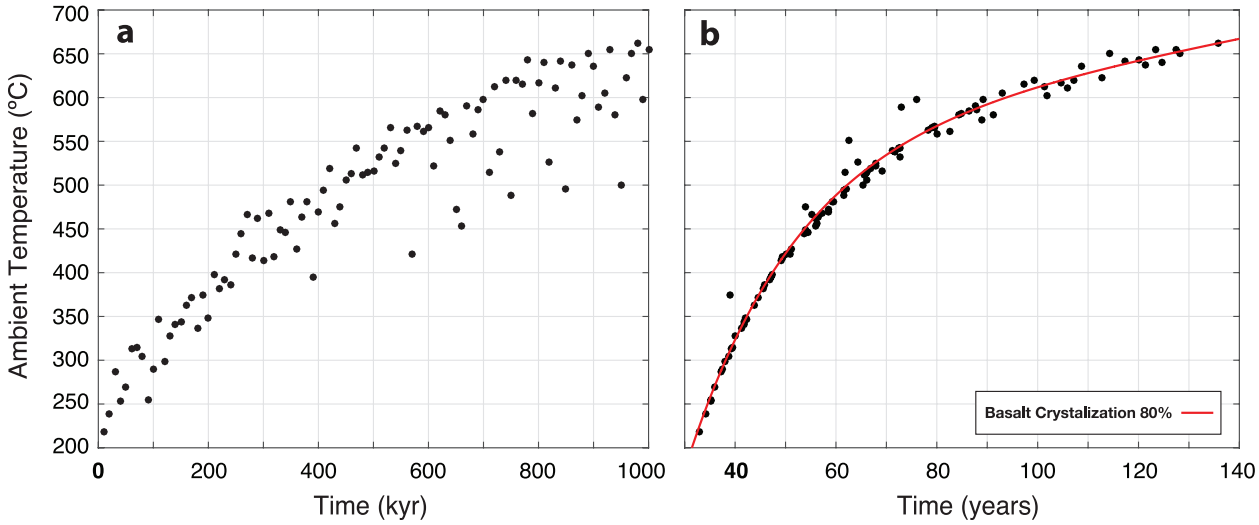

Figure A-7 (a) Plot of the ambient temperature of the crust immediately prior to emplacement of a new sill as a function of time during random sill emplacement (rate of 50 m sill every 10 kyrs; initial depth interval is 10-15 km). (b) Plot of ambient temperature of the crust immediately prior to emplacement of a new sill as a function of the time it takes a new basaltic sill to crystallize 80%. The simulation depicted used a finite fluid-present F-T relationship at 0.5 GPa (Figure 2-1c).

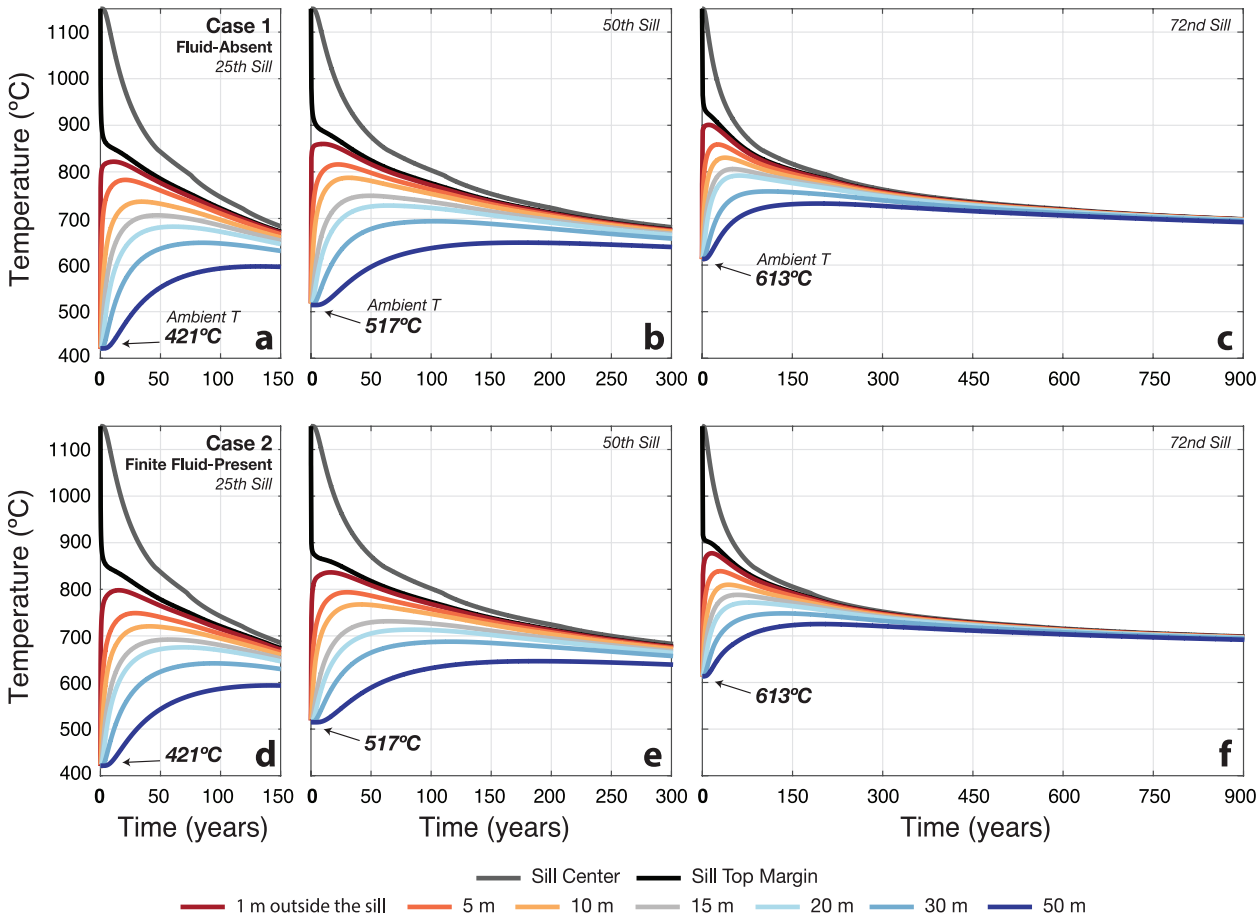

Figure A-8. Temperature vs. time immediately after sill emplacement at the basaltic sill center (gray line), basaltic sill top margin (black line), and depths 1, 5, 10, 15, 20, 30, and 50 m above the basaltic sill margin (colored lines same as in Figure 6). In all cases shown, random emplacement of 50-m thick sill every 10 kyr into an intial depth range of 10-15 km. (a) the 25th sill, (b) the 50th sill, and the (c) the 72nd sill; all for fluid-absent F-T curves at 0.3 GPa (Figure 2-1b). (d-f) same as (a-c), except all for finite fluid-present F-T curves at 0.3 GPa (Figure 2-1c). Bolded temperature with arrow is the ambient temperature of the crust immediately prior to sill emplacement.

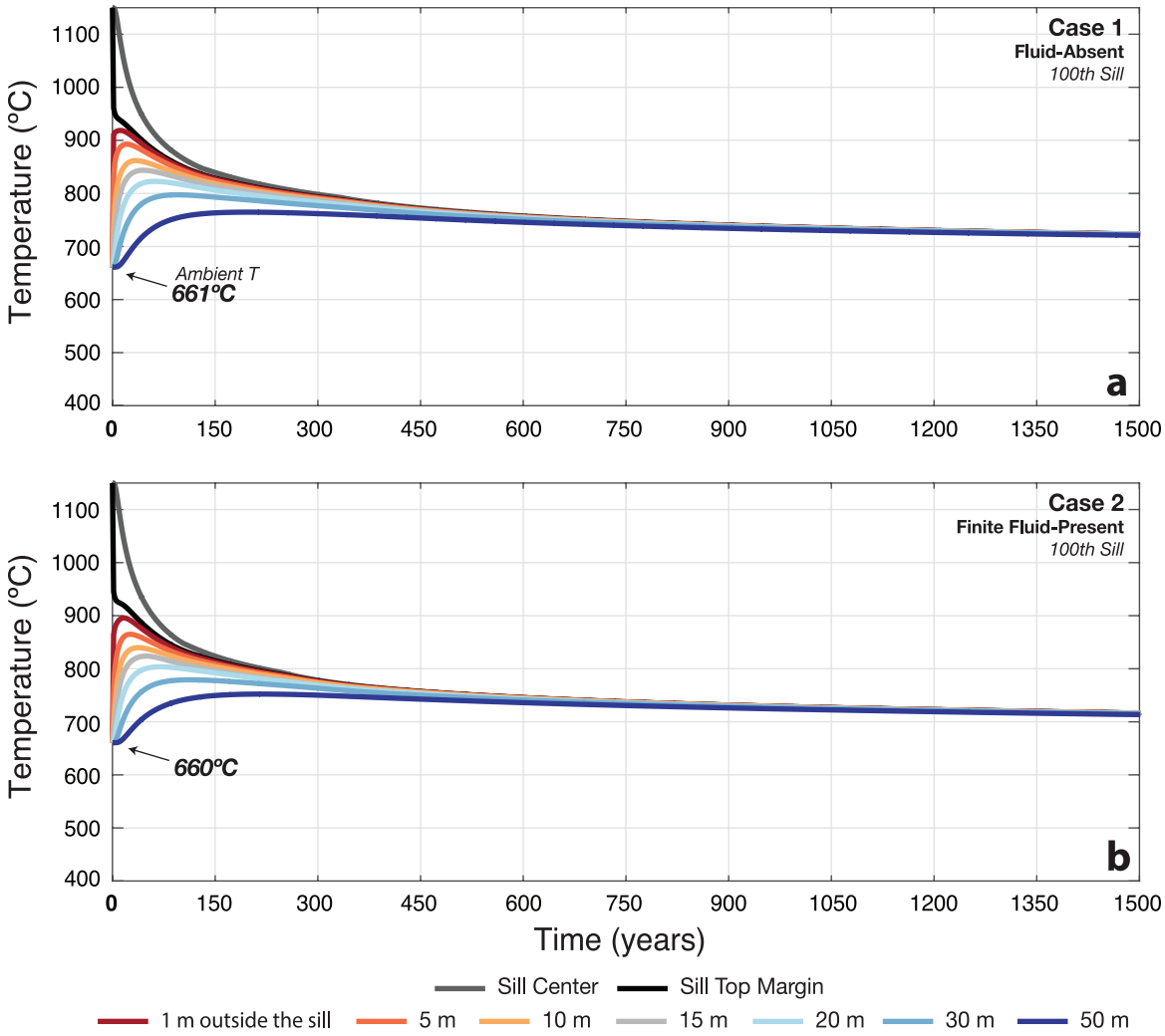

Figure A-9. (a) Same as Figure S8, but for the 100th sill; fluid-absent F-T curve at 0.3 GPa (Figure 2-1b). (b) same as (a), but for the 100th sill; finite fluid-present F-T curve at 0.3 GPa (Figure 1c). Bolded temperature with arrow is the ambient temperature of the crust immediately prior to sill emplacement.

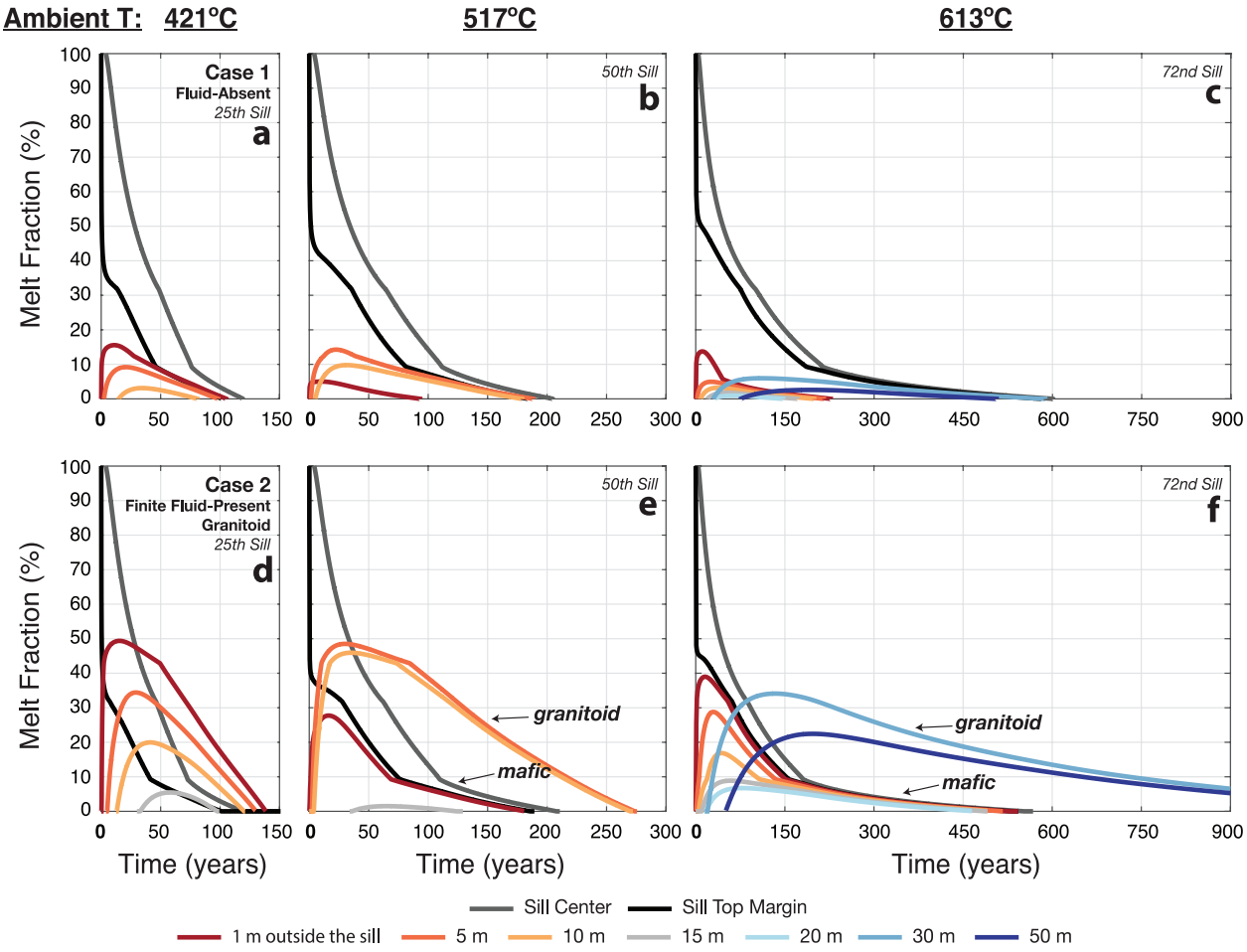

Figure A-10. Same as Figure A-8, but melt fraction instead of temperature is shown versus time immediately after sill emplacement. All symbols, colored lines the same as in Figure A-8. Arrows point to the different lithology (granitoid vs. mafic sill) of the wall rock (see Figure 2-6 in main paper).

Ambient T: **661°C (a) / 660°C (b)**

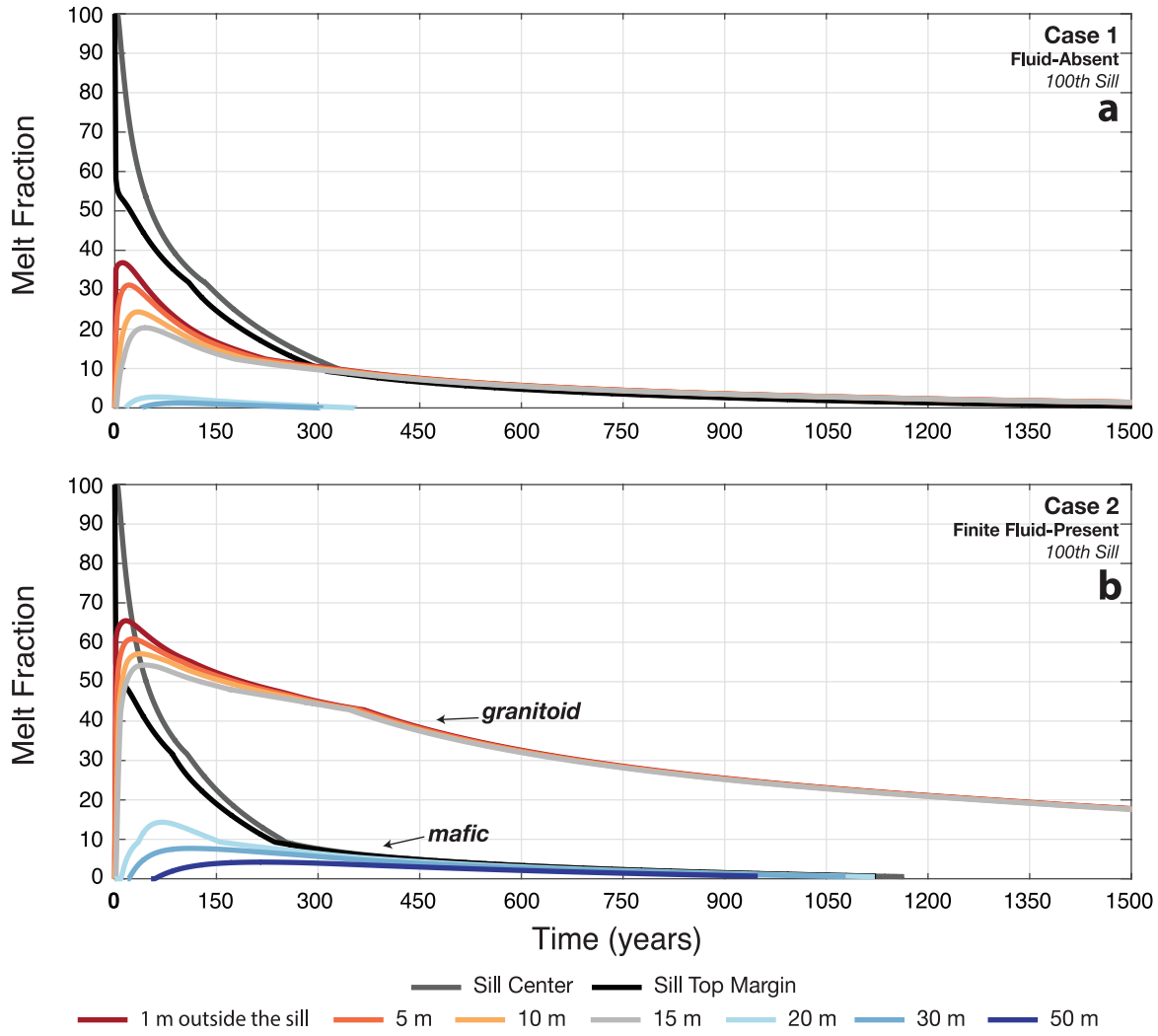

Figure A-11. Same as Figure A-9, but melt fraction instead of temperature is shown versus time immediately after sill emplacement. All symbols, colored lines the same as in Figure A-9. Arrows point to the different lithology (granitoid vs. mafic sill) of the wall rock (see Figure 2-6 in main paper).

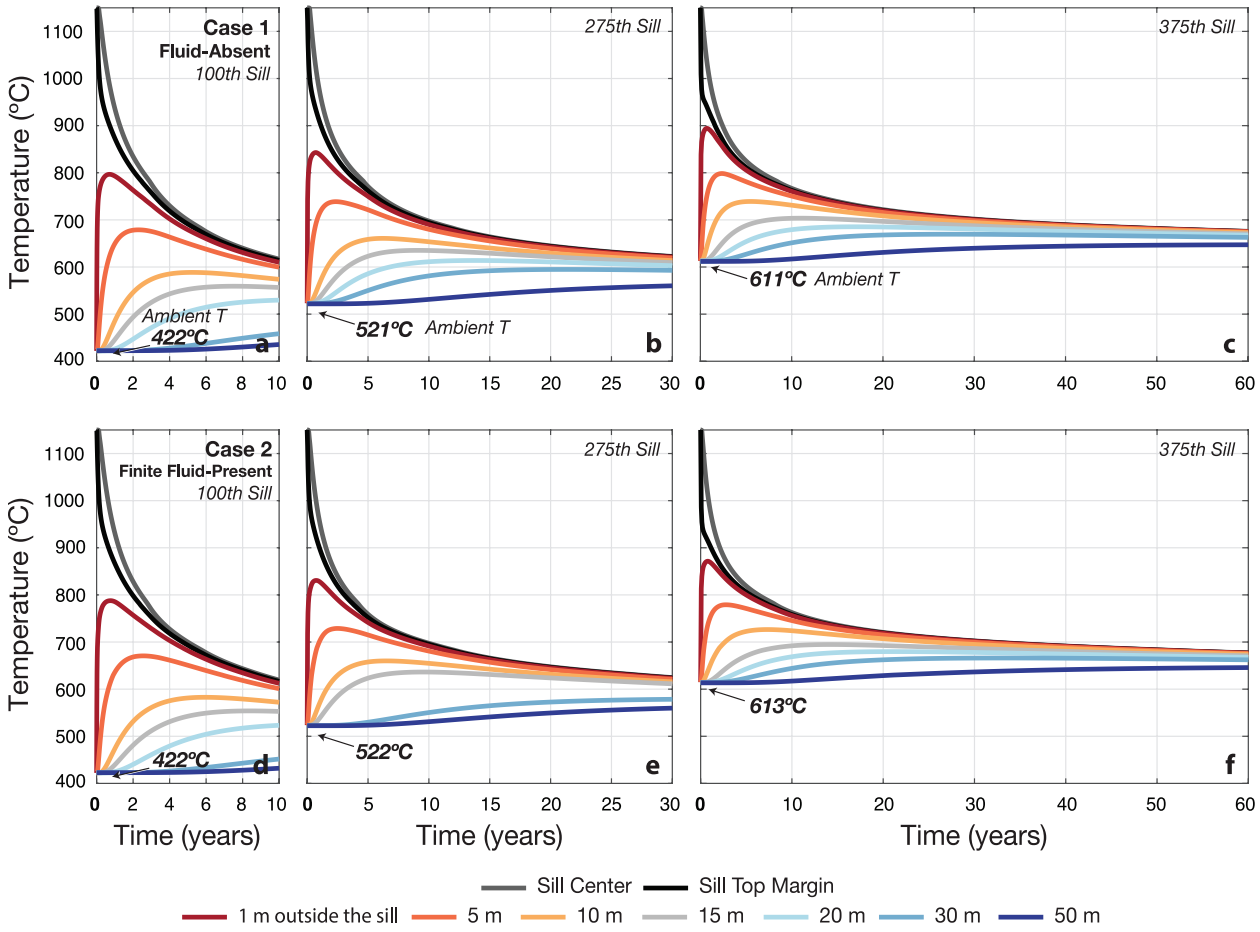

Figure A-12. Temperature vs. time immediately after sill emplacement at the basaltic sill center (gray line), basaltic sill top margin (black line), and depths 1, 5, 10, 15, 20, 30, and 50 m above the basaltic sill margin (colored lines same as in Figure 2-11). In all cases shown, random emplacement of 10-m thick sill every 2 kyr into an initial depth range of 10-15 km. (a) the 100th sill, (b) the 275th sill, and the (c) the 375th sill; all for fluid-absent F-T curves at 0.5 GPa (Figure 2-1b). (d-f) same as (a-c), except all for finite fluid-present F-T curves at 0.5 GPa (Figure 2-1c). Bolded temperature with arrow is the ambient temperature of the crust immediately prior to sill emplacement.

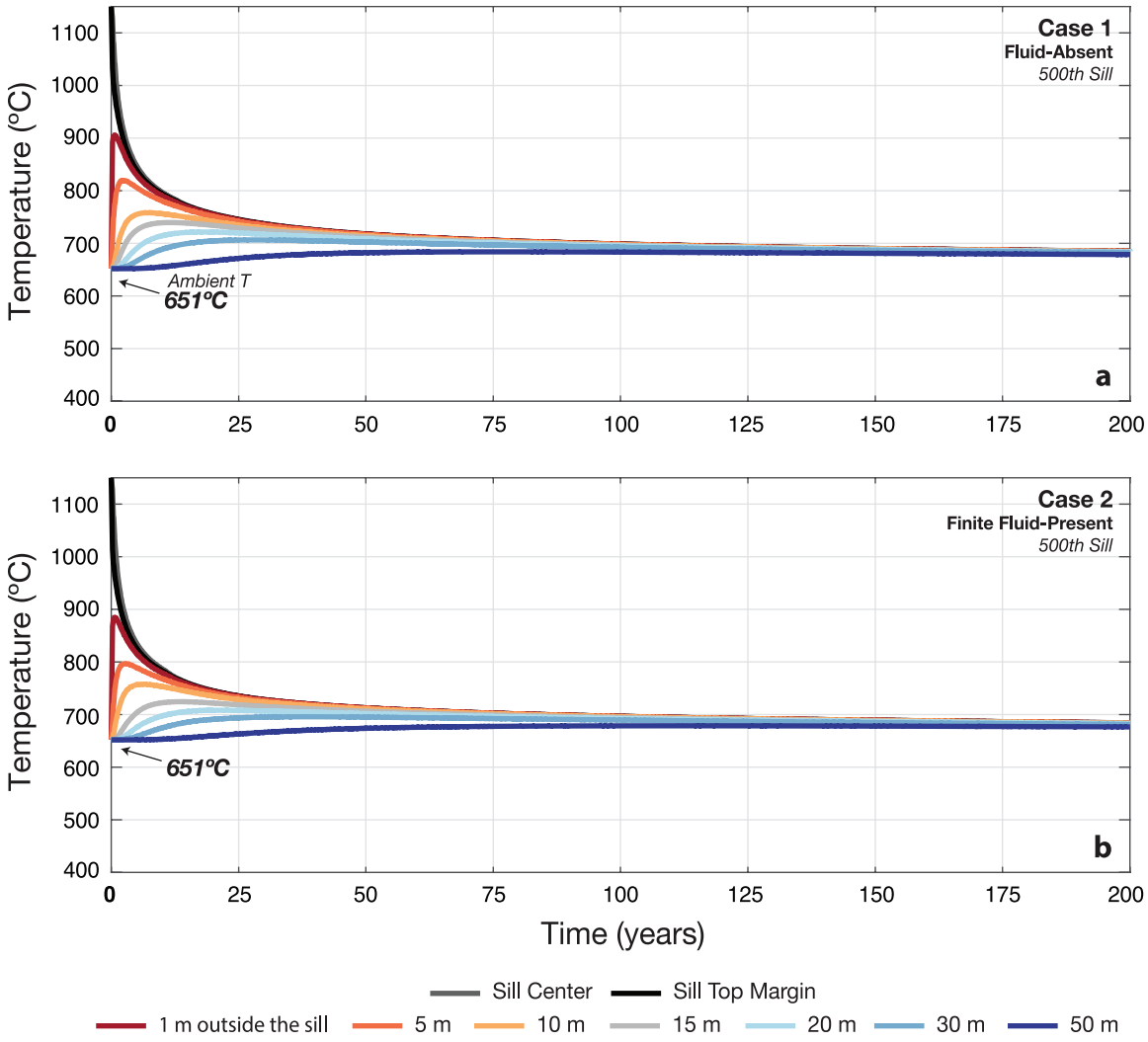

Figure A-13. (a) Same as Figure S12, but for the 100th sill; fluid-absent F-T curve at 0.5 GPa (Figure 2-1b). (b) same as (a), but for the 100th sill; finite fluid-present F-T curve at 0.5 GPa (Figure 2-1c). Bolded temperature with arrow is the ambient temperature of the crust immediately prior to sill emplacement.

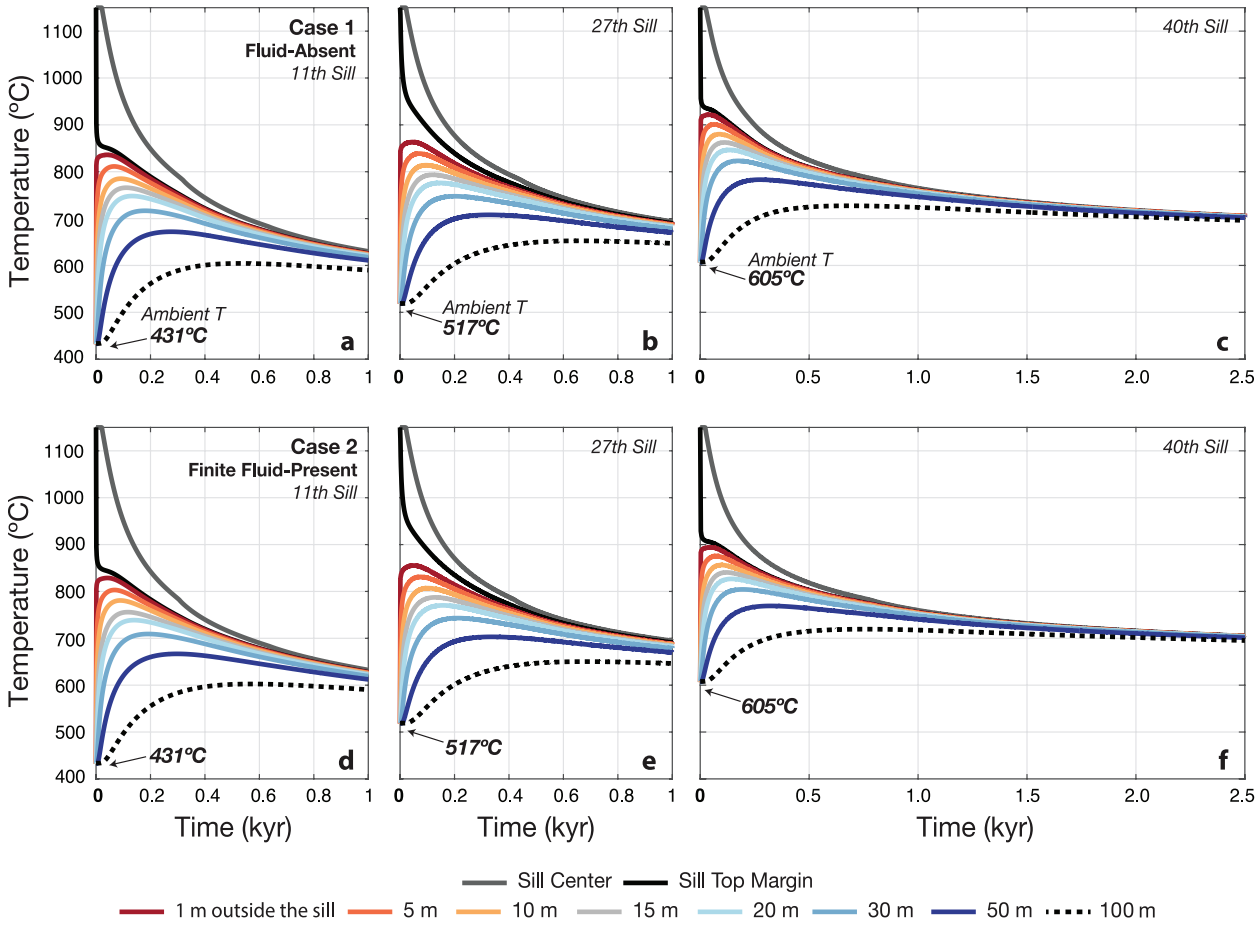

Figure A-14. Temperature vs. time immediately after sill emplacement at the basaltic sill center (gray line), basaltic sill top margin (black line), and depths 1, 5, 10, 15, 20, 30, 50, and 100 m above the basaltic sill margin (colored lines same as in Figure 2-11). In all cases shown, random emplacement of 100-m thick sill every 20 kyr into an initial depth range of 10-15 km. (a) the 11th sill, (b) the 27th sill, and the (c) the 40th sill; all for fluid-absent F-T curves at 0.5 GPa (Figure 2-1b). (d-f) same as (a-c), except all for finite fluid-present F-T curves at 0.5 GPa (Figure 2-1c). Bolded temperature with arrow is the ambient temperature of the crust immediately prior to sill emplacement.

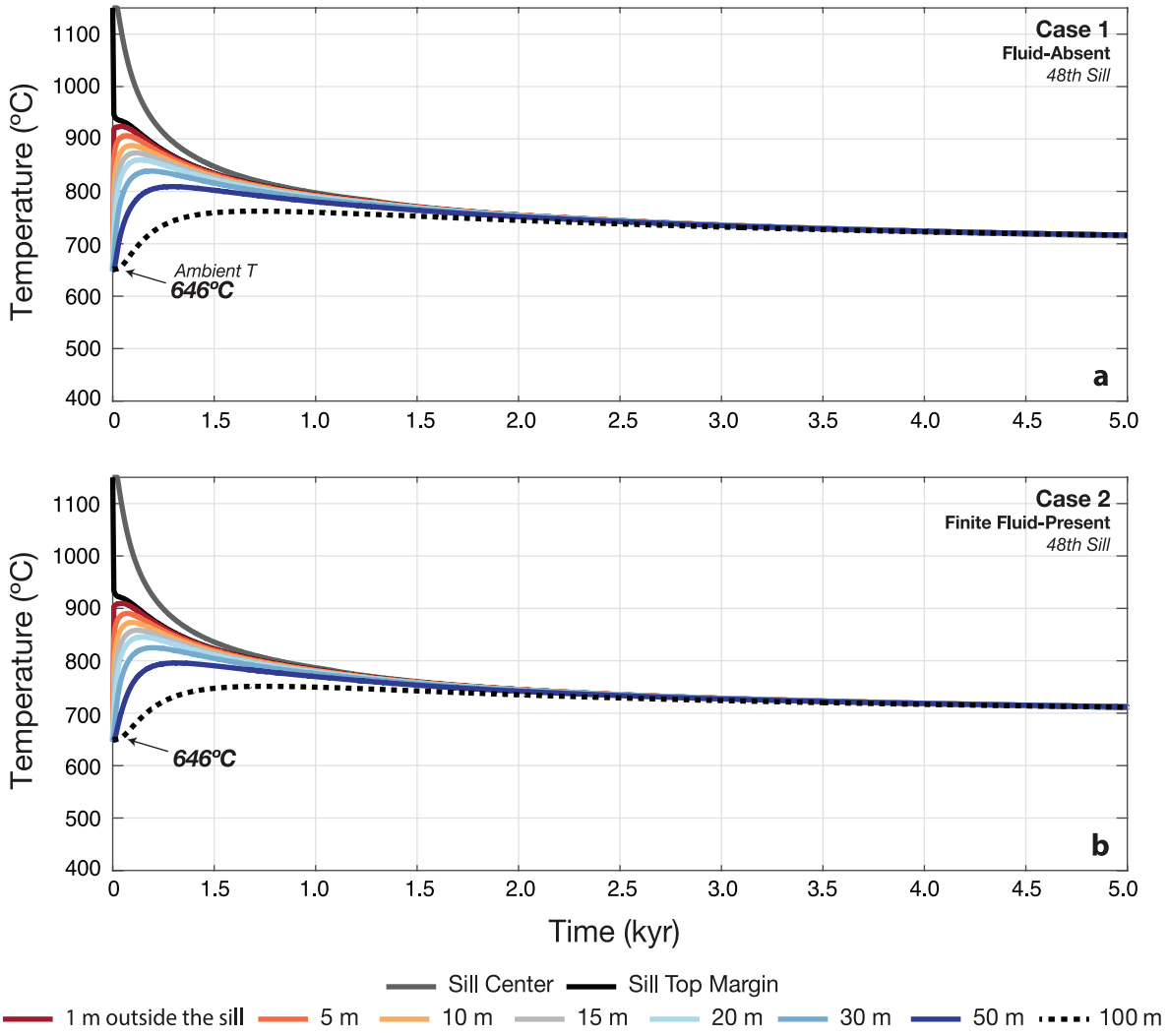

Figure A-15. (a) Same as Figure A-8, but for the 100th sill; fluid-absent F-T curve at 0.5 GPa (Figure 2-1b). (b) same as (a), but for the 100th sill; finite fluid-present F-T curve at 0.5 GPa (Figure 2-1c). Bolded temperature with arrow is the ambient temperature of the crust immediately prior to sill emplacement.

Ambient T: **651°C**

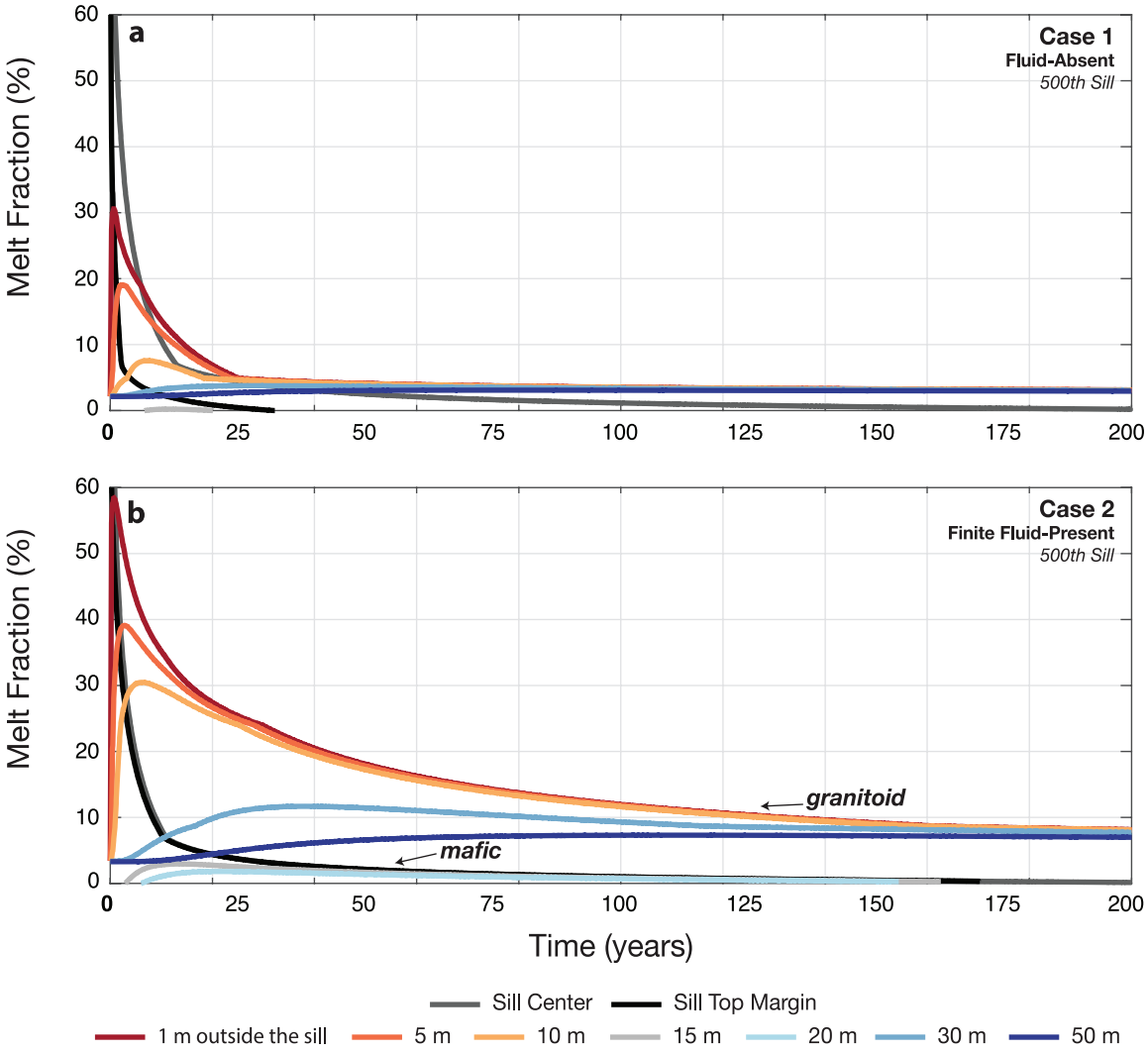

Figure A-16. Same as Figure A-13, but melt fraction instead of temperature is shown versus time immediately after sill emplacement. All symbols, colored lines the same as in Figure A-12. Arrows point to the different lithology (granitoid vs. mafic sill) of the wall rock (see Figure 2-11 in main paper).

Ambient T: **646°C**

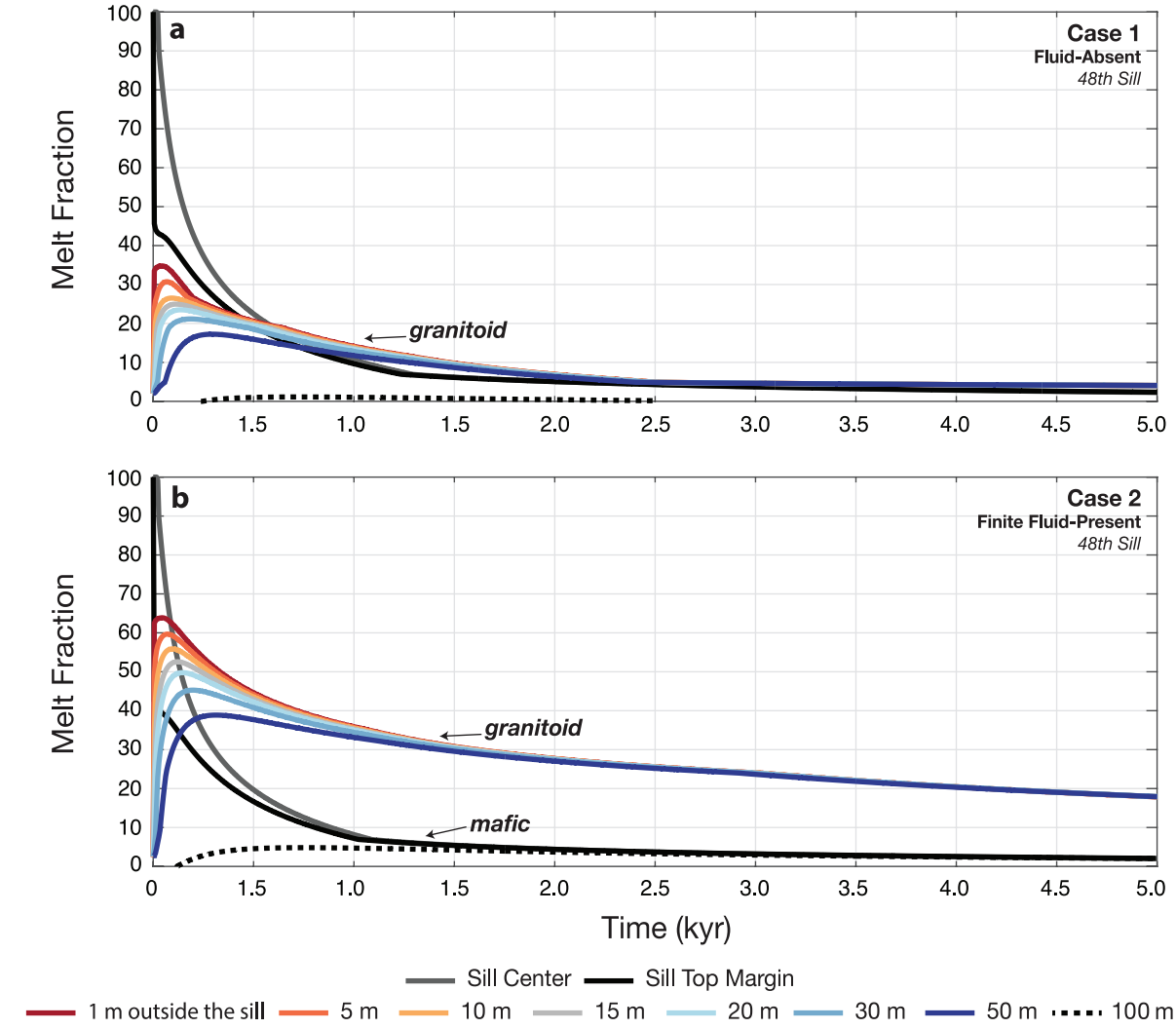

Figure A-17. Same as Figure A-15, but melt fraction instead of temperature is shown versus time immediately after sill emplacement. All symbols, colored lines the same as in Figure A-14. Arrows point to the different lithology (granitoid vs. mafic sill) of the wall rock (see Figure 2-11 in main paper)

Appendix B

Supplemental Material for Chapter 3

Supplement B-1 Figure benchmarking TIRAMISU: Transient hIgh-Resolution pArtial MeltIng Simulation of the crUst

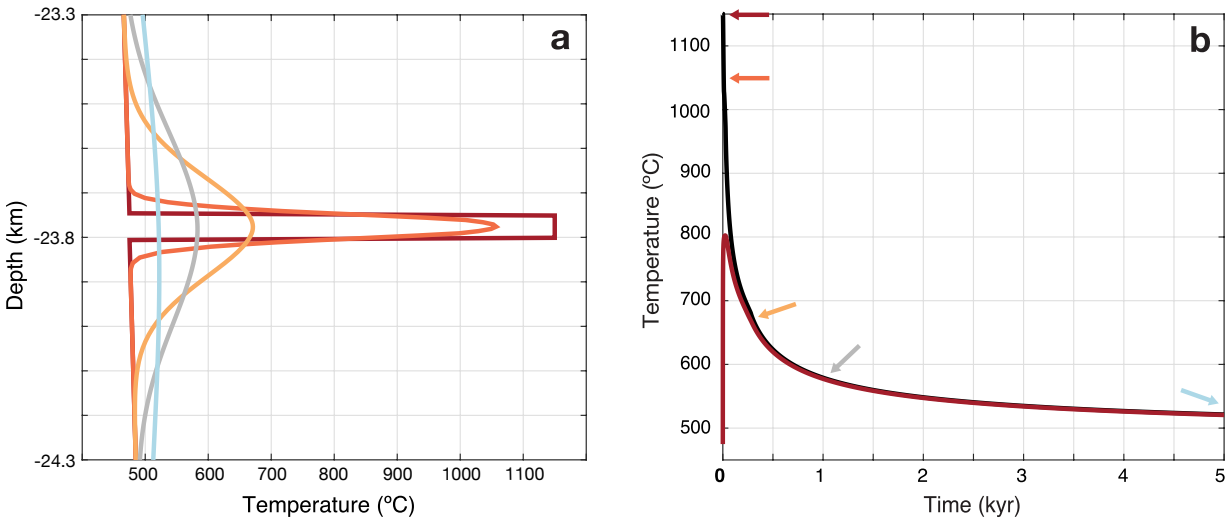

Figure B-18 A simulation was run with a 50–m thick basaltic sill emplaced into granitoid with its center at -23.775 kilometers depth, using the 0.5 GPa F-T curve from Figure 2-1a. The crust's initial temperature was a 20ºC per kilometer geothermal gradient. The sill was allowed to cool over 5 kyr. (a) A thermal profile of the cooling of the sill and the subsequent heating and cooling of the nearby crust above and below the sill. The curves are color coded for time stamps, pointed out from (b). (b) Shows the thermal evolution for the center of the sill (black) and 1 m outside of the sill (maroon).